Magnetic Biosensing System

A DISSERTATION
SUBMITTED TO THE FACULTY OF THE GRADUATE SCHOOL
OF THE UNIVERSITY OF MINNESOTA
BY

Yuanpeng Li

IN PARTIAL FULFILLMENT OF THE REQUIREMENTS
FOR THE DEGREE OF
DOCTOR OF PHILOSOPHY

Advisor: Jian-Ping Wang

April, 2015

Acknowledgements

First of all, I would like to sincerely express my greatest gratitude to my advisor, Prof. Jian-Ping Wang, for his inspiration, guidance and support throughout my PhD research. I greatly appreciate him for providing this opportunity to work on such an exciting field. Every time when I faced challenges he not only encouraged me but also provided great ideas and suggestions which lead to every breakthrough of my projects. His patience and understanding through all the time are vital for me. Without all these, this thesis would not be possible. His knowledge, enthusiasms and dedications to research and education have influenced me deeply.

I also would like to express my great gratitude to many people who have helped me on my thesis research. I thank Prof. Randall Victora, Prof. Bathanie Stadler and Prof. Jack Judy from MINT center on teaching me about magnetics; Prof. Chengguo Xing and Dr. Balasubramanian Srinivasan for the helpful discussions and collaborations on bioassay; Prof. Sang-Hyun Oh and Dr. Hyungsoon Im for the discussions and collaborations on DNA detection and microfluidic channel integration. I would like to thank all the staff members in UMN Nano Fabrication Center for giving me lots of help and suggestions during device fabrication. I appreciate to help from Prof. Bethanie Stadler, Prof. Anand Gopinath and Prof. Xiaojia Wang for serving as my defense committee.

I thank all of my colleagues in Wang's group for the helpful, inspiring discussions, sharing their research experiences, and all the assistance on my experiments, Dr. Meng Hao, Dr. Xiaofeng Yao and Dr. Yisong Zhang on device fabrications and characterizations; Dr. Wei Zhang, Dr. Liang Tu, Todd Klien, Yi Wang and Yinglong Feng on biosensing system integration; Dr. Yunhao Xu and Dr. Ying Jing for preparing high moment FeCo magnetic nanoparticles; Dr. Haibao Zhao, Dr. Xiaoqi Liu, Dr. Nian Ji, Dr. Hao Wang, Dr. Hui Zhao, Dr. Shihai He, and all the former and present group members for their help and support.

Last but not the least, my sincere thanks go to my parents, Yunlin Li and Shunhui Lin, for their support and trust through all these years. I thank my wife, Mingjing Ha for being

there all the time for me. I also want to dedicate this thesis to my newborn daughter Grace. Every single achievement in my life belongs to them too.

To my mother, father, wife and daughter.

Abstract

Biosensing systems that detect and quantify biomolecules at ultra-low concentration, with point of care settings, are of great need in many fields, including diagnostics, disease control, general health monitoring and fundamental research. Over the past decade, detection of biomolecule using magnetic biosensing system, which combines giant magnetoresistive (GMR) sensors and magnetic particles, has been attracting a lot of attention in biosensing area, due to the potential advantages on portability, low cost and rapid detection. This dissertation presents a novel magnetic biosensing system, consisting of highly sensitive GMR sensor and high-moment FeCo magnetic nanoparticle. Based on competition-based detection scheme, this system successfully demonstrates the quantification of ultralow concentration of biomarkers under a small magnetic field in real human serum/urine samples, and differentiates the patients with different grades of cancers.

One of the key factors to achieve detection of biomarkers in ultralow concentration is the sensitivity of the GMR biosensor. We designed and fabricated a GMR sensor with a near 0-degree ground state for the magnetization directions between pinned layer and free layer. This configuration enables three times greater sensitivity than any reported traditional GMR biosensor design, and requires much smaller polarization working field (10 Oe) which is more suitable for lab-on-chip and portable diagnostics.

Another key factor to increase the system sensitivity is to enhance the magnetic signal of magnetic label. High-magnetic-moment FeCo nanoparticles with great homogeneity, is

proposed and synthesized for biomedical application. The net magnetic moment of a FeCo nanoparticle is seven times higher than that of a commercial available Fe_3O_4 nanoparticle with an applied field of 10 Oe, assuming the same particle size. Moreover, the high homogeneity of FeCo nanoparticle enables the accurate quantification of low-abundance biomarkers.

Combining the novel GMR biosensor and high-moment FeCo magnetic nanoparticle, the accurate quantification of various biomarkers in real human serum/urine sample is demonstrated. To assist the high sensitivity quantification, two-layer/three-layer based competition detection schemes are developed. The low concentration interleukin-6 in unprocessed human sera, down to 200 copies, has been detected in only 5 minutes processing time. Based on the results, normal individuals and lung cancer patients were nicely identified. Moreover, the detection of as few as 1000 copies of endoglin is demonstrated in human urine samples. Based on the endoglin concentrations, the patients with different grades of prostate cancer are successfully differentiated.

Table of Contents

List of Tables

List of Figures

Chapter 1 Introduction

1.1 Introduction

Ultra-low concentration detection of biomolecules, such as proteins and DNAs, is highly desired for early detection of cancer and chronic diseases[1-7] when the biomarkers are only present in very low level. On the other hand, longitudinally monitoring[8-14] the changes of protein biomarkers is expected to help design medical treatment for specific individuals, which requires low-cost and easy-to-use medical devices[15-18]. Traditionally, fluorescence-based biosensors, such as enzyme-linked immunosorbent assays (ELISAs[19-21]), have been widely used in biomedical research and clinic for biosensing, although are only able to detect abundant of proteins. The main problems associated with fluorescence-based biosensors include lack of quantitative analysis, long processing time, expensive equipment and low signal-to-noise ratio due to the large optical background which limits the sensitivity[22]. Over the past ten years, magnetoresistive biosensors incorporated with magnetic labels (microbeads or nanoparticles) have become a promising candidate for biosensing due to the advantages of high sensitivity and low-cost. since such a system has the unique merits, including portability[23-25], low cost[26], rapid detection[27], ease for integration into lab-on-chip systems[28], and lack of magnetic background in biological samples. In this chapter, various biosensing techniques will be reviewed and discussed.

1.2 Optical biosensing

Optical biosensor has been widely employed, and is still one of dominant biosensors in various applications, such as clinical study[29], environmental monitoring[30], drug delivery[31] and warfare[32]. These applications are enabled by its advantages of insusceptible to electromagnetic field, low cost, easy for multiplexing and real time detection. On the other hand, optical biosensor also suffers in various aspects, for example, strong interference with light which leads to low signal to noise ratio and complicated/expensive setup to achieve high sensitivity. Although light is measured as output transduced signal for optical biosensor, based on detection principle, optical biosensor can be classified into two major categories: labeled and label-free detection. In labeled optical biosensing system, analyte of interest is typically bond to a light signal source directly or indirectly, such as fluorescence or phosphorescence, where the emission or absorbance of light with certain wavelength is monitored. Alternatively in label-free optical biosensor, the sensing signal is generated from the change of reflection/interference/evanescent field resulted from bioreaction. Ellipsometry, interferometry, surface plasmon resonance and optical waveguide, are most commonly used techniques in label free optical detection. In the following sections, various optical biosensing techniques are reviewed and discussed.

1.2.1 Fluorescent detection

Fluorescence, also called fluorophores or fluors, is by far the most often used optical method for biosensing. A typical fluorescent detection involves three stages: 1) absorbance; 2) excitation and 3) emission. Jablonski described the process using a diagram in 1993, later being called Jablonski diagram[33]. As shown in Figure 1.1, when a photon from excitation source is absorbed by fluorophore, an electron of fluorophore will be excited from ground state to excited state. There is a finite lifetime for the excited state, typically several nanoseconds, during which the excited electron consumed its partial energy due to the interaction with the molecular environment. In the last stage, the electron returns back to ground energy state and at the same time emits a photon. Due to the energy consumption in the second stage, the emitted photon has less energy than the injected one, thereby longer wavelength. As a result, the excitation light can be distinguished from the emitted florescent light.

The wavelength difference between excitation and emission is called stokes shift, which is a unique characteristic of each fluorescence. Preferably, a good fluorescent candidate should have large enough stoke shift, so that the wavelengths of excitation and emission light don't overlap with each other. The stoke shift characteristic is the key in multiplexing application, where multiple emission lights are excited and differentiated.

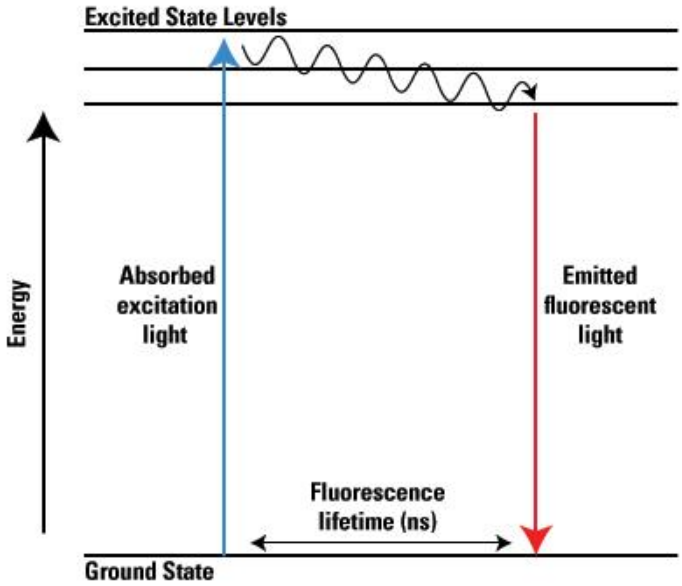

Figure 1.1 Jablonski energy diagram of fluorescence.

DNA microarray is one of the most important applications for fluorescent detection[34-37]. In the past decade, the development of DNA microarray has been motivated by many areas, such as gene expression profiling and comparative genomic hybridization. One of the most common DNA microarrays is to employ fluorescent labeled complimentary DNA (cDNA) for the detection. Figure 1.2 illustrates an example of using cDNA to investigate gene expression from yeast cell[38]. To start with, messenger RNAs (mRNAs), which are generated from the segmental copy of active gene, from both vegetative and sporulating yeast cells are collected. The mRNA produced by the yeast cells is complementary to certain original portion of the DNA strand. Next, by using reverse transcription, the complementary DNA to each mRNA is generated, during which the

florescent labels are attached to cDNA. In this case, vegetative yeast is labeled with green florescence, while sporulating yeast is labeled with red florescence. The florescent labeled cDNAs then are transferred and hybridized with DNA microarray, which containing the synthetic complimentary DNAs. Once the hybridization finishes, one can measure florescent light intensity from DNA microarray scan. The results reflect ratio of mRNAs from both sporulating yeast and vegetative yeast.

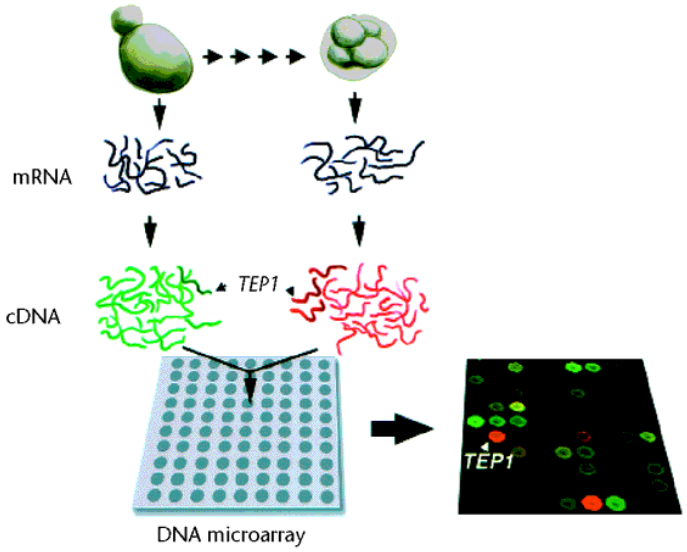

Figure 1.2 DNA microarray for yeast cell gene expression analysis.

An DNA microarray could hold up to thousands of spots with size of tens to hundreds of micrometers[39]. The array production can be either achieved by an auto spotting robots or photolithographic process. Affymetrix developed a process using photolithography and solid-phase DNA synthesis to construct DNA probe array, with a density as high as

approximately 300,000 polydeoxynucleotides on a 1.28 cm x 1.28 cm array[40]. With such high density and throughput, DNA microarray provides a powerful and efficient tool for genetic and cellular analysis.

Despite all the promising aspects discussed above, fluorescent detection has its own limitations, such as photobleaching. Being excited under high intensity light source or exposed to multiple detections, the fluorescent effect may be destructed irreversibly, which is called photobleaching. The root cause for photobleaching can be quite complex involving several different mechanisms[41]. Usually the hypothesis of multiple photochemical reaction pathways is referred to the main reason. Meanwhile, to achieve high detection sensitivity, fluorescent detection typically requires expensive and stationary laser system, as well as scanner. Therefore, other biosensing technologies, such as surface plasma resonance from same optical area and magnetic biosensing, are also being explored.

1.2.2 Surface plasma resonance

Surface plasma resonance (SPR) is a process, where the photons of incident polarized light couple with the free electrons (surface plasmons) at the interface between materials with negative and positive permittivity. This phenomenon was first observed by Wood[42] (initially named Wood's anomaly) in 1902, when he discovered the anomalous change of diffraction energy from metallic gratings. The process creates an electromagnetic field,

while at total excitation it generates a strong evanescent field which propagates along the interface. Since the evanescent field is very sensitive to the dielectric properties of the interface, surface plasma resonance has been widely used in microscopy[43,44], plasmonics[45-47], as well as biomedical applications[48-50].

To generate SPR, most of the current commercial SPR systems, such as Biacore, Spreeta and Optrel, employ prim coupling configuration proposed and developed by Otto[51] and Kretschmann[52]. Prism coupling based SPR sensor typically consists of an optical medium (such as prism), and a thin metal layer (such as gold), as shown in Figure 1.3 (a)[49]. A charge density oscillation could be generated at the interface, due to the opposite signs of dielectric constants of the prism and gold thin film. With the incident light, the charge density oscillation will couple with the plasma oscillation of the electrons in the metal, generating an evanescent field. In this configuration, when reaching the attenuated total reflection (ATR), the evanescent field generated by the incident light has the strongest intensity, while the reflectance shows a dip in the reflected light spectrum (Figure 1.3 (b)). With the binding of biomolecules, such as surface receptors or analyte, the evanescent field will strongly interact with the newly added bimolecular layers. Therefore, the dielectric property of the interface will be changed, so that the dip of reflectance will be shifted, or the reflected intensity will be changed. Such shift or intensity change, can be then measured by an external detector at the same time, which is the identifier of the bio-binding process. Although offering great sensitivity,

prism coupling configuration has challenge in device miniaturization and integration, due to the relatively large size of optical medium and detection system.

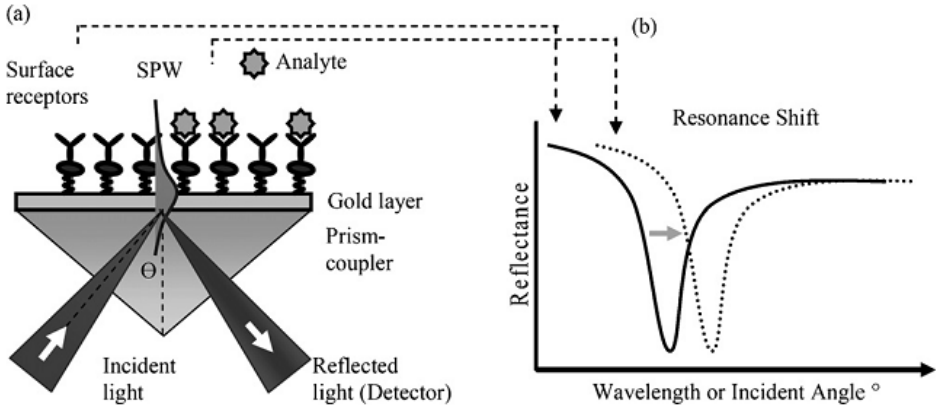

Figure 1.3 (a) Prism coupling SRP configuration; (b) resonance swift in the reflected light spectrum

Besides the prism coupling, some other SPR configurations are also studied. The main principle of other SPR configurations is similar to that of prism coupled SPR, except replacing prism with other optical medium, which would couple the incident light with the surface plasmons at interface. Jorgenson *et al.*[53] proposed optical fiber coupled SPR sensing in 1993. In this SPR configuration (Figure 1.4), an optical fiber, which can be single-mode[54] or multimode[55], is used to guide the incident light through the fiber by total internal reflection. The detection could happen at the fiber tips where the reflected light or diffracted light is measured, which is similar to the prism coupled method. At the fiber tips, evanescent field is also excited by the interaction between incident light and

the surface plasmons, which would be used for the detection of bio-bonding process. The advantage of waveguide coupled SPR over prism coupled SPR is unlike the bulky setup with prism coupled SPR, the feasibility for device miniaturization.

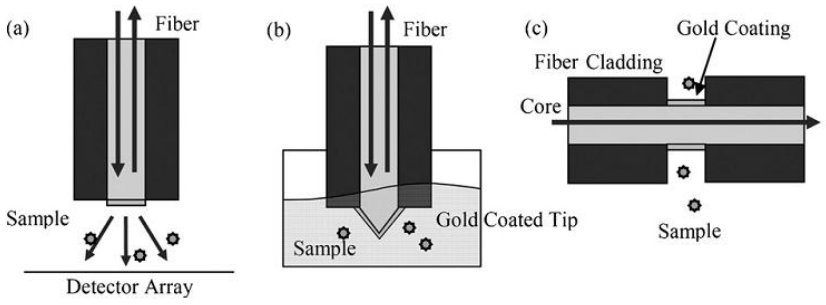

Figure 1.4 Schematic showing of three fiber-optic sensor configurations: a) polished end; 2) micro-prism end; 3) cladding-removed

1.3 Magnetic biosensing

The discovery of giant magnetoresistive (GMR) effect by Fert[56] and Grunberg[57], who was rewarded by Noble Prize in physics 2007, boosts the development of magnetic storage industry, as well as creating a new emerging area of spintronics. Recently, GMR or magnetic tunneling junction (MTJ) based biosensors have attracted increasing interest in the world. This technique uses GMR/MTJ sensors to detect the stray magnetic fields associated with the magnetic labels bonded with the biomolecules. In this section, magnetoresistive based biosensor will be reviewed and discussed.

1.3.1 GMR effect

GMR effect is a phenomenon that the resistance of the device changes under the application of magnetic field. Typically, the term of magnetoresistance (MR) is used to characterize the amount of the resistance change with the magnetic field. MR can be expressed by:

$$MR=\frac{R(\boldsymbol{H})-R_0}{R_0}$$

where $R(\boldsymbol{H})$ is the resistance of the device with magnetic field $\boldsymbol{H}$, and R_0 is the resistance without magnetic field. Magnetoresistance may originate from different mechanisms other than GMR, such as colossal magnetoresistance (CMR), anisotropic magnetoresistance (AMR) or tunneling magnetoresistance (TMR).

GMR was first reported experimentally by Fert[56] and Grunbery[57] independently in 1988. As shown in Figure 1.5, Fert *et al*. demonstrated nearly 50% of MR change using the (001)Fe/(001)Cr supperlattice structure prepared by molecular beam epitaxy, under 2T magnetic field and a low temperature of 4.2K. On the other hand, Grunbery also reported 10% of MR change from Fe-Cr-Fe layers with antiferromagnetic interlayer exchange, under around 0.35T and 5K temperature. Historically, before the discovery of GMR, the observed highest MR change was from AMR effect, which is around a few percentages. Therefore, the word "giant" was used by Fert to distinguish the large MR change comparing to AMR effect.

In theory, GMR effect can be explained by Mott's two current model[58], which was published in 1936 to qualitatively understand the sudden change of resistivity in ferromagnetic metals around Curie temperature. In his model, Mott proposed that, 1) the electron transport exists for both up-spin and down-spin independently in ferromagnetic material, and 2) electron scattering in ferromagnetic layer is strongly spin dependent. One assumption is that the mean free path of the electron is much longer than the thickness of the layers. Therefore, in a ferromagnetic/non-magnetic/ferromagnetic (FM/NM/FM) structure as shown in Figure 1.6 (a), one can assume the electron scattering is weak for up-spin with magnetization direction, while is strong in the case of down-spin. When the magnetizations of two ferromagnetic layers are parallel, up-spin encounters less electron scattering in both ferromagnetic layers, which results in smaller resistivity in both layers. On the other hand, down-spin, due to the spin dependent scattering, experiences more electron scattering on both layers, which leads to higher resistivity in both layers. Hence, the equivalent resistance circuit is shown in the bottom of Figure 1.6 (a), and the resistance is

$$R_P = \frac{R_\uparrow R_\downarrow}{R_\uparrow + R_\downarrow}$$

where $R_\uparrow$ is the device resistance of up-spin electrons, and $R_\downarrow$ is the device resistance of down-spin electrons. For the antiparallel case, as shown in Figure 1.6 (b), both up-spin

and down-spin experience strong scattering in one of the ferromagnetic layers, where the resistance is

$$R_P = \frac{R_\uparrow + R_\downarrow}{2}$$

therefore, the equivalent resistance in antiparallel configuration is higher than that of parallel configuration. In addition, the MR can then be expressed by:

$$MR = \frac{R_{AP} - R_P}{R_P} = \frac{(R_\downarrow - R_\uparrow)^2}{4R_\uparrow R_\downarrow}$$

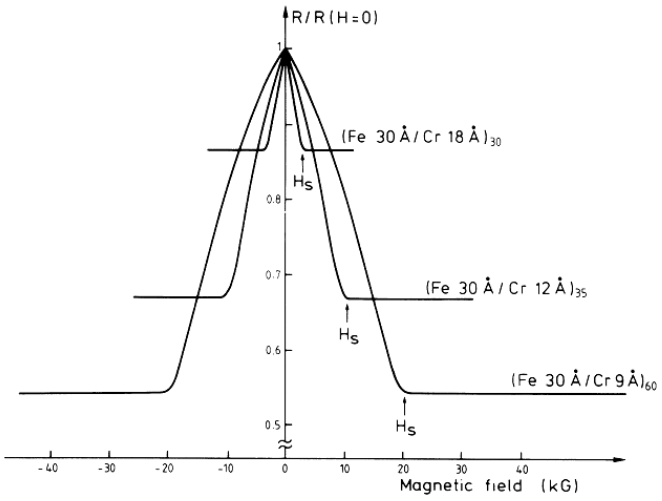

Figure 1.5 Magnetoresistance of three Fe/Cr superlattices at 4.2K
The current and the applied field are long the same [110] axis in the plane of the layers

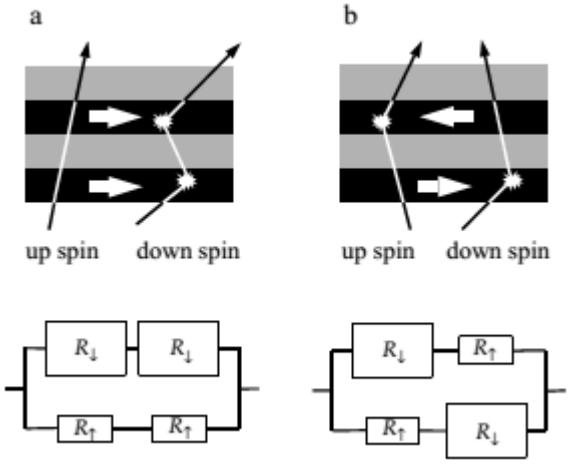

Figure 1.6 Schematic illustration of electron transport in a multilayer for parallel (a) and antiparallel (b) magnetizations of the successive ferromagnetic layers
The solid lines are individual electron trajectories

1.3.2 Spin valve structure

The GMR device is quite complex and functional only under large applied field and low temperature, due to the antiferromagnetic coupling between the multilayers. Such restrictions prevent the wide application of GMR device where small magnetic field and nominal/high temperature are needed. In 1991, spin valve structure[60] was proposed by Dieny *et al*. In the spin valve structure (Figure 1.7), a non-magnetic metal layer (also called spacer) is sandwiched between two ferromagnetic layers. The magnetization of one of the ferromagnetic layer is pinned by an antiferromagnetic (AFM) layer (such as IrMn, FeMn), which is also called fixed layer or pinned layer. Since it is pinned, the magnetization of fixed layer is not sensitive to the applied magnetic field, while the other

ferromagnetic layer is free to rotate with the application of external magnetic field. The resistance of the spin valve GMR sensor is high when the magnetizations of fixed and free layers are antiparallel and low when they are parallel. Therefore, the dynamic range of the spin valve GMR sensor typically depends on the anisotropy of the free layers. Figure 1.8 shows the around 4% MR response within +/- 50 Oe reported by Dieny *et al*.

Since then, spin valve GMR sensor has been studied and researched intensively. One important application for spin valve GMR sensor is magnetic recording. Spin valve GMR sensor was used as read sensor in hard drive industry[61,62], which increases areal density by three orders of magnitude (from ~0.1 to ~100 Gbit/in^2) between 1991 and 2003, till the invention of TMR sensor. Other applications include magnetic field sensing, magnetic random access momery (MRAM), as well as magnetic biosensing, which will be discussed in later sections.

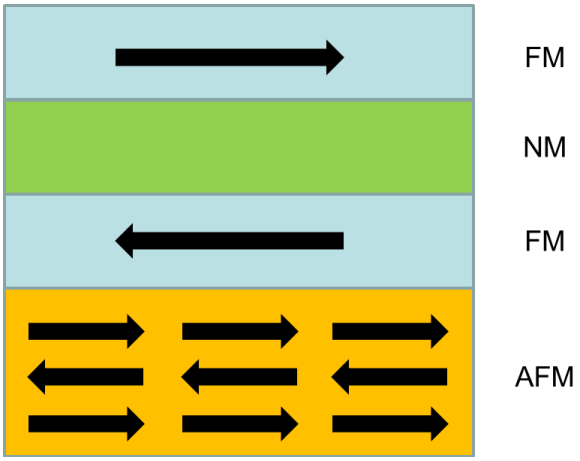

Figure 1.7 The schematic drawing of spin valve structure

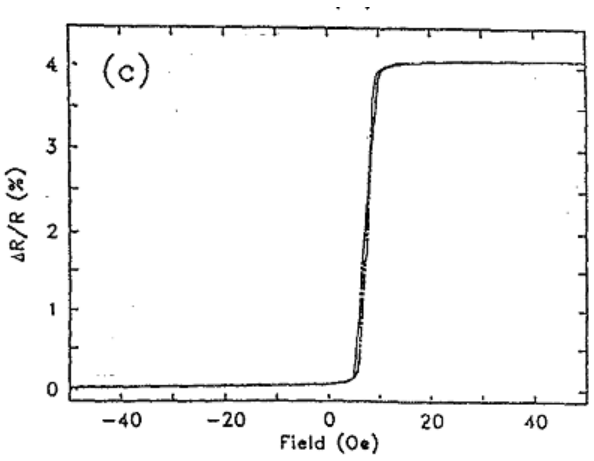

Figure 1.8 MR response of spin valve GMR sensor between +/- 50 Oe

1.3.3 GMR biosensing

In recent years, GMR or MTJ based biosensors are intensively studied. The first demonstration of magnetic biosensing system was done by Baselt *et al*. from Naval research lab[63]. As shown in Figure 1.9, this unit, which is called Bead ARray Counter (BARC), detects microsized magnetic beads immobilized on the GMR sensor surface. Bruckl *et al*. employed a spiral-shaped GMR biosensor and concluded that the GMR biosensor has higher sensitivity than fluorescence-based biosensor[64]. Tondra *et al*. examined the theoretical signal to noise ratio of this type of assay and predicted the possibility of detection of magnetic nanoparticle labels[65]. Freitas *et al*. developed a prototype of hand-held microsystem based on fully integrated magnetic biosensors for the

first time[66]. Prins *et al.*[67] and Boeck *et al.*[68] first demonstrated the real-time on-chip detection and manipulation of microsized magnetic particle using microfabricated current wires. Wang *et al.* demonstrated a multiplex protein assay using 50 nm magnetic nanotag sensing[23]. Besides GMR biosensor, MTJ biosensor is another promising candidate due to its high MR ratio. Xiao *et al*. has shown the detection of DNA labeled magnetic nanoparticles using MgO based MTJ sensor[69]. Table 1-1 briefly summaries, up to date, different magnetic biosensing systems, from the aspects of sensor type/size, sensor working range, magnetic label/size and the application to biomarker detection.

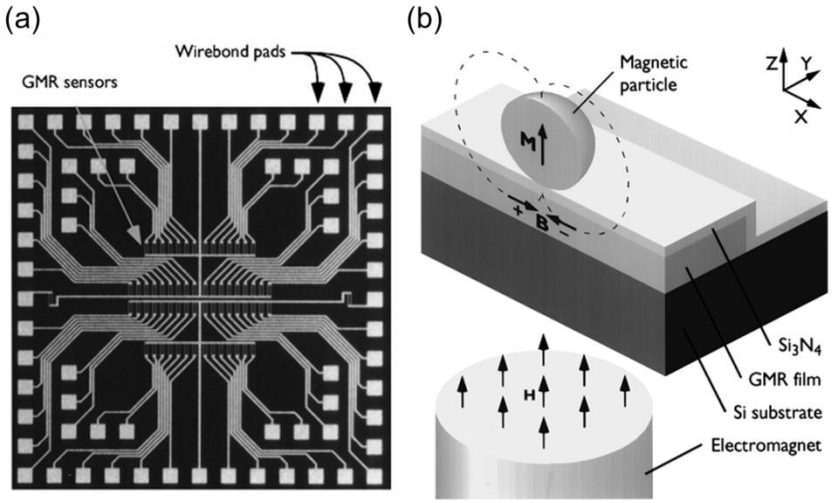

Figure 1.9 Prototype of BARC and detection principle
(a) Protograph of a prototype of 64 magnetoresistive sensors, which is composed of 80 × 20 μm GMR sensors

(b) Cross-section of a GMR sensor, illustrating the method used to detect superparamagnetic beads.

Group, location	Sensor type, size (μm*μm)	Sensor working range	Magnetic label, size	Biomolecule detection?	Biomarker detection?	Reference
Baselt et al., Naval research lab	GMR strip, 80*20	50 Oe	Dynal M280, 2.8um	Yes	No	[6]
Tondra et al., NVE	Wheatstone bridge GMR spin valve, 11*2	150 Oe	N/A	Yes	No	[16]
Freitas et al., Portugal	MTJ, 6*2	30 Oe DC + 13.5 Oe rms AC	Nanomag-D, 130nm	Yes	No	[9]
Wang et al., Stanford	GMR spin valve, 100*1.5	80 Oe rms AC + 50 Oe bias	MACS, 50nm	Yes	Yes	[10]
Prins et al., Netherlands	GMR, 100*3	20 Oe rms AC	Dynal Myone, 1um	Yes	Yes	[11] [17]
Boeck et al., Belgium	GMR spin valve, 10*1.4	N/A	Micromer-M, 2um	No	No	[12]
Bruck et al., Germany	GMR spiral-shaped, 1800*1	-500 Oe ~ 500 Oe	Bangs CM01N, 350nm	Yes	No	[7]
Xiao et al., Brown	MTJ, 18*6	-60 Oe ~ 60 Oe + 50 Oe DC bias	MACS, 50nm	Yes	No	[13]
Wang et al., U of Minnesota	GMR spin valve, 80*40	0 ~ 15 Oe	FeCo, 12.75nm	Yes	Yes	[15]

Table 1-1 Summary of magnetoresistive sensor and magnetic labels

Chapter 2 Magnetic Biosensing System Design

2.1 Introduction

There are typically three important components in a magnetic biosensing system: 1) magnetic biosensor; 2) magnetic label; 3) detection scheme. In this chapter, each essential component is discussed respectively. These results have been published as "Biomarkers identification and detection based on GMR sensor and sub 13 nm magnetic nanoparticles", Li, Y. *et al*. in Engineering in Medicine and Biology Society, 2009. EMBC 2009. Annual International Conference of the IEEE. 5432-5435.

2.2 Magnetic biosensor design

Sensor design is always the key factor in a sensing system. The sensitivity and the detection range of a sensing system exclusively depend on the design of sensor. Majority of magnetic biosensing systems utilizes the linear sensor following the magnetic recording industry, which is reviewed in this section. Meanwhile, another type of biosensor design, hysteresis sensor is proposed and demonstrated in this thesis. The different magnetic biosensor properties of these two types of sensor designs, such as sensitivity and detection range, are discussed in the following sections.

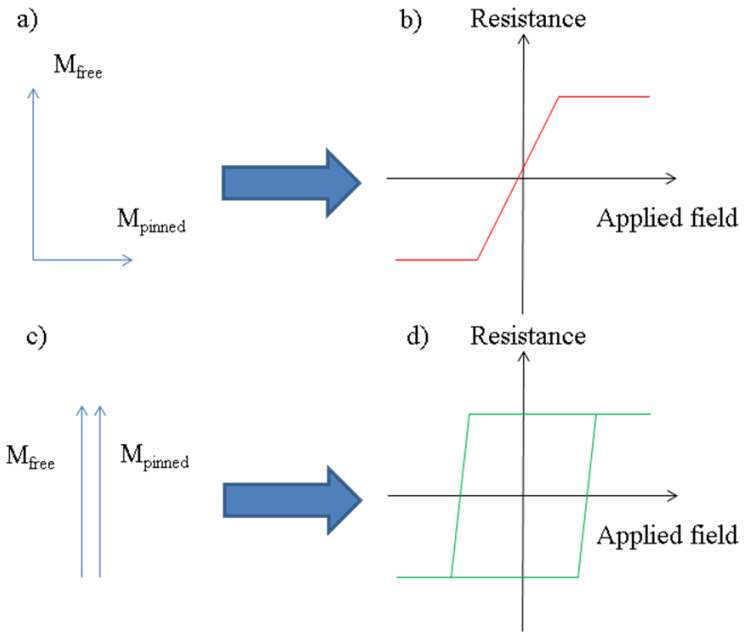

Figure 2.1 Magnetization configuration and transfer curve of linear and hysteresis GMR sensor
a) Traditional GMR configuration: 90 degree ground state for magnetization directions between free layer and pinned layer. b) Linear transfer curve for traditional GMR configuration. c) New GMR configuration: zero degree ground state. d) High sensitive transfer curve from zero degree ground state. (M_{free} and M_{pinned} represent the magnetization directions of free layer and pinned layer, respectively)

The sensitivity of the GMR biosensor is one of the key factors in the detection of low concentration biomarker. Currently, most of the GMR sensors reported have a 90 degree ground state for magnetization directions between free layer and pinned layer, as shown in Figure 2.1 (a). The transfer curve for this traditional configuration of the GMR sensor is shown in Figure 2.1 (b) as a red line. This orthogonal configuration originates from magnetic recording industry, where GMR sensor is used as a reader for sensing the

magnetic stray field from the spinning disk. While this design shows good linear signal output, the drawback is the requirement of large applied field (100 Oe or above) which limits its sensitivity and portability. To solve these problems, we proposed, designed and fabricated GMR sensor with zero degree ground state for magnetization direction between free layer and pinned layer shown in Figure 2.1 (c). Based on its transfer curve as shown in Figure 2.1 (d), hysteresis sensor design enables a higher sensitivity (dR/dH) and requires a much lower applied field compared to the traditional 90 degree configuration. Especially, the unique feature of low applied field makes this design more suitable for lab-on-chip and portable diagnostics. Figure 2.2 shows a fabricated GMR sensor with 3% MR and maximum sensitivity of 0.6 % MR per Oe near 10 Oe applied field. This sensitivity is three times higher than any traditional GMR sensor design that has been reported.

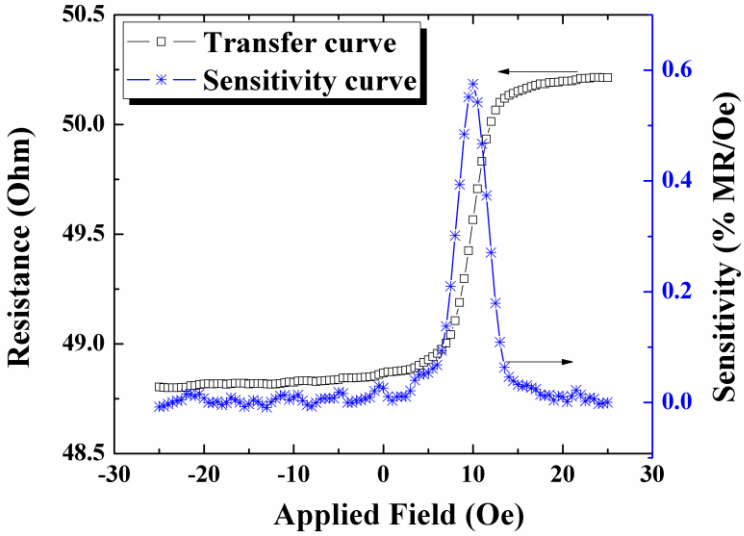

Figure 2.2 Transfer curve and sensitivity curve of GMR

2.3 Magnetic label

Magnetic biosensing is usually an indirect detection method since the biological sample (analyte) does not provide magnetic signal, except under very high magnetic field, such as nuclear magnetic resonance (NMR). Therefore, magnetic labels, like magnetic microbeads or nanoparticles, are needed to provide magnetic signal for sensor detection. Furthermore, there are several considerations for the design of magnetic label.

First of all, magnetic label is required to be superparamagnetic to avoid the particle aggregation during sample preparation. The magnetization of superparamagnetic particle can be described by the Langevin function as

$$\boldsymbol{M} = \boldsymbol{M}_s \times L(\frac{\boldsymbol{m}_0 \mu_0 \boldsymbol{H}}{k_B T})$$

where $\boldsymbol{M}_s$ is the saturation magnetization, $\boldsymbol{m}_0$ is the saturation magnetic moment of a single particle, μ_0 is the magnetic permeability of vacuum, $\boldsymbol{H}$ is the applied magnetic field, k_B is the Boltzmann constant, T is the absolute temperature, and L is the Langevin function. Therefore, without any applied magnetic field, the net magnetization of a superparamagnetic particle is zero at room temperature, which prevents the unnecessary magnetic interaction between particles.

Secondly, magnetic label with high magnetic moment under reasonable applied magnetic field is preferred. The way that magnetic label provides signal to magnetic biosensor is through magnetic dipole interaction. Therefore, higher magnetic moment, which is proportional to larger magnetic dipole field, would provide stronger magnetic signal to sensor.

Thirdly, the size and homogeneity of magnetic label is very critical. Up to date, most of the reported magnetic labels are commercially available, and vary in size from 50nm to 3μm. Due to the low diffusivity and poor binding selectivity, microsized magnetic labels are not favorable for biomolecule detection. On the other hand, nanosized magnetic labels, with similar size to biomarkers, are preferred in the application of magnetic biosensing. Figure 2.3 shows the summary of magnetic label size published in the past ten years. The arrow drawn for the guide of eye shows a clear trend indicating that

magnetic labels with smaller size become more preferred in the magnetic biosensing scheme. In recent few years (shown in the insert of Figure 2.3), sub 50nm magnetic labels have been integrated into the magnetic sensing system.

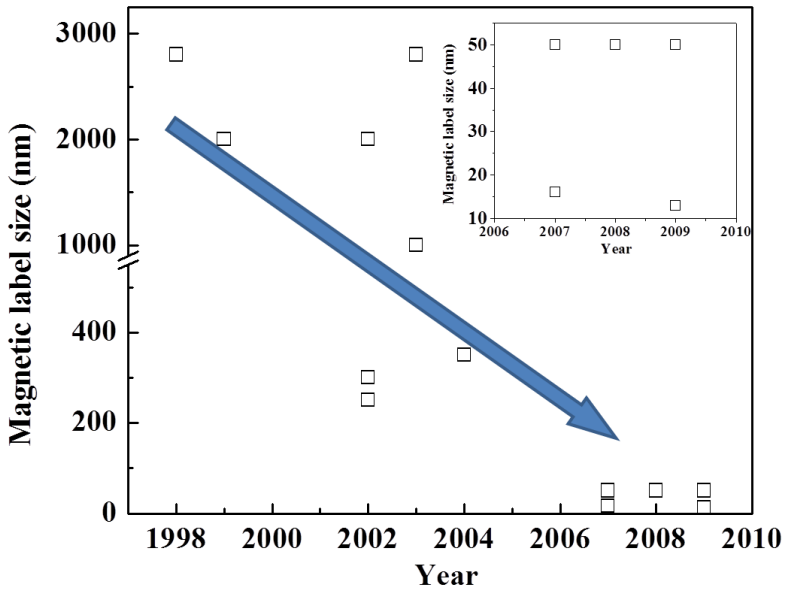

Figure 2.3 Summary of size of magnetic labels used in the past ten years

While most of research groups use commercial iron oxide nanoparticles with low magnetic moments, high moment FeCo magnetic nanoparticle is utilized for magnetic biosensing application in this dissertation,. The net magnetic moment of a 12.75 nm FeCo nanoparticle is 7 times higher than that of a commercially available γ-Fe_2O_3 nanoparticle at external field of 10 Oe, assuming the same nanoparticle size and 1.5 nm oxide shell for

FeCo nanoparticles. Figure 2.4 shows TEM image of 12.8 nm FeCo magnetic nanoparticles with a composition of 70:30 which were synthesized using a sputtering gas condensation technique[71]. The particle morphology and phase are precisely controlled by modifying the magnetic flux in the sputtering target. The prepared FeCo nanoparticles are dominantly cubic shaped. The nanoparticles are highly homogeneous as shown in Figure 2.5, which is crucial for accurate biomolecule quantification.

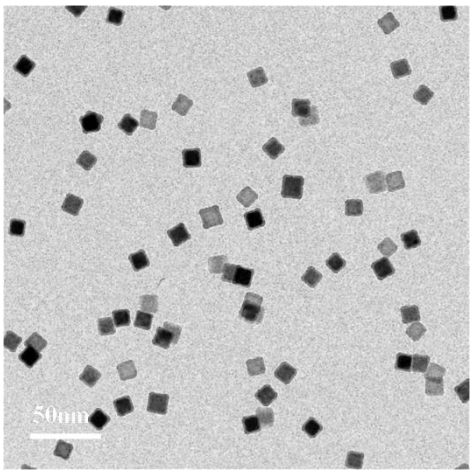

Figure 2.4 TEM image of cubic FeCo nanoparticles

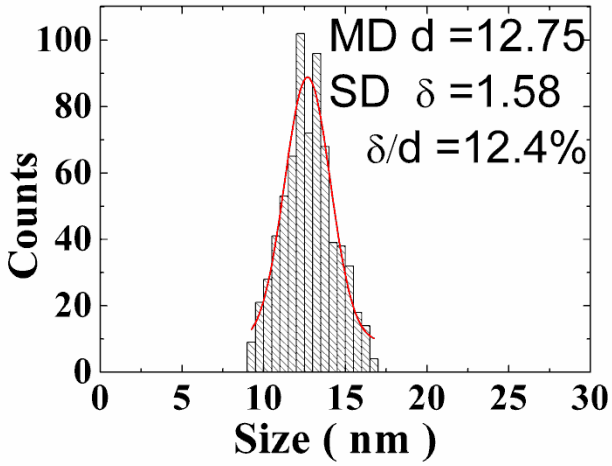

Figure 2.5 Size distribution of FeCo nanoparticles

2.4 Magnetic biosensing detection scheme

Since magnetic biosensing is an indirect detection method, the detection scheme, which connects magnetic label to magnetic biosensor, is vital to whole system. Traditionally, there are two detection schemes: three-layer and two-layer. Figure 2.6 (a) demonstrates a three-layer structure based biomarker detection scheme using GMR biosensor and high moment FeCo magnetic nanoparticles. The capture antibodies are first immobilized on the positive GMR sensor surface. Then the samples with biomarkers, such as IL-6, are applied on GMR sensor surface under the binding condition. Subsequently, the detection antibodies modified by high moment FeCo magnetic nanoparticles are applied on the sensor surface. After thorough rinsing, the modified detection antibodies bind to the capture antibody-modified positive GMR biosensor,

contributing to the sensing signal picked up by the GMR biosensor underneath. This structure is typically referred as sandwich or three-layer structure. As shown in Figure 2.6 (b), another detection scheme is to bypass the detection antibody, and directly bind the magnetic nanoparticle onto biomarker. This structure is referred as bilayer or two-layer structure. The advantage of this method is the magnetic signal would be higher since the magnetic nanoparticles are closer to magnetic biosensor. However, directly labeling biomarkers is not preferred, since it may contaminate the sample.

To solve this problem, in this thesis, a competition based two-layer detection scheme is proposed. As shown in Figure 2.7, two-layer competition detection scheme starts with unprocessed sample and standard reference sample. The standard reference sample consists of the same target analyte as unprocessed sample, but with magnetic nanoparticle labeled purposely first. While applying both samples on sensor surface with detection antibodies, analytes with and without magnetic label would compete the limited binding sites of detection antibodies. Eventually, an equilibrium state can be achieved, when the amounts of both labeled and unlabeled analytes, which binds to the detection antibodies, stay unchanged. Under this circumstance, the magnetic signal from labeled analyte reflects not only the amount of labeled analyte binding to detection antibodies, but also the amount of unlabeled analyte binding to detection antibodies. Usually a dose response curve is established first with difference amount of known analyte concentrations. Later, the concentration of unlabeled analyte can extracted from the does response curve, based

on the magnetic signal from competition based detection scheme. The experimental results are discussed in Chapter 4.

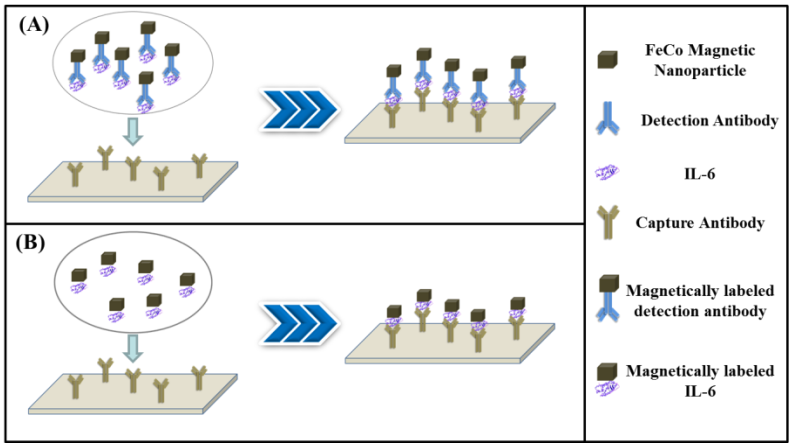

Figure 2.6 Two different GMR biosensor and magnetic nanoparticle-based biomolecule detection schemes.
(A) Three-layer approach: the GMR biosensors are first functionalized with capture antibodies. The analyte spotted onto the GMR biosensor surface binds to the capture antibody. Subsequently, detection antibodies labelled with magnetic nanoparticles are then applied and bind to the captured analyte. (B) Two-layer approach: after the functionalization with capture antibodies, the magnetic nanoparticle modified analyte are directly applied and captured on the GMR biosensors.

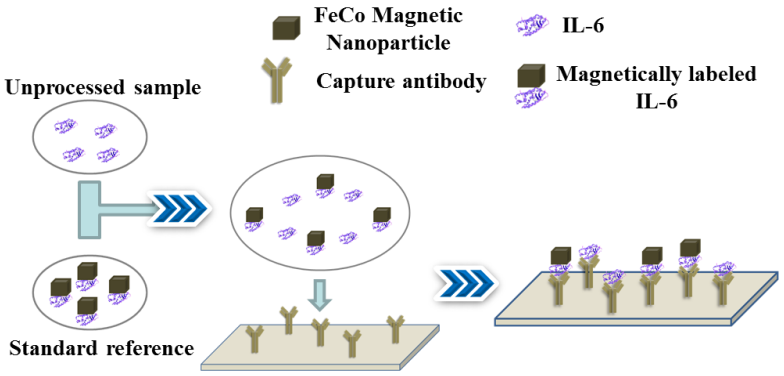

Figure 2.7 Two-layer based competition detection scheme.
The magnetic nanoparticle labeled analyte and unlabeled analyte are applied on the same capture antibody functionalized GMR biosensor and compete the binding sites.

Chapter 3 Sensor Fabrication and Measurement

3.1 Introduction

In this chapter, the fabrication process of GMR biosensor is introduced first. The process steps consist of certain semiconductor fabrication techniques, such as thin film deposition, photo-lithography and dry etching (ion milling). Each main step is discussed respectively in this chapter. Furthermore, the measurement scheme of the sensing system is discussed.

3.2 GMR thin film stack deposition

The GMR magnetic biosensor is made of multilayer thin film structure which is deposited in high vacuum condition. The multiplayer stack consists of both metallic (magnetic and non-magnetic) and insulating layers, with only nanometers thickness.

The GMR stack deposition starts from a silicon wafer, which has 100 nm pre-deposition thermal oxide by using thermco mini brute. As shown in Figure 3.1, a multilayer GMR structure of Ta (5nm) /$Ir_{0.8}Mn_{0.2}$ (10nm) /$Co_{0.9}Fe_{0.1}$ (2.5nm) /Cu (3.3nm) /$Co_{0.9}Fe_{0.1}$ (1nm) /$Ni_{0.82}Fe_{0.12}$ (2nm) /Ta (5nm) was deposited on thermal oxide silicon wafer using a six-target Shamrock sputtering system[72]. Shamrock sputtering system utilizes the magnetron sputtering technique, which is a widely used physical vapor deposition (PVD) method for thin film deposition. In magnetron sputtering, the sputtering

target is bombarded by energetic ions, in this case, Ar^+ ions, so that the sputtering material is ejected and deposited on the substrate. What makes the magnetron sputtering different from other general sputtering technique is that a magnetic field is used to constrain the secondary electron close to target, which increases the plasma density. During the film deposition, a magnetic field of around 50 Oe was applied to the main flat of the substrate wafer, in order to induce in-plane parallel easy axis.

The detailed sputtering conditions of each layer are listed below (Ar pressure, sputtering power, bias voltage, sputtering time):

Ta50: 50sccm Ar, 156W, 60V, 175sec

IrMn80: 50sccm Ar, 257W, 30V, 140sec

CoFe25: 25sccm Ar, 193W, 60V, 75sec

Cu33: 45sccm Ar, 176W, 60V, 17sec

CoFe10: 25sccm Ar, 193W, 60V, 30sec

NiFe20: 25sccm Ar, 283W, 60V, 33sec

Ta50: 50sccm Ar, 156W, 60V, 175sec

The film composition was confirmed by Auger electron spectroscopy (AES) thin film elemental depth profiling, as shown in Figure 3.2. In AES depth profiling, the concentration of each element in the GMR stack basically follows the stack deposition sequence. The Ta layer serves as a seed layer of the stack. An antiferromagnetic layer $Ir_{0.8}Mn_{0.2}$ layer is used to pin the pinned magnetic $Co_{0.9}Fe_{0.1}$ layer. The free layer consists

of $Co_{0.9}Fe_{0.1}$ and $Ni_{0.82}Fe_{0.12}$ bi-layers, which is very sensitive to the external magnetic field. During stack deposition, there is an external magnetic field applied along the main flat of the silicon substrate. Figure 3.3 shows the direction of the induced magnetic anisotropy, which defines the easy axis of free layer on wafer level.

After the deposition, the GMR wafer was post-annealed under 200 degree C for 30 minutes, where the easy axis of pinned layer is defined. Figure 3.4 shows the hysteresis loop of the wafer level GMR stack after annealing, which is measured along the hard axis direction. As shown in the figure, the wafer level GMR stack shows an easy axis loop of the hysteresis loop, with ~350 Oe exchange bias field of the pinned layer and ~15 Oe coecivity field of the free layer. Figure 3.4 demonstrates that, on wafer level, the GMR stack has around 2.42% magnetoresistive ratio (MR) on hard axis direction, and the sensor sensitivity is around 0.04622 ohm/Oe. On the other hand, Figure 3.5 shows the hysteresis loop and transfer curve of the wafer level GMR stack measured along the easy axis direction. Both hysteresis loop and transfer curve show a hard axis behavior. From the two set of hysteresis loops and transfer curves, it is suggested that the magnetization of free layer aligns with that of pinned layer after annealing, which is possibly due to orange peel coupling[73].

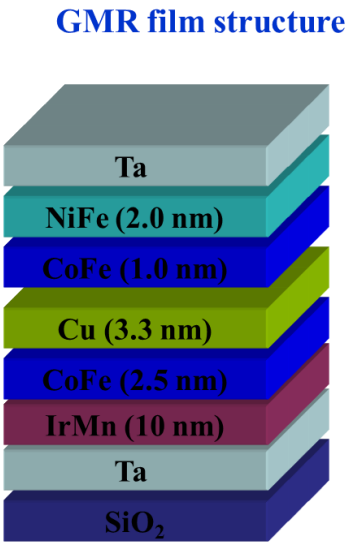

Figure 3.1 Schematic showing of GMR thin film stack

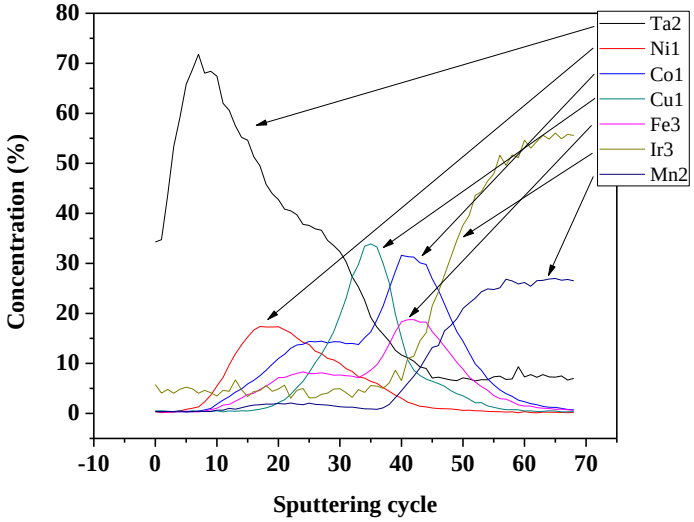

Figure 3.2 Auger electron spectroscopy thin film elemental depth profiling of GMR stack

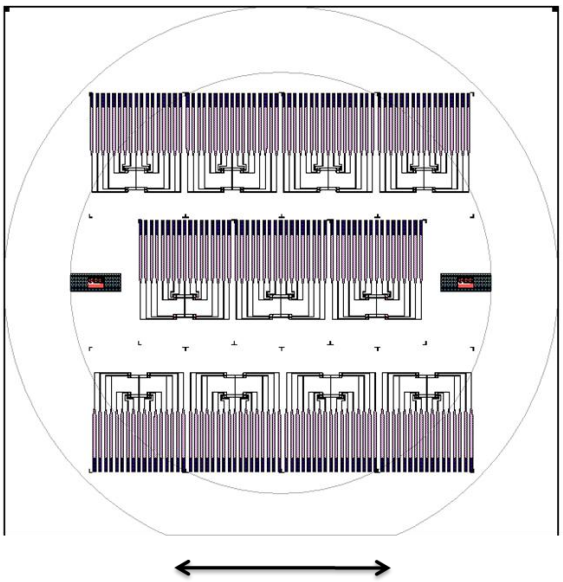

Figure 3.3 Induced magnetic anisotropy configuration on wafer during GMR stack deposition

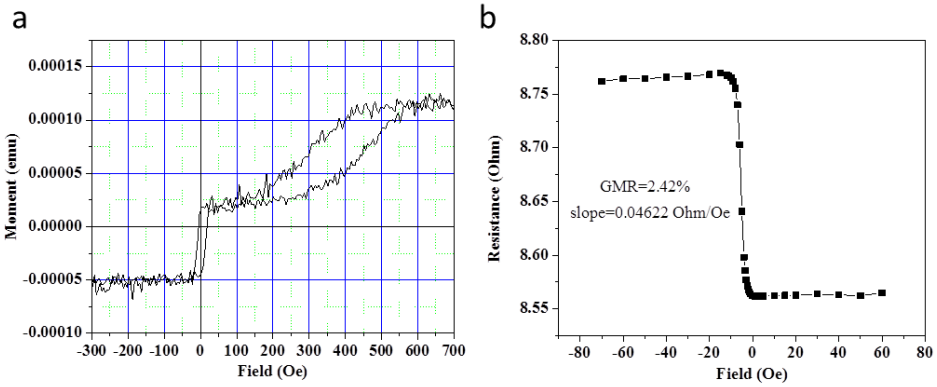

Figure 3.4 Magnetic properties of wafer level GMR stack, measured along the hard axis

a) Hysteresis loop
b) Transfer curve

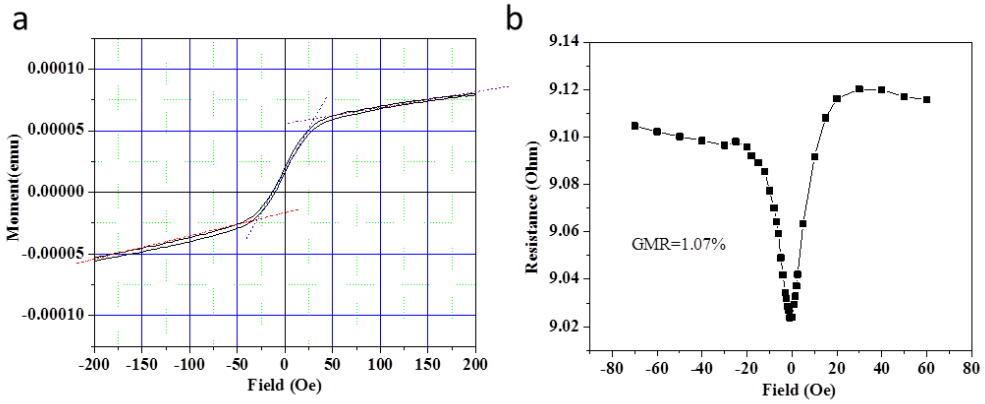

Figure 3.5 Magnetic properties of wafer level GMR stack, measured along the easy axis
a) Hysterisis loop
b) Transfer curve

3.3 Microfabrication of GMR biosensor

After thin film deposition, GMR wafer goes through microfabrication process. Figure 3.6 demonstrates the main GMR biosensor patterning processes. At first, the shape and dimension of the GMR sensor is defined through photoresist by photo lithography. Secondly, using ion milling, the pattern is transferred to GMR thin film stack to form individual GMR sensor with same size. Then the electrode is deposited to form the electrical contact, using E-beam deposition and lift-off process. After that, by using the same techniques as electrode deposition, a thick silicon dioxide layer is formed on the whole wafer, except the active sensing area of GMR biosensor. The purpose is to provide good insulation during the test because most of the GMR biosensing is operated in

solution. At last, a thin layer of silicon dioxide is deposited on top of the active sensing area, which will be utilized as a biofunctionazation layer to bind different kinds of biomolecules.

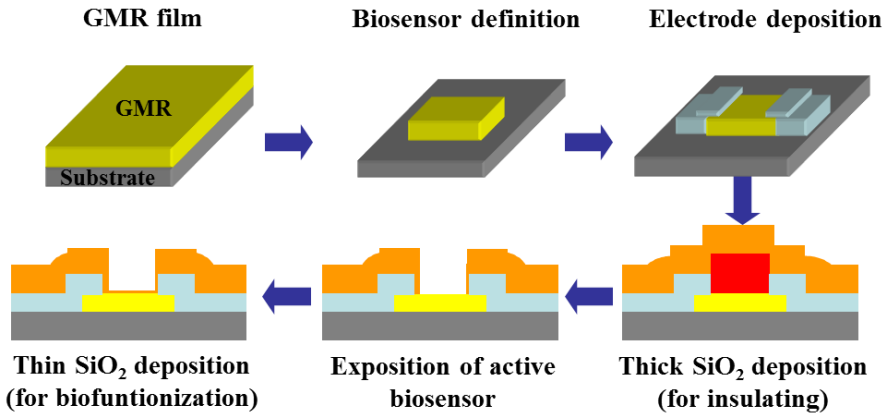

Figure 3.6 Schematic showing of GMR biosensor patterning process.

3.3.1 Wafer layout mask design

A wafer mask is typically used to define desired feature on the substrate in patterning process. For example, the geometries of GMR biosensor element, electric lead and protection layer are defined through mask in microfabrication process. Therefore, multilayer wafer layout masks need to be designed before the microfabrication of sensor chip. In biosensor chip mask design, one should consider the overall picture of patterning process, testing scheme and packaging method, particularly the way to accommodate biological sample for testing.

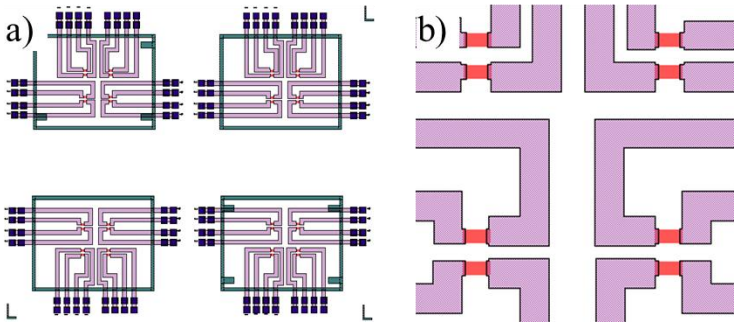

Figure 3.7 Mask design of hysteresis sensor
a) Die layout
b) Zoom in view of sensor definition

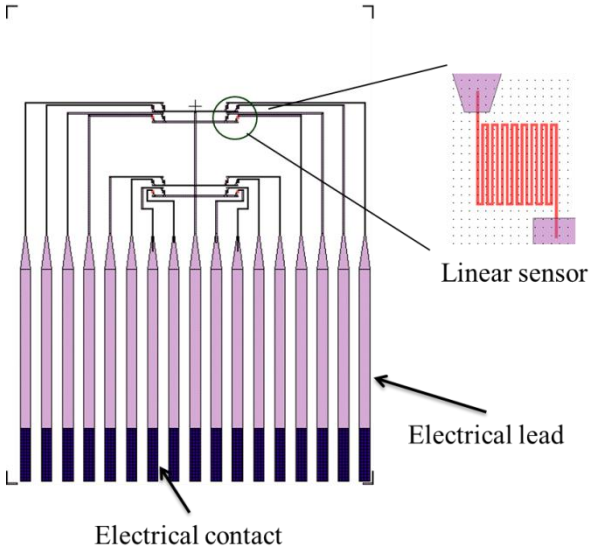

Figure 3.8 Mask design of linear GMR sensor

3.3.2 Lithography

As discussed above, the first step of patterning is to transfer device pattern onto the GMR stack wafer, where lithography technique is typically employed. What lithography does is to put down a photoresist, which has the same shape and dimension as what one defines in the mask design, onto the target substrate. There are two major lithography techniques: 1) photo-lithography; 2) e-beam lithography. Photo-lithography is relatively simpler and easier process, compared with e-beam lithography. However, e-beam lithography has much higher resolution, which ranges from submicron to tens of nanometers, than that of photo-lithography. Therefore, depending on the critical dimension of device, different lithography technique will be employed.

In this work, both photo and e-beam lithography are used. For regular hysteresis and linear sensor, as shown in Figure 3.9, the physical dimensions are both in tens of micrometers to several micrometers range. Therefore, photo-lithography is utilized to transfer device pattern onto the sensor wafer. Typically, photo-lithography includes the following steps: a) substrate preparation; b) photoresist coating; c) soft-bake; c) exposure; d) develop; e) post-bake. The wafer was first prepared by being cleaned and pre-baked at a certain temperature, which removes contamination and moisture in order to improve adhesion. Then the photoresist is spin coated onto the wafer, followed by a soft-bake to remove the solvent of the photoresist. Next step is to exposure the photoresist under UV light, with the photomask over the wafer to transfer pattern. After that, the wafer, together

with the photoresist after exposure, is submerged into developer. Depending on the type of photoresist (positive or negative), the developer would resolve the photoresist with UV exposure or without UV exposure. A post-bake process is also typically required to harden the photoresist and further improve adhesion to wafer after developing. The process for e-beam lithography is similar to that of photolithography. The major difference is on exposure step. Other than UV light exposure, e-beam lithography utilize electron beam to expose photoresist. Since the spot size of electron beam can be controlled to be very small, down to nanometer range, the resolution of e-beam lithography is capable of achieving the same pattern transfer on the same range.

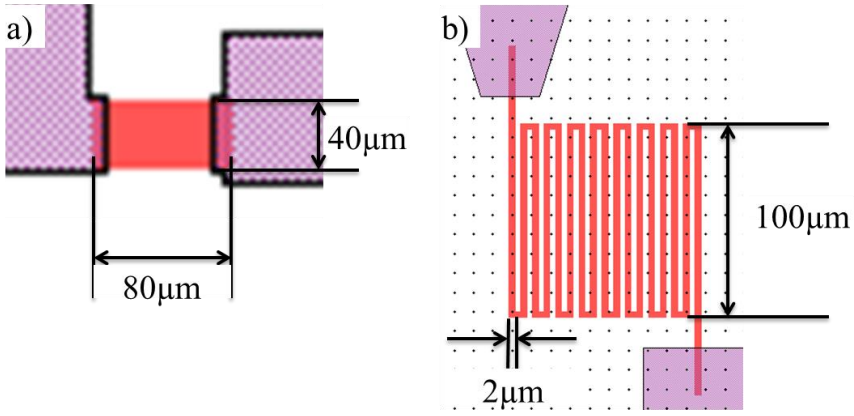

Figure 3.9 Mask designs of two types of sensor elements:
a) hysteresis sensor with 80 μm × 40 μm dimension
b) linear sensor with 100 μm × 2 μm dimension

3.3.3 Ion milling

Photolithography or e-beam lithography only transfers the designed pattern onto photoresist. To transfer the designed pattern to onto the GMR thin film wafer, ion mill is needed to etch off the unneeded portion of thin film wafer. Ion milling is a dry etching technique. In ion milling chamber, argon atoms are bombardment by electrons collectively, which are confined by a magnetic field in the chamber. The ion gas which is formed from bombardment is then accelerated by an electric field and guided towards the etching target. The final step is to use ion gas to bombard the etching target and knock out the unwanted atoms. Since ion milling is a physical bombardment process, both metal and insulation layer can be etched through ion milling. On the other hand, the etching selectivity is not as good as wet etching techniques. In addition, the heat generated in the bombardment process and the re-deposition of etching material, are also challenges to ion milling technique, which would be addressed in the ion milling process discussed later. Nevertheless, ion milling is still widely used in different application, such as the fabrication of magnetic reader, microelectronic circuit and magnetic sensor.

In GMR sensor fabrication, ion milling is utilized to etch the GMR thin film wafer with pattern photoresist. Due to the poor selectivity of ion milling, photoresist acts as a hard mask to process the sensor area. To avoid over etching, a reference thin film structure, which is deposited on a transparent plastic substrate, is placed besides the wafer to monitor the etching process. During the etching process, the ion beam is on and off for

every three minutes alternatively, to avoid the overheating of photoresist. The ion beam incident angle starts from 10 degree first. When the etching is almost finished, the ion beam incident angle is changed to 70 degree to remove the re-deposition on the sidewall of the sensor stack.

After the ion milling, the photoresist needs to be removed by photoresist remover. The photoresist through ion milling process is typically hard to remove, due to the heating process during ion milling. Sometimes, a high temperature bath with photoresist remover is preferred to completely stripe off the resist.

3.3.4 Electrical lead deposition

After sensor pattern definition, electrical leads are deposited to form electric connection between sensor and external circuit. A standard bi-layer lift-off process and ion beam deposition are the major two processes for electric lead deposition. As shown in Figure 3.10, the lift-off process starts with the spin coating of bilayer photoresist, SF-5 and 1813. Then the bilayer photoresist is exposed and developed to the pattern of electric lead. Only electric lead area is not covered with bilayer photoresist. Next, the trilayer of Ta/Au/Ta are deposited through ion beam deposition, where Au is selected due to good conductivity and Ta is used as an adhesive layer for Au deposition. Subsequently, the bilayer photoresist is removed, together with the Ta/Au/Ta deposited on top of the bilayer photoresist.

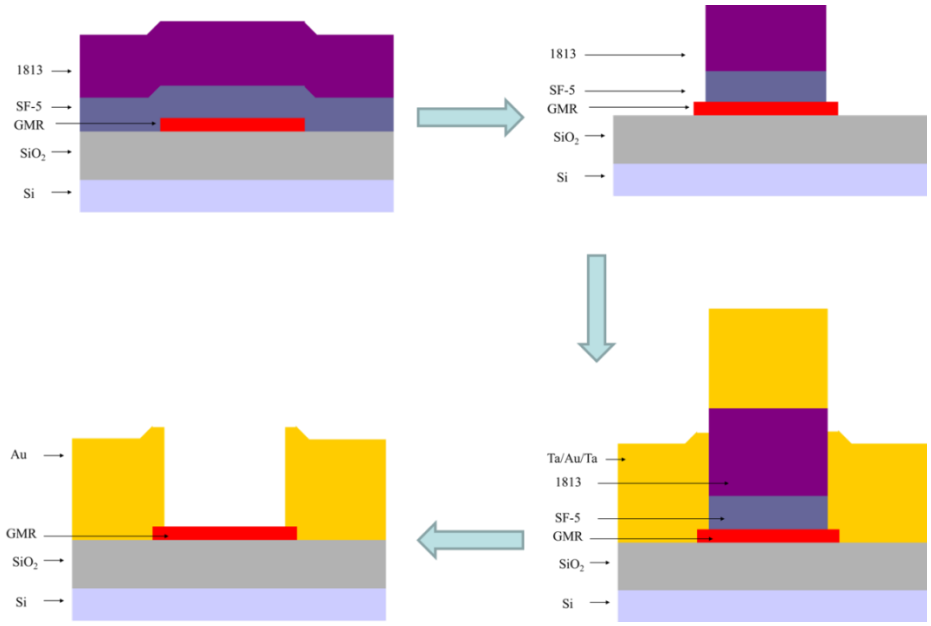

Figure 3.10 Lift-off process for electric lead deposition

3.3.5 Insulation layer deposition

Since the biodetection usually occurs in liquid environment, the insulation of electric lead and sensor is important to avoid electric breakdown of biosensing chip. As shown in Figure 3.11, a silicon oxide with around one micrometer thickness is used as the isolation layer. The silicon oxide is deposited through e-beam evaporator onto the whole wafer. And the sensor area is exposed through lift-off process. During this process, the reference sensor would be cover by the thick insolation layer, so that it would not be affected by the magnetic signal from magnetic labels.

3.3.6 Biofunctionization layer deposition

In the last fabrication process, biofunctionization layer is deposited on to the sensor. The purpose for biofunctionization layer is for bonding specific biomolecules, such as DNAs or antibodies, onto the sensor surface. Both Au and thin silicon oxide can be used as biofunctionization layer, where Au is used for DNA hybridization and silicon oxide is used to bond with antibodies. The thickness of biofunctionization layer is preferred to be as thin as possible in order to obtain better magnetic signal.

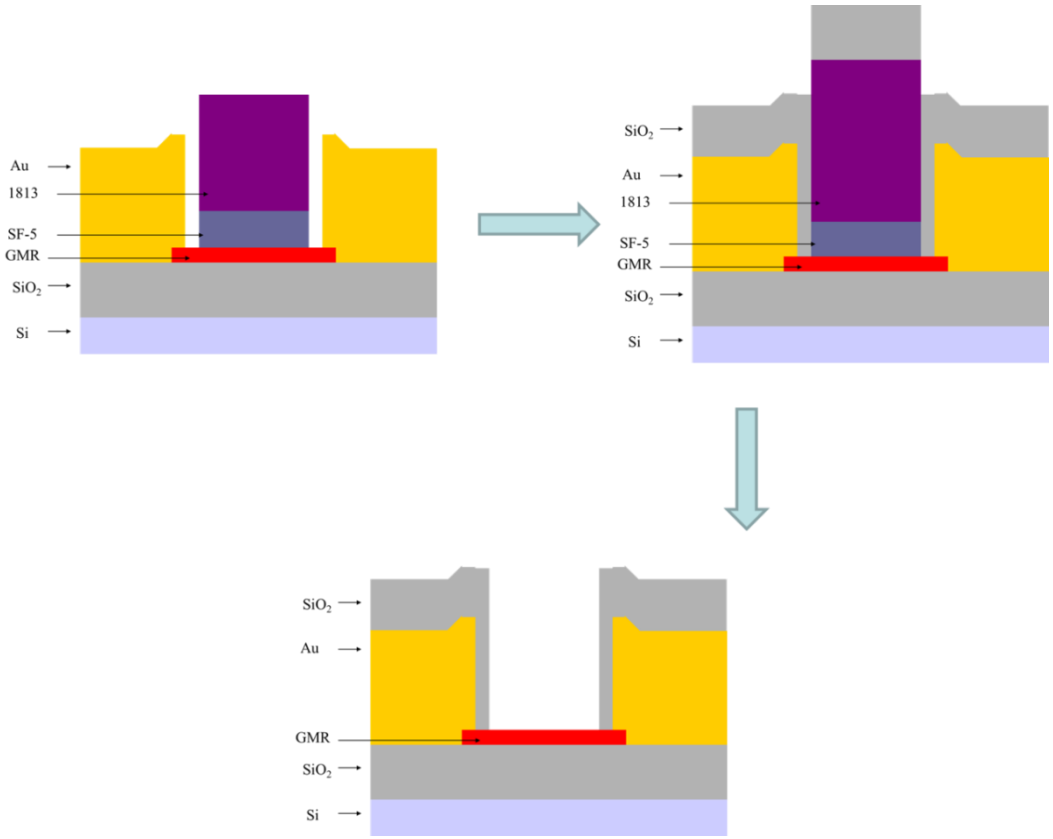

Figure 3.11 Lift-off process for isolation layer deposition

3.4 GMR biosensor measurement

3.4.1 DC method

The magnetoresistance of GMR sensor was measured using a four-probe working station. A model Keithely 2400 sourcemeter was used to measure the resistance of the GMR sensor by four wire configuration. The sensing current which runs through the GMR sensor is 1mA, while the voltage of the GMR sensor was monitored by the

Keithely 2400 sourcemeter at the same time. An external magnetic field generated by an electromagnetic coil was applied in plane to change the magnetization direction of the free layer. The second function of the external magnetic field is to polarize the magnetic nanoparticles on the GMR sensor which could generate the stray magnetic field for sensing. A self-coded labview program (National instruments, USA) was used to control the measurement system by a computer. The typical transfer curve of GMR sensor is shown in Figure 2.2.

3.4.2 AC method

Although DC method is easy and flexible to set up, it has some drawbacks, such as incompatibility of real time detection and high 1/f noise. AC detection, on the other hand, is more flexible to integrate with microprocessor and processing circuit for mobile device.

1/f noise in magnetic sensor originates from both nonmagnetic part and magnetic part. Nonmagnetic part of 1/f noise is from contact noise, while the magnetic part is due to the magnetic fluctuation in the sensor resulting from thermal noise. To address this issue, de Boer *et al.* proposed mixing frequency method in 2007[26]. The main idea is try to move the detection frequency away from low frequency region, where 1/f noise is dominant. The most straightforward way is to run a high frequency AC current through sensor, so that the detection frequency of sensing signal is the AC current frequency. However, it

results in a crosstalk signal at the AC current frequency, which is in orders of magnitude higher than the sensing signal. The solution is then to apply an AC magnetic field with a frequency different from AC current frequency. Therefore, the GMR sensing signal can be expressed by:

$$V_{GMR}(t)=I_{GMR}(t)(R_0+\Delta R)$$

$$=I_0\cos(2\pi f_s t)(R_0+\Delta R_0\cos(2\pi f_s t))$$

$$=I_0R_0\cos(2\pi f_s t)+\frac{1}{2}I_0\Delta R_0\cos(2\pi(f_s-f_e)t)+\frac{1}{2}I_0\Delta R_0\cos(2\pi(f_s+f_e)t)$$

where R_0 is the DC part of sensor resistance, ΔR_0 is the variable part of the sensor resistance with magnetic field, I_0 is the amplitude of AC current, f_s is the frequency of AC current and f_s is the frequency of AC magnetic field. As shown in Figure 3.12, modulation signal (side tones) is the signal without the crosstalk interference. By using a high pass or band pass filter, 1/f noise could then be removed.

However, in mixing frequency method, the signal analog resolution is defined by the resolution of analog to digital convertor (ADC). As shown in Figure 3.12, the overall sensing signal is dominated by excitation current signal (carrier tone), while the side tones are typically a few percentages of carrier tones (MR ratio). Therefore, carrier tone suppression is the key to improve signal analog resolution. Traditionally, a wheatstone bridge would be employed to suppress the carrier, combining the reference sensor. However, since the resistance of sensors in an array could be varied, the wheatstone

bridge could not suppress carrier tone completely. We propose an adaptive referencing scheme, as shown in Figure 3.13. The carrier tone of each sensor would be obtained and suppressed by a programmable reference signal, whose amplitude and phase is the same as the carrier tone of the original sensor. Data acquisition card (NI USB-6289) is used for both tone detection and reference signal generation.

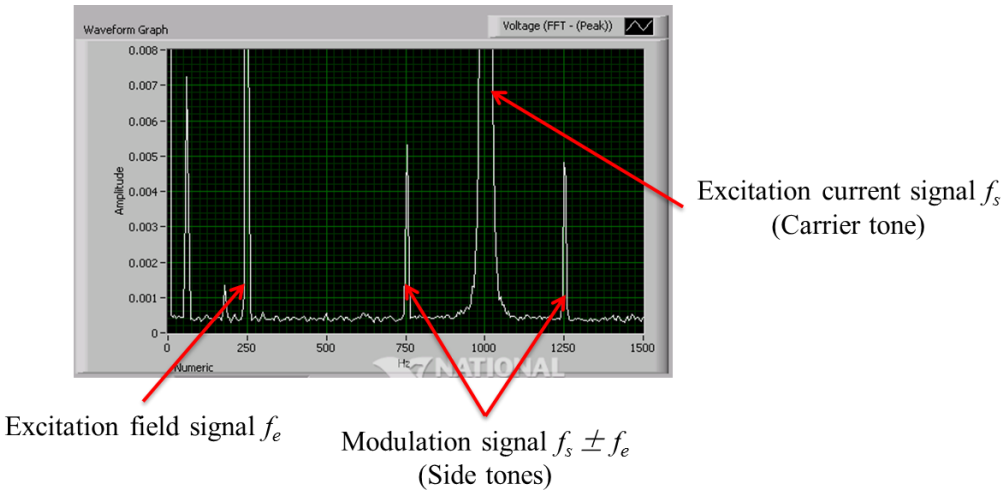

Figure 3.12 frequency domain of mixing frequency method

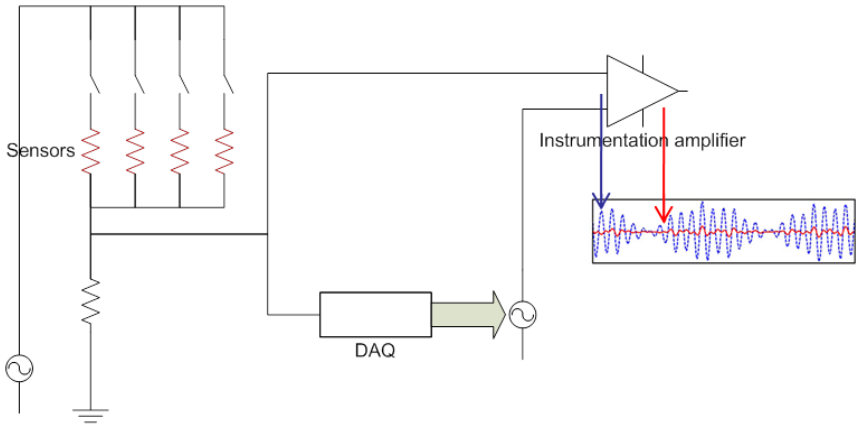

Figure 3.13 Schematic drawing of adaptive referencing scheme

.

Chapter 4 Application of GMR Magnetic Biosensing System

4.1 Zeptomole sensitivity demonstration of interleukin 6 detection

4.1.1 Introduction

Longitudinally monitoring the changes of protein biomarkers (generally < pmol)[74] is expected to help design medical treatment for specific individuals[15] and detect chronic diseases in their early stage, which is critical to achieve successful personalized medicine and control of chronic diseases.[1] This requires a highly sensitive detecting system that is of low-cost, easy to use, does not require expensive instruments, and preferentially compatible with current electronic technologies. Since the late 1990s, magnetoelectronics,[75-77] including GMR sensor,[27] has emerged as one promising platform to meet such requirements.[63,65,67,78-80] In principle, a GMR sensor would detect magnetic stray fields resulted from magnetic labels on the sensor surface (Scheme 1). Several studies have demonstrated the usage of magnetic biosensors to detect biomolecules with relatively large particle labels (> 250nm).[67,69,78-82] The high mass and size of the label in relation to biomolecules to be tethered is expected to interfere with the natural biomolecule movement, recognition, and binding, which would be less serious with small-sized magnetic nanoparticles. However, magnetic nanoparticles as detectable labels acquire a smaller magnetic moment than the larger ones, requiring more sensitive sensors

and measurement systems. Although the detection of tens of 16 nm iron oxide nanoparticles by direct placement on GMR sensor surface was demonstrated,[83] usefulness in real biological system is not studied. Therefore, use of small magnetic nanoparticles for sensitive detection and quantification of biomolecule are yet to be realized.[67,78-80]

In this section, the development of a highly sensitive detection system based on a GMR sensor and 12.8nm high moment cubic FeCo nanoparticles is reported, which linearly detects 600 - 4500 copies of streptavidin based on biotin-streptavidin interaction (Figure 4.1). The feasibility of this detecting system for real biological applications is demonstrated, with the example of the linear detection of human interleukin 6 (IL-6, a potential lung cancer biomarker) through a sandwich-based principle. These results have been published as "A Detection System Based on Giant Magnetoresistive Sensors and High-Moment Magnetic Nanoparticles Demonstrates Zeptomole Sensitivity: Potential for Personalized Medicine", Srinivasan, B. *et al*. Angewandte Chemie International Edition 48, 2764-2767, (2009).

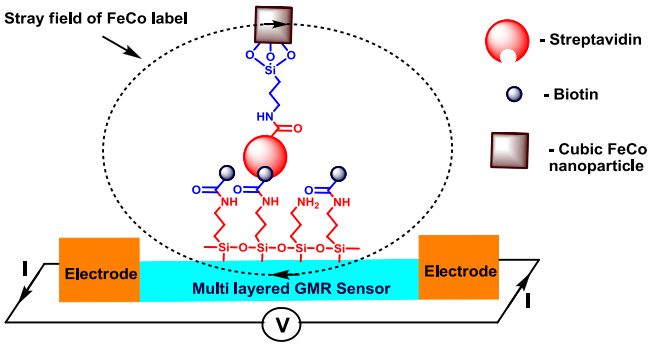

Figure 4.1 GMR sensor for detection of molecular recognition

4.1.2 GMR sensor fabrication and surface modification

A multilayer GMR structure of Ta (5nm) /$Ir_{0.8}Mn_{0.2}$ (10nm) /$Co_{0.9}Fe_{0.1}$ (2.5nm) /Cu (3.3nm) /$Co_{0.9}Fe_{0.1}$ (1nm) /$Ni_{0.82}Fe_{0.12}$ (2nm) /Ta (5nm) was deposited on thermal oxide silicon wafer using a six-target Shamrock sputtering system. After the deposition of GMR multilayer structures, a layer of photoresist 1813 was spin-coated on the wafer using Brewer CEE resists spinner 100. Then the wafer was exposed through a mask which defines the GMR sensor shape using a Karl Suss mask aligner for 5.5 seconds. After the development of photoresist 1813, the wafer was ion milled into a rectangle shape at an angle of 60 degree and 70 degree in order to obtain a sharp edge. After the removal of the photoresist 1813, a total 210nm Ta/Cu/Ta multilayer was deposited on the wafer by the shamrock sputtering system. This multilayer structure was patterned by lift-off process and used as the electrodes of the GMR sensors. In order to obtain a proper surface for bio-modification, an 11.4nm SiO_2 layer was deposited and patterned on the GMR sensor area using a lift-off process. The rest of the wafer except the electrode area was passivated by 1 μm thick silicon dioxide. Finally, the wafer was post annealed at 280℃ for 40 minutes under 4000 Oe magnetic field in order to pin the fixed magnetic layer. Figure 4.2 shows a scanning electron microscope (SEM) image of the GMR sensor

with a lateral dimension of 80 μm x 40 μm after the patterning. GMR sensor chip design layout is shown in Figure 4.3.

GMR sensor surface was sequentially modified first with 3-aminopropyltriethoxysilane (APTES) followed by Chromalink® biotin (Figure 4.4). Chromalink biotin succinimidyl ester was chosen over biotin succinimidyl ester for biotinylation modification, because the former has a chromophoric group for quantification purposes.

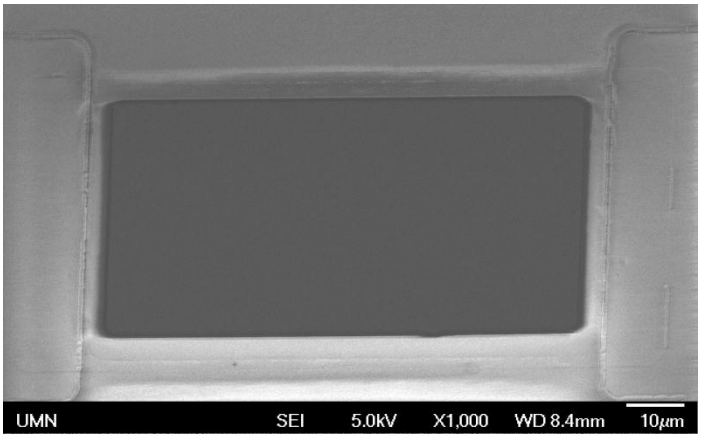

Figure 4.2 SEM image of GMR sensor

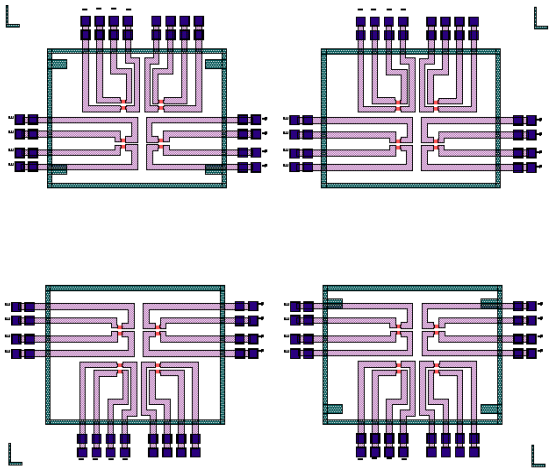

Figure 4.3 GMR sensor chip design layout.

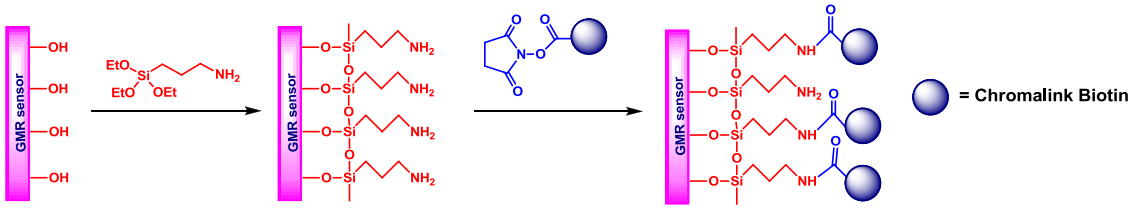

Figure 4.4 Illustration of GMR sensor surface modification

4.1.3 Estimation of the number of FeCo nanoparticles:

Estimation of FeCo nanoparticle concentration in a dispersion of an unknown concentration was determined by completely digesting them in hydrochloric acid in the presence of oxidant like hydrogen peroxide to convert Fe to Fe(III) and measuring absorbance at 340nm. A known quantity of FeCo materials (50-100mg) was taken in a 10ml vial. To this, 1ml of 30% v/v HCl and 1ml of 30% hydrogen peroxide were added.

The reaction mass gradually turns greenish brown and finally brown in color. The reaction is exothermic and starts boiling on its own and hence intermittent cooling may be needed to control the reaction. The reaction mass was allowed to stand for 6h at room temperature. After that, it was made up to 25ml in volume using DI water. Using this stock, 0.008M solution was made in a 50ml SMF. From this, serial dilution was made to obtain various concentrations. Absorbance was measured at 340 nm using a 96 well plate reader. A standard calibration curve was established (Figure 4.5).

FeCo nanoparticles were deposited on PEG coated glass slides during the preparation process. Then the nanoparticles were washed off from the glass slides into a vial using DI water and made up to 3ml at a concentration approximately 100-150 µg/ml in DI water (based on density calculations using TEM image). The nanoparticles in 250 µL solution were collected by an external magnet field. To these particles, 100 µL of 30% HCl and 100 µL of hydrogen peroxide were added carefully. Reaction mass was allowed to stand for 6h. After that, the final volume was made up to 300 µL. Absorbance at 340 nm was measured. Two more experiments were carried out similarly. Based on absorbance, the concentration of FeCo was calculated using the standard curve. Results showed that concentration of our initial stock is 87.324 ±0.599 µg/ml.

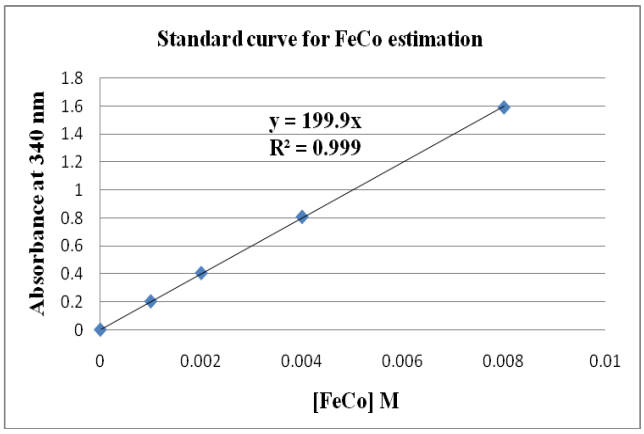

Figure 4.5 Standard calibration curve for FeCo estimation

	Quantity of FeCo NPs in stock (μg/ml)
Absorbance at 340 (nm)	
0.255 ± 0.002	87.1 ± 0.5

Table 4-1 FeCo estimation (mean ± SD; n=3)

4.1.4 FeCo nanoparticle surface modifications

FeCo nanoparticles were first modified with amino groups on the surface by using APTES (Figure 4.6), which resulted in ~ 660 APTES molecules on each nanoparticle. APTES modified nanoparticles were subjected to streptavidin-AF488 modification using 1-ethyl-3-(3-dimethylaminopropyl)-carbodiimide (EDC) coupling chemistry. It is estimated that each NP is modified by 1.3 streptavidin-AF488 molecules. There is no significant non-specific binding of streptavidin to the magnetic nanoparticles. These data suggest that most particles are likely to be modified by 1 copy of streptavidin molecule. TEM images of APTES modified and streptavidin modified NPs were shown in Figure

4.7, demonstrating no significant particle aggregation. This is again critical for quantification of biomolecules, which is based on the magnitude of magnetic signals from nanoparticles

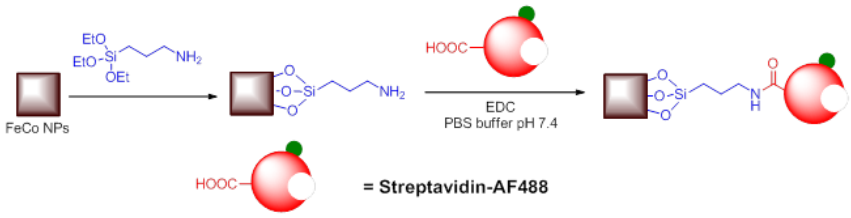

Figure 4.6 Illustration of nanoparticle modification

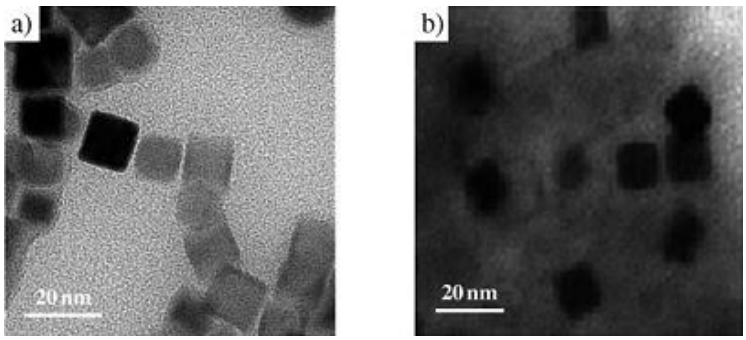

Figure 4.7 TEM images of FeCo nanoparticles modified by a) APTES and b) streptavidin-AF488.

To demonstrate the incorporation of ATPES on FeCo nanoparticles, aqueous solution of bare FeCo nanoparticles and APTES modified FeCo nanoparticles were applied on carbon film coated copper grids. Energy dispersive X-ray spectra (EDX) was taken on field emission gun transmission electron microscope (FEI Tecnai G2 30). Strong signal of Si in the ATPES modified FeCo NPs sample confirmed the successful modification

(Figure 4.8) while the very weak signal of Si detected in bare FeCo NPs sample was within random error range (Figure 4.9).

4.1.5 Biotin-Streptavidin detection

To explore the sensitivity of this GMR sensor- and magnetic nanoparticle-based detecting system, varied quantities of streptavidin-AF488 modified magnetic nanoparticles were applied onto the surface of GMR sensor modified by Chromalink® biotin. After thorough wash to remove the potentially unbound streptavidin, the magnetic signals from the magnetic nanoparticles specifically retained on the GMR sensor through biotin-streptavidin interactions were measured by the GMR sensor.

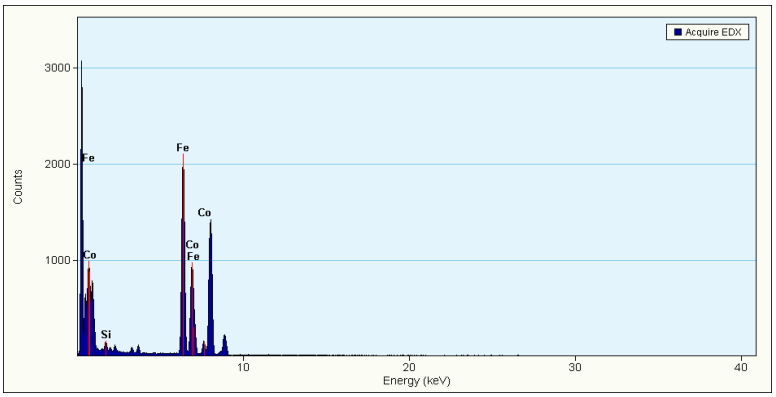

Figure 4.8 TEM-EDX spectra of bare FeCo NPs dispersion in water

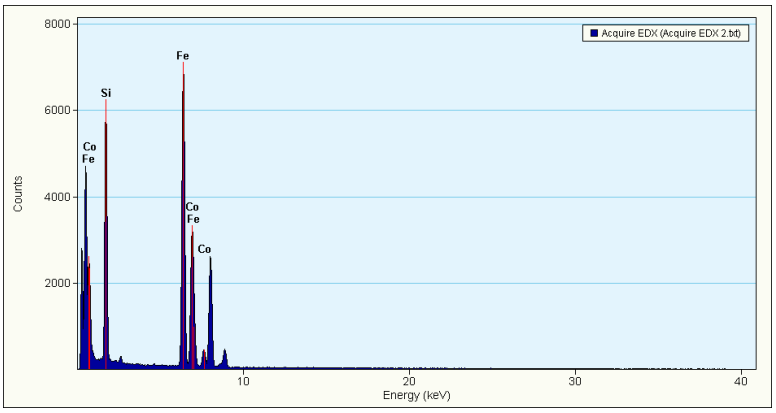

Figure 4.9 TEM-EDX spectra of APTES modified FeCo NPs dispersion in water

As shown in Figure 4.10 (a), the GMR sensor detected signals from as low as 600 copies (< 10^{-21} mol, zeptomol) of streptavidin, the sensitivity of which is expected to detect all potential biomarkers from 10 nanoliter or less body fluid. More importantly, there is a linear dose-response relationship of the amount of streptavidin applied and the magnetic signals detected by the GMR sensors. Such a dynamic range of linearity outperforms most other GMR based detecting systems reported to date, making accurate quantification possible. The signal detected on biotin modified GMR sensor is introduced through the biotin-streptavidin interaction as the control sensors with no biotin modification detected no resistance changes under the identical experimental conditions.

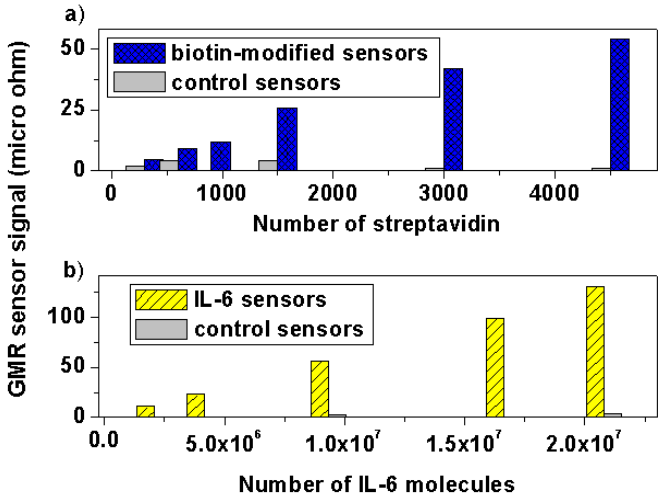

Figure 4.10 GMR sensor signal of streptavidin and IL-6
a) Resistance change for different amounts of streptavidin molecules on the GMR sensor. Blue: GMR sensors with surface modified by biotin. Gray: GMR sensors with no biotin modification. b) Resistance change detected by sensors for different amounts of IL-6 molecules modified on the sensors using a sandwich structure. The same amount of capture antibody and detection antibody-modified magnetic nanoparticles was applied to each sensor with varied numbers of IL-6 molecules. Yellow: IL-6 modified GMR sensors. Gray: GMR sensors with no IL-6 modification.

4.1.6 Human interleukin-6 detection

To further explore the practical usage of this GMR sensor-magnetic nanoparticle-based detecting system, we evaluate the potential of this system to detect human interleukin-6 (IL-6, a potential serum biomarker for lung cancer) using a sandwich approach, which follows the same principle of Enzyme-Linked ImmunoSorbent assay (ELISA). Monoclonal anti-human IL-6 antibody (capture) was covalently attached to APTES modified GMR sensor using EDC coupling chemistry. Recombinant human IL-6

is allowed to bind to capture antibody on the GMR sensor surfaces. Polyclonal anti-human IL-6 antibody (detection) was magnetically labeled with APTES modified FeCo nanoparticles through covalent linkage in a 1.19:1 fashion. Magnetic particle labeled detection antibody was allowed to bind IL-6 bound sensor surface.

As shown in Figure 4.10 (b), the GMR sensor detected signals from as low as 2.08×10^6 IL-6 molecules. The sensitivity for IL-6 ELISA assay (R&D, D6050) is 2.79×10^7 IL-6 molecules, which is 13 times less sensitive than our un-optimized GMR sensor- and magnetic nanoparticle detecting system. More importantly, there is a linear dose-response relationship between the amount of IL-6 applied and the magnetic signals detected by the detecting system. Currently work is undertaken in our laboratory to optimize the sandwich assay conditions to improve the sensitivity and dynamic detecting range.

4.1.7 Conclusion

In conclusion, we have established a GMR sensor- and high-moment magnetic nanoparticle-based detecting system that, for the first time, detects as few as 600 copies of streptavidin, which is modified by 12.8nm cubic FeCo nanoparticle in a 1:1 ratio. We also demonstrated that this detecting system can adopt the principle of ELISA assay with increased sensitivity. GMR and magnetic nanoparticle based detecting system is expected to be applicable to many other biological systems for detection and quantification of

various biomolecules. The high sensitivity of this detecting system open new avenues for the detection of biomolecules involved in the etiology of various diseases, especially the chronic ones, such as cancer, which is now under investigation. It can also be used to monitor residual disease and disease reoccurrence. Most importantly, because of the magnetic/electric nature of this detecting system, we expect that this detecting system will help the realization of point-of-care.

4.2 Competition-based nanomagnetic assay for low-abundance protein biomarker quantification in unprocessed human sera

4.2.1 Introduction

Traditional technologies for disease biomarker detection are enzyme-linked immunosorbent assays (ELISA)[84,85], Western Blotting, immunohistochemistry, DNA based genomics, and mass spectrometry based proteomics and metabolomics[86]. With no exception, these approaches have intrinsic common limitations, including expensive equipment, long processing time, extensive professional training, and low signal-to-noise ratio[22]. Methods that can rapidly and specifically quantify disease biomarkers from human unprocessed body fluids with low cost are expected to greatly facilitate disease biomarker validation and disease early detection. Sensing based on the combination of GMR sensors and magnetic nanoparticles has attracted much attention as a promising alternative[23-28,56,57,63,64,67,68,72,87-91]. Nevertheless, most GMR biosensor application has

been confined to proof of detecting concept[64,67,68,88], model studies[89,90], or detection of spiked biomolecules, the concentration of which generally are orders of magnitude higher than the physiological relevant ones[24,72,91], mainly because its theoretical sensitivity has not been achieved under physiological conditions.

This study reports the first realization of specific, accurate, and rapid quantification of interleukin-6 (IL-6), a low-abundance protein and a potential cancer biomarker[92], in unprocessed human sera, by employing our novel near 0-degree GMR sensor with our uniform high-moment magnetic nanoparticles and minimizing the detecting distance between nanoparticles and GMR sensing. Such integration led to significant increase of detecting sensitivity and accuracy. The near 0-degree design of the GMR sensor also eliminates the need of a high magnetic field for detection, which open the opportunity for portable device. Our platform therefore has a significant impact for magnetic sensor-based biomolecule detection with the potential to develop a lab-on-chip device, practical for frequent biomarker detection and monitoring. These results have been published as "Nanomagnetic Competition Assay for Low-Abundance Protein Biomarker Quantification in Unprocessed Human Sera", Li, Y. *et al*. Journal of the American Chemical Society 132, 4388-4392, (2010).

4.2.2 Three-layer and two-layer approaches

The methodology of GMR biosensor and magnetic nanoparticle-based family medical device, in case of protein detection, includes two basic detection schemes: three-layer approach and two-layer approach. As shown in Figure 4.11 (A), three-layer approach contains the following steps: the GMR biosensors are first functionalized with capture antibodies specific to the analyte; then analyte are applied onto the GMR biosensor and followed by the magnetic nanoparticle labeled (MNL) detection antibodies; finally, the analyte are sandwiched by the capture antibody and MNL detection antibody. By detecting the bond magnetic nanoparticles by GMR biosensor, the captured analyte can be quantified. Alternatively, two-layer approach, as illustrated in Figure 4.11 (B), only requires the direct application of MNL analyte onto the capture antibody modified sensor. Although based on different modification steps, these two approaches share the same magnetic nanoparticle detection principle. Since the magnetic nanoparticle used for labeling is superparamagnetic, the magnetic dipole field $\boldsymbol{H_{dip}}$ of the superparamagnetic nanoparticle is given:

$$\boldsymbol{H}_{dip} = \frac{3(\boldsymbol{m}\cdot\boldsymbol{r})\boldsymbol{r}}{r^5} - \frac{\boldsymbol{m}}{r^3}$$

where $\boldsymbol{r}$ is the space vector pointing from the center of superparamagnetic nanoparticle to the point where the field is measured, $\boldsymbol{m}=V\chi\boldsymbol{H_a}$ is the magnetic moment of the

superparamagnetic nanoparticle under the applied field $\boldsymbol{H_a}$, V is the volume of the superparamagnetic nanoparticle and χ is the susceptibility of the superparamagnetic nanoparticle. Hence, the effective magnetic field $\boldsymbol{H_{eff}}$ on the sensor considering the dipole field from the nanoparticles is $\boldsymbol{H_{eff} = H_a - H_{dip}}$. Because the resistance of GMR biosensor responses easily to the in-plane magnetic field, the magnetic dipole field from the nanoparticle could be picked up by the GMR biosensor, which is represented by the change of sensor resistance after the magnetic nanoparticle binds to the sensor surface. From equation 5.1, it is clear that the detection signal is highly sensitive to the distance between the magnetic nanoparticle and the GMR biosensor. Therefore, the sensitivity of this system is expected to be improved by adopting two-layer approach since the magnetic nanoparticle is closer to the GMR biosensor than that in three-layer case.

Since the dipole field is much smaller than that with the applied field, we can assume a linear relationship between the resistance R and the effective magnetic field:

$$R = C \cdot H_{eff}$$

where C is a coefficient. For a bare GMR sensor, the effective magnetic field on the sensor is just the applied field. So the resistance of the sensor R_0 in this case is:

$$R_0 = C \cdot H_a$$

After the nanoparticle attachment, the effective magnetic field on the sensor considering he dipole field from the nanoparticles is $\boldsymbol{H_{eff} = H_a - H_{dip}}$. Hence, the resistance of the sensor R_1 is:

$$R_1 = C \cdot H_{eff}$$
$$= C \cdot (H_a - H_{dip})$$

Therefore, the sensing signal *S* is defined as the resistance different with and without nanoparticle attachment:

$$S = R_0 - R_1$$
$$= C \cdot H_a - C \cdot (H_a - H_{dip})$$
$$= C \cdot H_{dip}$$

The sensitivity improvement is defined as the ratio of sensing signals in two-layer case S^b and three-layer case S^s:

$$\frac{S^b}{S^s} = \frac{C \cdot H_{dip}^b}{C \cdot H_{dip}^s}$$
$$= \frac{H_{dip}^b}{H_{dip}^s}$$
$$= \frac{\frac{m}{(r^b)^3}}{\frac{m}{(r^s)^3}}$$
$$= (\frac{r^s}{r^b})^3$$

where r^s and r^b is the distance between the center of magnetic nanoparticle and the sensor surface in three-layer and two-layer structure, respectively. Assuming the capture antibody, IL-6 and detection antibody vary size from 3nm to 30nm[93], then we can calculate the dynamic range of sensitivity improvement. For the maximum sensitivity improvement, we consider: a three-layer structure of 3nm capture antibody, 3nm IL-6 and 30nm detection antibody; a two-layer structure of 3nm capture antibody and 3nm IL-6. For minimum sensitivity improvement, we consider: a three-layer structure of 30 nm

capture antibody, 30nm IL-6 and 30nm detection antibody; a two-layer structure of 30nm capture antibody and 30nm IL-6. Therefore, the dynamic range of the sensitivity improvement is from 3.4 up to 39.3.

Currently, most GMR detection of protein-based biomolecules in publications employs a three-layer (sandwich)-based approach, which compromises the detection sensitivity to the whole system. To demonstrate the sensitivity improvement experimentally, we explored the sensitivity of this system for human IL-6 detection, a potential serum biomarker for lung cancer, employing both three-layer and two-layer approaches. In this paper, the binding efficiency of capture antibody, detection antibody and IL-6 were optimized in order to maximize the sensor sensitivity. As shown in Figure 4.12 as low as 20.76 pM IL-6 molecules were detected based on three-layer approach, while two-layer approach increases the sensitivity of this system up to the detection of 373 fM MNL IL-6 molecules, which is around 50 times more sensitive to the three-layer approach. The sensitivity increase in two-layer case is mainly due to smaller distance between the magnetic nanoparticles and the GMR biosensor.

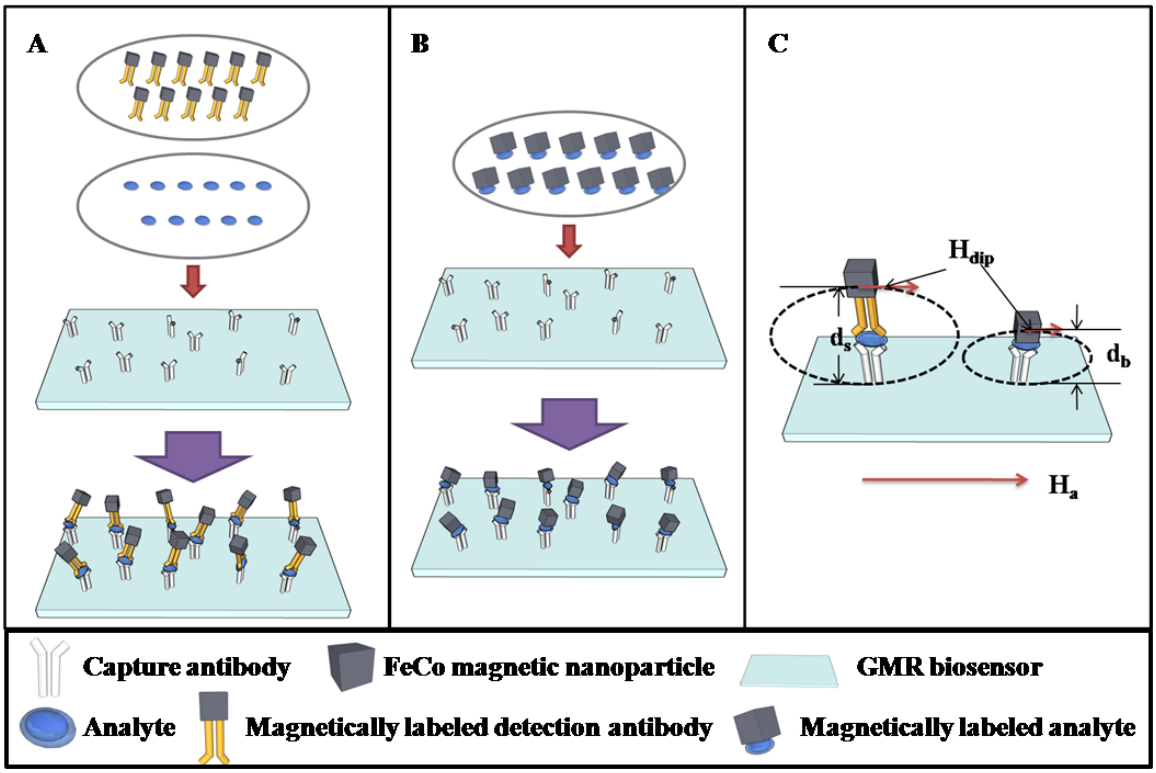

Figure 4.11 Two GMR sensor and magnetic nanoparticle-based biomolecule detection schemes.
(A) Three-layer (Sandwich) approach: the GMR sensors are first functionalized with capture antibodies. The analyte binds to the capture antibody. Subsequently, detection antibodies labeled with magnetic nanoparticles are then applied and bind to the captured analyte. (B) Two-layer approach: after the functionalization of the GMR sensor with capture antibodies, the magnetic nanoparticle modified analyte is directly applied and captured on the GMR biosensors. (C) GMR biosensor working principle. The GMR biosensor can detect the dipole field generated by the magnetic nanoparticles captured on the sensor surface, which is sensitive to distance.

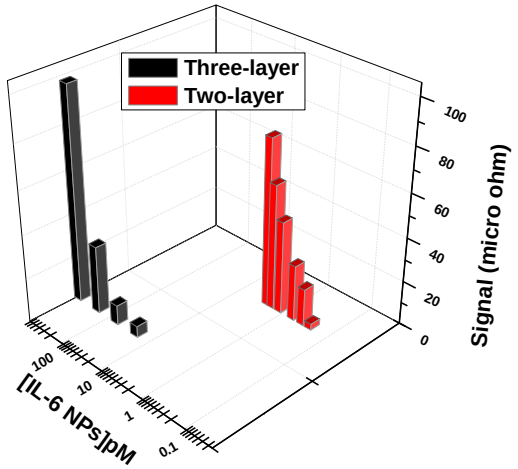

Figure 4.12 Sensitivity comparison between three-layer and two-layer approaches. Dose response curves of three-layer approach and two-layer approach are shown. For three-layer approach, the same amount of detection antibody modified FeCo magnetic nanoparticles were applied to each sensor with different amounts of unlabeledIL-6 molecules. For two-layer approach, different amount of FeCo MNL IL-6 molecules were applied on each sensor.

4.2.3 Two-layer Based Competition Detection Scheme

To test unprocessed real biological sample directly, we propose two-layer based competition detection scheme. Although high sensitivity can be achieved based on two-layer approach as discussed above, it requires labeling target analyte with magnetic nanoparticle in the testing sample, which decreases the feasibility of the GMR biosensing system. The competition detection scheme (Figure 4.13) enables the quantification of unlabeled analyte through the detection of MNL analyte. In addition, as shown in Figure 4.14, non-competition based detection scheme may result in non-monotonic solution, if

the capture antibody or MNL detection antibody is not sufficient to the analyte. Therefore, an estimation of the analyte would be preferred to avoid such situation. However, in the case of competition detection scheme, the monotonic of detection result can always be achieved due to the nature of competition dose response curve (Figure 4.15). Following the two-layer approach, the MNL analyte are mixed with unlabeled analyte in the real sample and the mixture is applied on the same capture antibody functionalized GMR biosensor. The MNL and unlabeled analyte will compete with each other for limit amount of binding sites of capture antibodies with different efficiencies. As proof of concept, we quantified the IL-6 molecules using the competition scheme. The mixture of 4.15 pM MNL IL-6 molecules and varied amounts of unlabeled IL-6 was applied on the GMR biosensors. Figure 4.13 (b) shows the dose response curve of the competition detection scheme, which provides a large dynamic detection range from 125 fM to 41.5 pM unlabeled IL-6 molecules. This improvement is contributed from the fact: the less unlabeled IL-6 in the mixture, the more MNL IL-6 binding to the GMR biosensor, generating more magnetic signal for enhanced signal-to-noise ratio.

4.2.4 Unprocessed Human Serum Sample Quantification

We conducted the quantification of IL-6 molecules in real human serum samples using two-layer based competition detection scheme. Ten human serum samples were evaluated. Five of them were from healthy individuals, which were labeled as NS1 to

NS5. The other five were from lung cancer patients, labeled as CS1 to CS5 (Table 4-2). Briefly, MNL IL-6 molecules were mixed with these unprocessed human serum sample (4 μL) and applied onto the GMR sensor surface (MNL IL-6 at a concentration of 4.15 pM in 4nL unprocessed human serum samples per sensor area). The concentration of IL-6 in the human serum samples was determined by using the above established competition-based dose response curve (Figure 4.13). Figure 4.16 compares the levels of IL-6 in human sera quantified by our GMR biosensor and those by commercial ELISA (R&D systems). Significant amount of IL-6 can be detected and quantified by our GMR biosensor in all ten unprocessed serum samples, while ELISA failed to detect IL-6 in four of the five sera from healthy individuals, NS2-NS5. The levels of IL-6 in sera NS1, CS2-CS5 quantified by our GMR sensor are comparable to those determined by ELISA. However, there is a significant discrepancy of IL-6 abundance in unprocessed serum CS1 between the results from ELISA (2.42×10^4 fM) and our device (1.96×10^5 fM). We hypothesize that the IL-6 level in CS1 is relatively high that it is out of the linear detecting range of ELISA and that the result from ELISA underestimates the quantity of IL-6 in CS1. To test this hypothesis, serum CS1 was diluted 80 times so that the level of IL-6 would be within the linear detecting range of ELISA based on our GMR data. The diluted sample was then re-evaluated by ELISA. The ELISA result from this diluted measurement (1.92×10^5 fM) agreed nicely with our GMR data (Figure 4.16, Table 4-3), demonstrating the accuracy and wide detecting range of our GMR biosensor-based

detecting system. Excitingly, the levels of IL-6 in the five sera from lung cancer patients are all significantly higher than those in the sera from healthy individuals, preliminarily supporting IL-6 as a potential lung cancer biomarker.

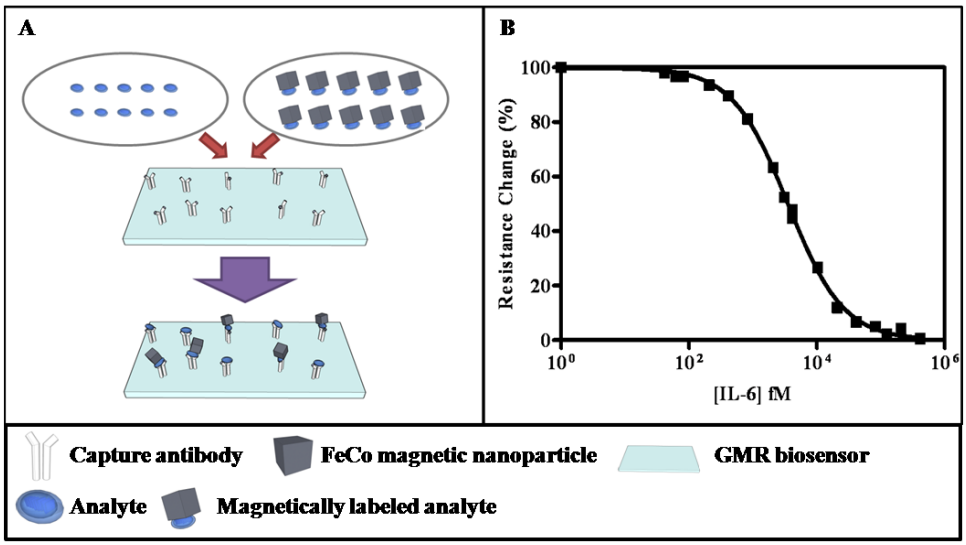

Figure 4.13 Two-layer based competition detection scheme
(A) Competition-based two-layer based detection scheme: the magnetic MNL IL-6 and unlabeled IL-6 are applied on the capture antibody functionalized GMR biosensor and compete for the binding sites. (B) Two-layer based competition dose response curve between 4.15 pM FeCo MNL IL-6 and varied concentrations of unlabeled IL-6 molecules. The solid curve is the non-linear dose fitting curve.

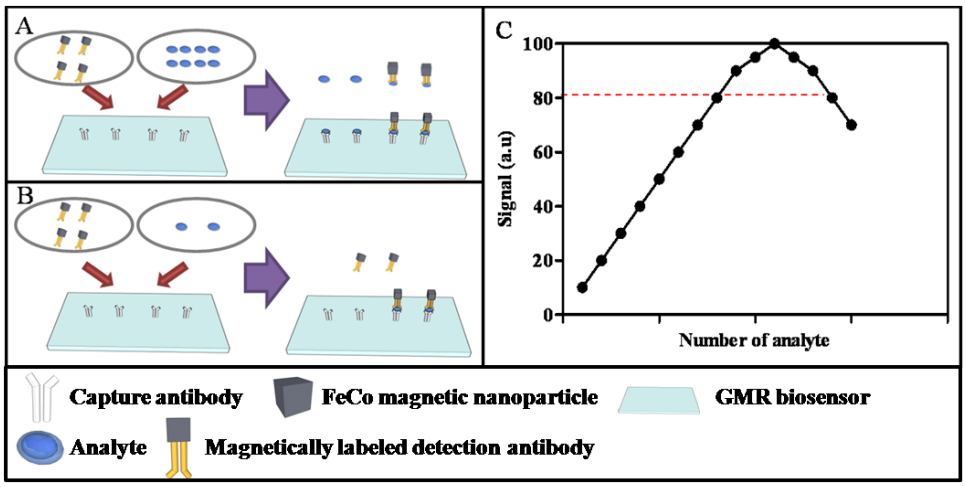

Figure 4.14 The non-monotonicity in three-layer detection scheme for unknown samples.
In case of high concentration (A) and low concentration (B) sample, same amount of magnetic nanoparticles could be bond on the surface and generate same signals (C). (The red line is the guide for eyes)

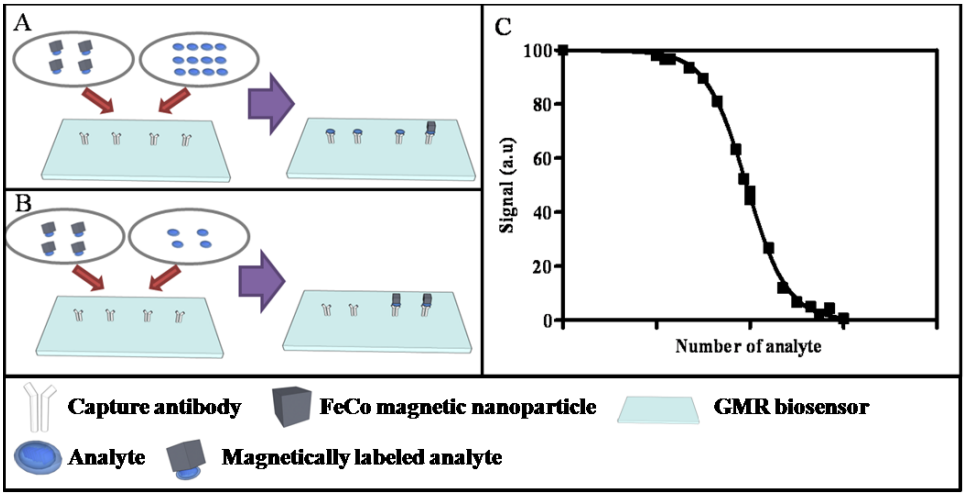

Figure 4.15 The monotonicity in two-layer based competition detection scheme for unknown samples.
In case of high concentration (A) and low concentration (B) sample, the system will generate different signal (C).

Serum sample	NS1	NS2	NS3	NS4	NS5	CS1	CS2	CS3	CS4	CS5
Promedd x number	11290266	11290268	11290306	11290595	11290624	10669752	11201397	11230619	11275849	11275852
Cancer Type	No cancer	No cancer	No cancer	No cancer	No cancer	Lung	Lung	Lung	Lung	Lung

Table 4-2 human serum samples details

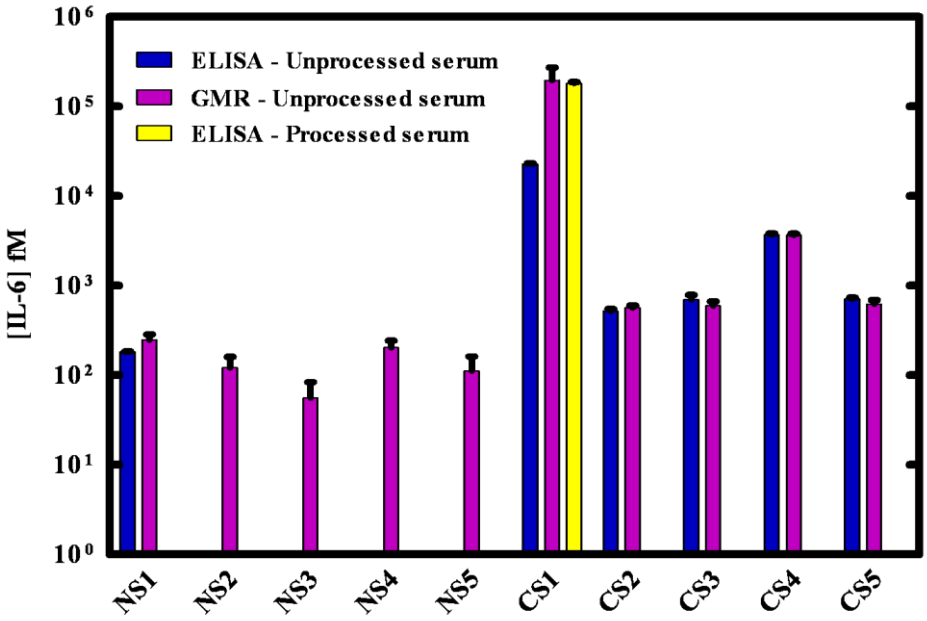

Figure 4.16 Comparison of IL-6 levels in human serum samples determined by ELISA and competition-based GMR biosensor.
Columns: mean; bars: standard deviation ($2 \leq n \leq 8$); NS1-NS5 stands for human serum samples from five healthy individuals; CS1-CS5 stands for human serum samples from five lung cancer patients. Processed serum means that CS1 was diluted 80 times for ELISA quantification while unprocessed serum means the serum sample was evaluated as such. ELISA failed to detect IL-6 in NS2-5.

[IL-6] fM	NS1	NS2	NS3	NS4	NS5	CS1	CS2	CS3	CS4	CS5
ELISA	219	N/A[a]	N/A[a]	N/A[a]	N/A[a]	192140 [b]	552	742	3928	757
GMR	248	122	56	203	112	195981	567	597	3681	627

[a] N/A – Not detectable by ELISA; [b] After 80-fold dilution

Table 4-3 Comparison of IL-6 levels in human serum samples determined by ELISA and GMR biosensor.

4.2.5 Detection Specificity, Time and Reproducibility

We then performed a series of experiments to examine the detecting specificity of our device. One approach evaluating the detecting specificity of IL-6 in sera was to determine whether serum samples depleted of IL-6 would introduce any signals. IL-6 in serum samples from NS1 and CS1 were depleted by an immunoprecipitation approach. The depleted sera were then used in competition with MNL IL-6, following the same procedure. The results (Figure 4.17 (A)) demonstrate that the IL-6 depleted sera, irrespective of their disease state and original IL-6 level, show no competition at all against MNL IL-6, establishing the detecting specificity of our device to IL-6. The detecting specificity against other specific serum proteins of varied abundance was also evaluated. MNL IL-6 was mixed with either 10^6-fold human recombinant interleukin-8 (IL-8), human vascular endothelial growth factor (VEGF), human recombinant fatty acid synthase (FAS), or 10^{10}-fold human albumin from serum (HAS) for competition detection. Again, we detected no signal changes due to the non-specific binding of these

other serum proteins even when they are in high excess compared to IL-6 (Figure 4.17 (B)).

Finally, the detection time and reproducibility of our biosensing system were preliminarily evaluated. The time-course binding of MNL IL-6 to GMR sensor was studied. As show in Figure 4.17 (C), 94% signal was achieved within 1 minute and the binding reached equilibrium for quantification within 5 minutes, demonstrating the feasibility to realize quick detection. The system also demonstrates high reproducibility as shown in Figure 4.17 (D) that different GMR sensors, when used to quantify 4.15 pM IL-6 at four different time points, produces the same results.

4.2.6 Conclusion

In summary, an ultra-sensitive, highly specific and reproducible, and rapid sensing platform with a wide detecting range has been developed. This platform consists of the integration of a near-0 degree GMR sensor with uniform high moment magnetic nanoparticle-based device and a competition-based detecting principle. The feasibility of this system to directly quantify IL-6 in unprocessed human serum samples in five minutes has been demonstrated. Although 4 μL serum was used for this analysis, only 4 nL of the serum is indeed responsible for signal, because we have not achieved sensor area-specific modification that the capture-antibody modified area includes the sensor and its surrounding area. The surrounding area is ~1,000 times the sensor area. Hence,

upon achieving sensor-specific modification, our sensor platform would require only 4 nL of serum or it can quantify IL-6 from serum of much lower IL-6 concentration, which is currently under investigation. The detecting specificity of this system was rigorously established by demonstrating that IL-6 depleted sera introduced no signal at all. Rapid detection (5 min) and reproducibility were also demonstrated for this system. Such a platform paves the practical way for the identification and validation of biomarkers involved in the etiology of various diseases. It may eventually lead to a low-cost and handheld medical device for early detection of chronic diseases.

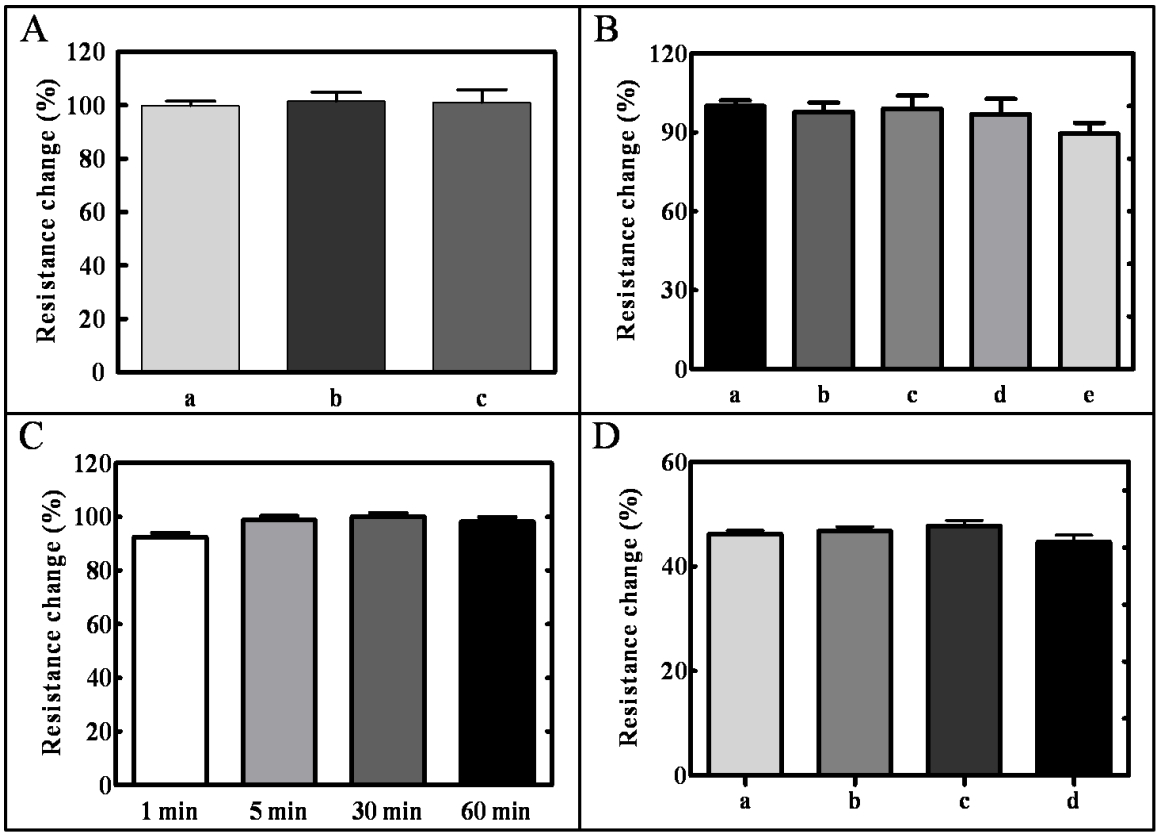

Figure 4.17 Detecting specificity, dynamics, and reproducibility of IL-6
(A) Resistance change in the absence or presence of IL-6 depleted serum with MNL IL-6 molecules. a) Control, no IL-6 depleted serum; b) IL-6 depleted serum from NS1; c) IL-6 depleted serum from CS1 (B) Resistance change in the presence of other proteins with MNL IL-6 molecules (1.25 pM MNL IL-6). a) Control, no competition; b) 1.25x106 pM IL-8; c) 1.25x106 pM VEGF; d) 1.25x106 pM FAS; e) 1.25x1010 pM HAS. (C) Time course binding study. (D) Resistance change due to competition of unlabeled recombinant human IL-6 with MNL IL-6 molecules on the sensor surface, a-d) competition results from four independent experiments that were performed with a one-week interval between two experiments.

4.3 A Three-Layer Competition Based Quantification of Endoglin

4.3.1 Introduction

While patients with high grade prostate cancer make up only 15-20% of those with prostate cancer, they represent more than half of the patients who die from prostate cancer[94]. Early identification of patients with high grade prostate cancer is critical to making inroads into reducing prostate cancer related deaths[95]. While used ubiquitously to screen for prostate cancer, prostate specific antigen (PSA) is neither a sensitive nor a specific biomarker for discriminating between low grade and high grade prostate cancer[96]. Thus, there is an urgent need for additional biomarkers both to improve identification of patients with prostate cancer and to differentiate patients with low-risk and high-risk cancers.

A number of urine-based markers have been investigated for the diagnosis of prostate cancer, including DNA, RNA and protein markers[97-99]. In a single site study among patients undergoing prostate biopsy, levels of urinary endoglin detected by ELISA were shown to distinguish between patients with prostate cancer and those without prostate cancer[100]. The predictive value was found to be superior to the predictive value of PSA[100]. Of particular interest, urinary endoglin was able to distinguish between high volume and low volume diseases. It remains to be determined of its diagnostic potential between low-grad and high-grade prostate cancer. Typically, these urinary markers are

detected either by ELISA or by western blotting. These techniques can have inherent disadvantages including the need to concentrate urine by dialysis to facilitate detection; these obstacles can increase cost, lead to testing errors and involve the need for institutional laboratory testing[97,98]. Therefore alternative technology is needed to feasibly detect endoglin directly from urine.

In principle, a magnetic biosensing system uses GMR sensor to detect stray magnetic field resulting from magnetic labels on the sensor surface. Its application in real biological systems, such as unprocessed human serum and urines, has been very limited, potentially due to the limited biological sensitivity[23,24,27,63,64,66,67,72,82,88,90,91,101-103]. In previous chapter, we have discussed a new GMR sensing platform that has unique features improving its sensitivity – near 0 °ground state for the sensor (3-fold increase in sensitivity) and use of high magnetic moment uniformly sized small (12.8 ± 1.58 nm) cubic shaped FeCo nanoparticles[104] (7-fold increase in sensitivity). Based on the detecting principle, GMR sensor sensitivity strongly depends on the distance (d) between the magnetic nanoparticle and the sensor surface. The magnetic signal decreases as the distance increases[104]. Currently, all other GMR detection of biomolecules employs a three-layer (sandwich) approach that has three biomolecules between GMR sensor and magnetic nanoparticle[23,24,27,63,64,66,67,72,88,90,91,101-103]. A two-layer competition based nanomagnetic assay, which reduces the detection distance by removing the detecting antibody between GMR sensor and magnetic nanoparticle, further improving the

detecting sensitivity (55-fold for IL-6)[104], is discussed in previous chapter too. By integrating these, the sensitivity has been improved by 1000-fold and we have demonstrated that our device can directly detect and quantify low-abundance IL-6 protein directly from 4 μL of unprocessed serum sample[104].

In this section we discuss a competition magnetic bioassay (Figure 4.18), in order to quantify endoglin directly from unprocessed human urine samples using our GMR biosensing technology and to evaluate whether endoglin levels in urine have the potential to predict for the presence of prostate cancer and to distinguish between different grades of prostate cancer. These results have been published as "A Three-Layer Competition-Based Giant Magnetoresistive Assay for Direct Quantification of Endoglin from Human Urine", Srinivasan, B. *et al*. Analytical Chemistry 83, 2996-3002, (2011).

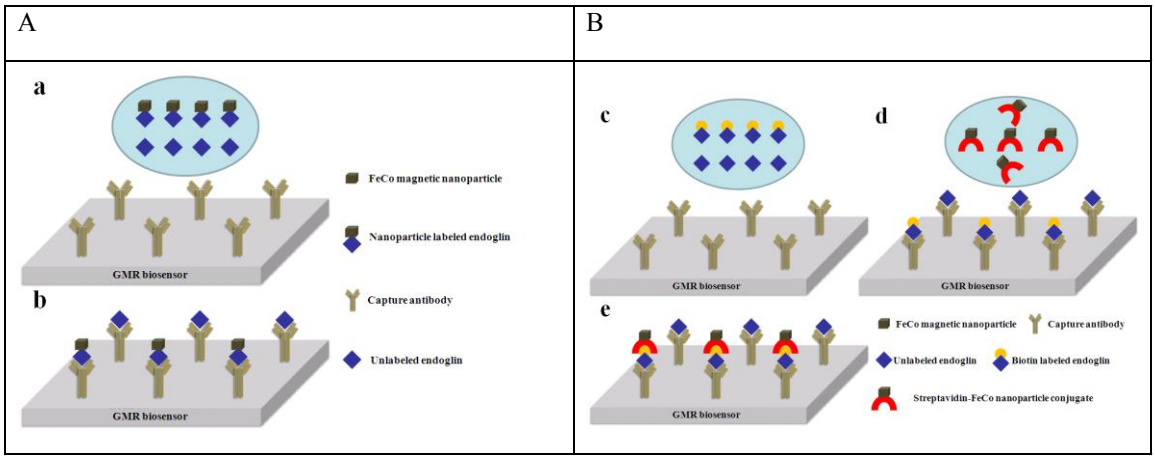

Figure 4.18 Two-layer and three-layer competition detection scheme
A: Two-layer competition detection scheme: the GMR sensors are first functionalized with capture antibodies (a). Nanoparticle labeled endoglin and unlabeled endoglin were then mixed and applied on the sensor surface to compete for capture antibodies (b). B: Three-layer competition detection scheme: the GMR sensors are first functionalized with capture antibodies. Biotin labeled endoglin and unlabeled endoglin were then mixed and applied on the sensor surface to compete for capture antibodies (c). Subsequently, streptavidin-FeCo nanoparticle conjugates were applied for binding (d and e).

4.3.2 Experimental methods

GMR sensor and nanoparticle fabrication and magnetoresistance measurement: Fabrication of GMR sensor and high magnetic moment cubic FeCo nanoparticles and magnetoresistance measurements were carried out by following the same procedures as described in earlier report[72] and Chapter 3.

Sensor surface modification: GMR sensor surface was sequentially modified with (3-aminopropyl)triethoxysilane (APTES) followed by capture antibody attachment through 1-[3-(dimethylamino)propyl]-3-ethylcarbodiimide (EDC) coupling reaction. After each step, the surface was thoroughly washed with water to remove unbound ligands, which were collected for quantification. For each step of modification, bound ligands were quantified using the following equation: amount of bound ligand on the surface = amount of total ligand added – amount of ligand recovered.

Cubic FeCo nanoparticle surface modification: i. APTES modification: A solution of APTES (100 μg in 0.5mL ethanol) and ammonium hydroxide (5 μl, 29%) was added to cubic FeCo nanoparticles (100 μg) and sonicated for 4h. ii. Human recombinant endoglin modification: To a dispersion of FeCo nanoparticles (0.3mL, PBS buffer, pH 7.4; 30 μg of FeCo nanoparticles), dylight 488 labeled endoglin (6.2 μL, 0.5mg/mL in PBS buffer, pH 7.4) and EDC (10 μL, 5mg/mL in PBS buffer, pH 7.4) was added and shaken overnight at 4 ℃ under light-protected conditions. Endoglin to nanoparticle ratio was found to be 1.36:1 upon quantification. iii. Streptavidin-AF488 modification: FeCo nanoparticles are modified with streptavidin-AF488 in a ratio of 1:1.3 according to our previously published procedure[72].

Two-layer competition assay for human endoglin in urine samples: A 4 μL mixture of urine sample (4 nL per sensor area) and high magnetic moment FeCo nanoparticle labeled endoglin (1.66 $x10^{-20}$ mol per sensor area, 4.15 pM,

nanoparticle/endoglin = 1.357) was applied to compete for capture antibody (1.66 $x10^{-20}$ mol per sensor area) on the GMR sensor surface for 10 min at 4 ℃. Resistance change of the GMR sensor was measured.

Three-layer competition assay for human endoglin in urine samples: A 20 μL mixture of urine sample (20 nL per sensor area) and endoglin-$biotin_{20}$ (1.66 $x10^{-20}$ mol per sensor area, 0.83 pM) was applied to compete for capture antibody (1.66 $x10^{-20}$ mol per sensor area) on the GMR sensor surface for 30 min at 4 ℃. Then streptavidin-FeCo nanoparticle conjugate (41.5 pM, $1.66x10^{-19}$ mole streptavidin per sensor area, streptavidin/nanoparticle 1.3:1) was applied for binding for 10 min at 4 ℃ followed by washing with water to remove unbound streptavidin-FeCo nanoparticle conjugates. Resistance change of the GMR sensor was measured.

Three-layer competition assay dose response curve: Briefly a spiked mixture of endoglin-$biotin_{20}$ ($1.66x10^{-20}$ mol per sensor area, 0.83 pM) and varied concentrations of unlabeled endoglin in 20 μL endoglin depleted urine cocktail was applied on the sensor surface to compete for capture antibody ($1.66x10^{-20}$ mol per sensor area) on the sensor for 30 min at 4 ℃. Then streptavidin-FeCo nanoparticle conjugate (41.5 pM, $1.66x10^{-19}$ mole streptavidin per sensor area, streptavidin/nanoparticle 1.3:1) was applied for binding for 10 min at 4 ℃ followed by washing with water to remove unbound streptavidin-FeCo nanoparticle conjugates. Resistance change of the GMR sensor was measured.

Total urinary protein estimation: Total urinary proteins in the urine samples were determined by micro pyrogallol red method using a total protein kit, (catalog number TP0400) purchased from Sigma Aldrich following vendor's protocol.

Creatinine quantification in urines: Quantitative determination of creatinine in the urine samples were determined by using creatinine assay kit (catalog number KGE005) purchased from R&D Systems, Inc., Minneapolis, USA following vendor's protocol.

4.3.3 Results and discussion

Two-layer competition assay for urinary endoglin detection: Two-layer competition assay (Figure 4.18 (A)) was used first to detect endoglin from the urine (4 µL) where urinary endoglin competes with high magnetic moment FeCo nanoparticle labeled endoglin ($1.66x10^{-20}$ mol per sensor area, 4.15 pM, nanoparticle/endoglin = 1.357) for capture antibody ($1.66x10^{-20}$ mol per sensor area) on the GMR sensor surface. Nanoparticle labeled endoglin in PBS buffer, pH 7.4 (4 µL, $1.66x10^{-20}$ mol per sensor area, 4.15pM) binding to capture antibody on the sensor surface served as one control. The other control (for non-specific competition) uses endoglin depleted urine U1 to compete with high magnetic moment FeCo nanoparticle labeled endoglin ($1.66x10^{-20}$ mol per sensor area,4.15pM) for capture antibody ($1.66\ x10^{-20}$ mol per sensor area) on the GMR sensor surface. High grade prostate cancer patient urine U1 (4 µL) under this condition resulted in no statistical significant resistance change as a sensing signal compared to controls. This observation in part may be result of urinary endoglin cannot

effectively compete and easily displace nanoparticle labeled endoglin (if nanoparticle labels the endoglin at the proximity of its binding site) from the capture antibody binding site and/or very low competition from urinary endoglin in that sample due to low abundance. Hence the urine sample U1 was lyophilized and reconstituted in double distilled water to obtain 6.67 fold concentrated sample for testing under two-layer competition assay. Although the concentrated urine sample U1 showed statistically significant resistance change, the magnitude of resistance change is small (Figure 4.19 (A)).

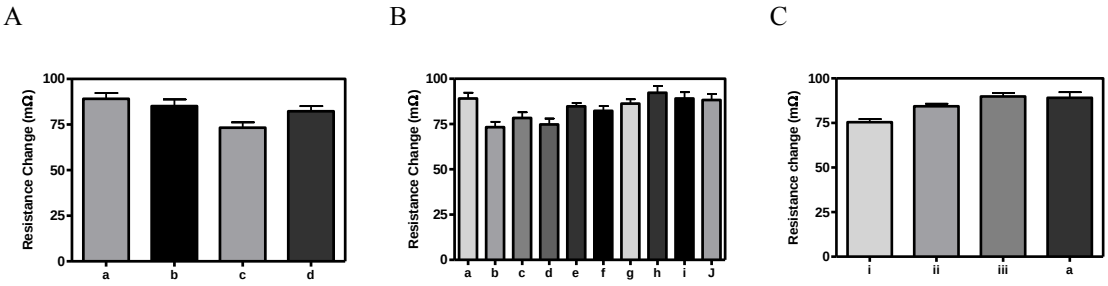

Figure 4.19 Resistance changes from urine samples
A: Resistance change due to competition of urine sample with magnetic nanoparticle labeled endoglin (4.15pM)
a) control, no competing urine sample; b) urine U1 from a high grade prostate cancer patient; c) 6.66-fold concentrated urine U1 from a high grade prostate cancer patient; d) endoglin depleted urine U1 from a high grade prostate cancer patient.
B: Resistance change due to competition of 6.66 fold concentrated urine samples with magnetic nanoparticle labeled endoglin (4.15pM) a) control, no competing urine; b) U1; c) U2; d) U3; e) U6; f) U7; g) U8; h) U11; i) U12; j) U13.
C: Average resistance change caused by i) three high grade prostate cancer urines (U1-U3); ii) three low grade prostate cancer urines (U6-U8); iii) three no prostate cancer urines (U11-U13); a) control, no competing urine.

Using this method, three samples from each group (urines U1-U3 from patients who are biopsy positive for high grade prostate cancer; U6-U8 low grade prostate cancer; and U11-U13 from individuals who are biopsy negative for cancer) were tested (Figure 4.19 (B)). Upon signal averaging, high grade urine samples group showed statistical significant resistance change whereas low grade and no cancer urine samples groups did not showed any statistical significant resistance change compared to control. Though the two-layer competition assay results are encouraging, urine samples need to be concentrated; and low grade prostate and no cancer patients cannot be differentiated by endoglin levels in the urines (Figure 4.19 (C)).

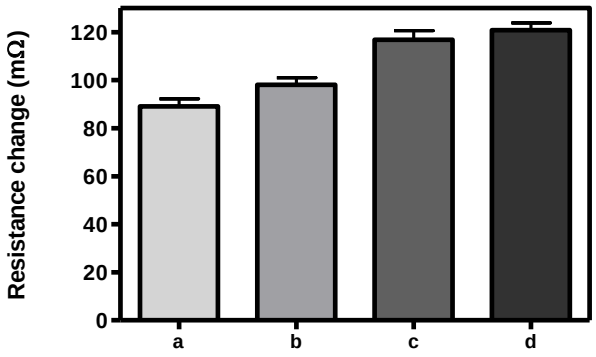

Figure 4.20 Resistance changes upon binding to capture antibody modified ($1.66x10^{-20}$ mol capture antibody per sensor area) sensor surface
a) nanoparticles harvested form one nanoparticle per endoglin reaction (4.15pM endoglin); b) nanoparticles harvested from two nanoparticle per endoglin reaction (4.15pM endoglin); c) endoglin-$biotin_{20}$ (4.15pM) followed by nanoparticles harvested

from one nanoparticle per streptavidin reaction (41.5 pM streptavidin) binding; d) endoglin-biotin$_{20}$ (4.15pM) followed by nanoparticles harvested from two nanoparticle per streptavidin reaction (41.5 pM streptavidin) binding.

Two nanoparticles labeling of endoglin was sought to improve the sensitivity of this detection scheme as the sensing signal comes from the nanoparticle labeling. To achieve one nanoparticle labeling per endoglin, we used one equivalent of nanoparticles and 1.5 equivalents of endoglin under coupling reaction conditions. Hence for two nanoparticles labeling of the endoglin, we used one equivalent of nanoparticles and three equivalents of endoglin for reaction. When we used harvested particles from the endoglin two nanoparticles labeling reaction on our GMR sensor, signal improved minimally compared to one nanoparticle labeled endoglin binding (Figure 4.20) indicating that two nanoparticle cannot be attached per endoglin potentially due to comparable sizes of endoglin and nanoparticle and the other one equivalents of the particle remain unmodified which gets washed off after binding event.

Three-layer competition assay for urinary endoglin detection: The other way to accomplish more than one nanoparticle per endoglin to gain assay sensitivity is to modify endoglin with several biotins; and biotins on the endoglin can be recognized by streptavidin-nanoparticle conjugates (Figure 4.18 (B)). Endoglin molecules were labeled with biotin using biotin N-hydroxysuccinimidyl ester coupling chemistry to have biotin to endoglin ratio 4, 8, 12, 16 and 20. To identify the right biotin loading per endoglin to bind more streptavidin, optimization experiments were done on silica wafer. Capture

antibodies were covalently coupled to silica wafers modified with 3-aminopropyltriethoxysilane (APTES). Endoglin labeled with different copies of biotin (4, 8, 12, 16 and 20 biotin copies per endoglin) were applied to each capture antibody modified wafer surfaces. Fixed amount of streptavidin-AF488 was applied to all endoglin-biotin bound surfaces and unbound streptavidin-488 from each spots was quantified. From the results, one endoglin-biotin$_{20}$ (one endoglin molecule is labeled with 20 copies of biotin molecules) was found to capture 3.2 copies of streptavidin-AF488. If streptavidin-nanoparticle conjugate (streptavidin/nanoparticle, 1.3:1) binds similarly as streptavidin-AF488 to endoglin-biotin$_{20}$, then this will result in three nanoparticles per endoglin on average. This three layer assay not only will result in more nanoparticle labels per endoglin but also will increase the distance between the nanoparticle label and sensing surface. If advantageous more nanoparticle labels per endoglin over rides disadvantageous distance increase between nanoparticle label and the sensing surface, sensing signal from three layer assay will be more compared to two-layer assay on the GMR platform.

The three-layer competition assay was used to detect endoglin from the 6.67 fold concentrated high grade prostate urine sample (4μL, WO6 52) where urinary endoglin competes with endoglin-biotin$_{20}$ (1.66 x10^{-20} mol per sensor area, 4.15pM, biotin/endoglin = 20) for capture antibody (1.66 x10^{-20} mol per sensor area) on the GMR sensor surface followed by streptavidin-FeCo nanoparticle conjugate (41.5 pM, 1.66x10^{-}

^{19} mole streptavidin per sensor area, streptavidin/nanoparticle 1.3:1) binding and washing with water to remove unbound streptavidin-FeCo nanoparticle conjugates. The same experiment without competing urine sample for capture antibody on the sensor surface served as one control. The same experiment with endoglin instead of endoglin-biotin$_{20}$ and without competing urine sample for capture antibody on the sensor surface served as negative control. Three-layer assay produced 25% more signal (117 mΩ) compared to two-layer assay (94 mΩ). Streptavidin nanoparticles also don't non-specifically bind to endoglin (Figure 4.21). Urinary endoglin also competed efficiently with endoglin-biotin$_{20}$ than with nanoparticle labeled endoglin. This is reasonable since nanoparticle is heavy and if it gets modified at the proximity of endoglin binding site to capture antibody so that once nanoparticle labeled endoglin binds to capture antibody, it is difficult to be displaced by urinary endoglin. Since biotin is small in size compared to nanoparticle, urinary endoglin can effectively compete and easily displace endoglin-biotin$_{20}$ from the capture antibody binding site. Though three-layer competition assay performs better than two-layer competition assay, urine samples need to be concentrated for testing unless sensitivity is further improved.

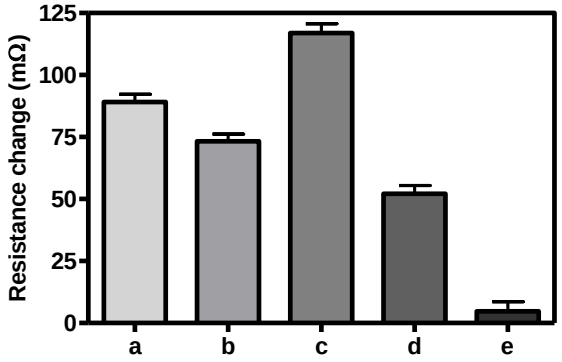

Figure 4.21 Resistance changes upon binding to capture antibody modified ($1.66x10^{-20}$ mol capture antibody per sensor area) sensor surface
a) magnetic nanoparticle labeled endoglin (4.15pM); c) endoglin-$biotin_{20}$ (4.15pM) followed by streptavidin-FeCo nanoparticle conjugate (41.5 pM, $1.66x10^{-19}$ mole streptavidin per sensor area, streptavidin/nanoparticle 1.3:1) binding; e) endoglin (4.15pM) followed by streptavidin-FeCo nanoparticle conjugate (41.5 pM) binding.
Resistance change due to competition of 6.66 fold concentrated urine U1 sample
b) with magnetic nanoparticle labeled endoglin (4.15pM); d) with endoglin-$biotin_{20}$ (4.15pM) followed by streptavidin-FeCo nanoparticle conjugate (41.5 pM) binding e).

To increase more nanoparticles per endoglin in the three-layer competition assay, two nanoparticle conjugations per streptavidin was sought as a solution. Since streptavidin is relatively little bigger molecule compared to endoglin, it will be worth to try two nanoparticle conjugation per streptavidin despite failure with endoglin. When we used harvested particles from the streptavidin two nanoparticles labeling reaction on our GMR sensor, signal improved minimally compared to one nanoparticle labeled streptavidin binding indicating that two nanoparticles cannot be attached per streptavidin due to comparable sizes of streptavidin and nanoparticle (Figure 4.20). The undesired

processing of urine samples was avoided by using 20 µL urine volume (20 nL per sensor area) as it provides five-fold more urinary endoglin than 4 µL for three-layer competition assay leading to significant drop in resistance change (big sensing signal) upon competition. Though the more sample volume covers extra area including capture antibody modified area, as and when endoglin reaches the proximity of capture antibody due to Brownian motion, binding can happen. To test this hypothesis for two-layer assay, 4 µL nanoparticle labeled endoglin in PBS buffer, pH 7.4 (4nL and 1.66 $x10^{-20}$ mol per sensor area, 4.15pM) and 20 µL nanoparticle labeled endoglin in PBS buffer, pH 7.4 (20nL and 1.66 $x10^{-20}$ mol per sensor area, 0.83pM) binding to capture antibody (1.66 $x10^{-20}$ mol per sensor area) on the sensor surface was carried out. Sensing signal obtained by the use of 20 µL sample volume corresponds to 78% of sensing signal obtained by the use of 4 µL sample volume and this can happen mainly due to Brownian motion (Figure 4.22).

To test this hypothesis for three-layer assay, 4 µL endoglin-$biotin_{20}$ (4 nL and 1.66 $x10^{-20}$ mol per sensor area, 4.15 pM) and 20 µL endoglin-$biotin_{20}$ (20 nL and 1.66 $x10^{-20}$ mol per sensor area, 0.83pM) binding to capture antibody (1.66 $x10^{-20}$ mol per sensor area) on the GMR sensor surface followed by 4 µL streptavidin-FeCo nanoparticle conjugate (4 nL and $1.66x10^{-19}$ mole streptavidin per sensor area, 41.5 pM) binding were carried out. Sensing signal obtained by the use of 20 µL sample volume corresponds to 75% of sensing signal obtained by the use of 4 µL sample volume and supports involvement of

Brownian motion (Figure 4.22). Though signal drops by ~25% by the use of 20 μL sample volume, it provide five-fold more urinary endoglin than 4 μL do for three-layer competition assay which will leads to significant drop in resistance change upon competition.

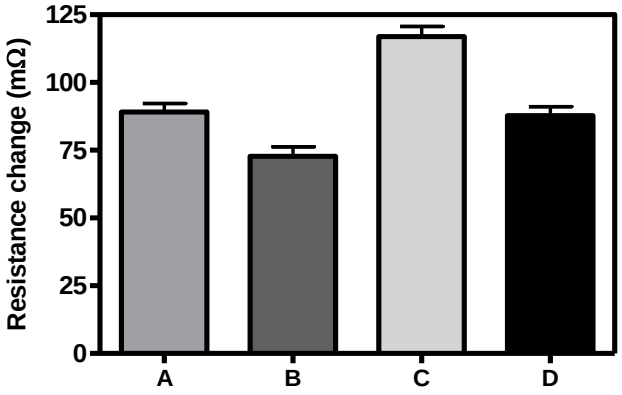

Figure 4.22 Resistance changes upon binding to capture antibody modified ($1.66x10^{-20}$ mol capture antibody per sensor area) sensor surface
A) 4 μL magnetic nanoparticle labeled endoglin in PBS buffer (4 nL and $1.66x10^{-20}$ mol per sensor area, 4.15pM); B) 20 μL magnetic nanoparticle labeled endoglin in PBS buffer (20 nL and $1.66x10^{-20}$ mol per sensor area, 0.83 pM); C) 4 μL endoglin-$biotin_{20}$ in PBS buffer (4 nL and $1.66x10^{-20}$ mol per sensor area, 4.15pM) followed by 4 μL streptavidin-FeCo nanoparticle conjugate in PBS buffer (4 nL and $1.66x10^{-19}$ mole streptavidin per sensor area, 41.5 pM) binding; D) 20 μL endoglin-$biotin_{20}$ in PBS buffer (20 nL and $1.66x10^{-20}$ mol per sensor area, 0.83 pM) followed by 4 μL streptavidin-FeCo nanoparticle conjugate in PBS buffer (4 nL and $1.66x10^{-19}$ mole streptavidin per sensor area, 41.5 pM) binding.

Based on this outcome, urine samples (20 μL; urines from patients who are biopsy positive for high grade prostate cancer U1-U5; low grade prostate cancer U6-U10 and

from individuals who are biopsy negative for cancer U11-U15) were tested as such without any processing under three-layer competition assay wherein 20 μL urine samples (20nL per sensor area) competes with endoglin-biotin$_{20}$ (0.83 pM, 1.66x10^{-20} mol per sensor area) for capture antibody on the sensor surface. All urine samples showed statistical significant resistance change as a sensing signal compared to control (Figure 4.23).

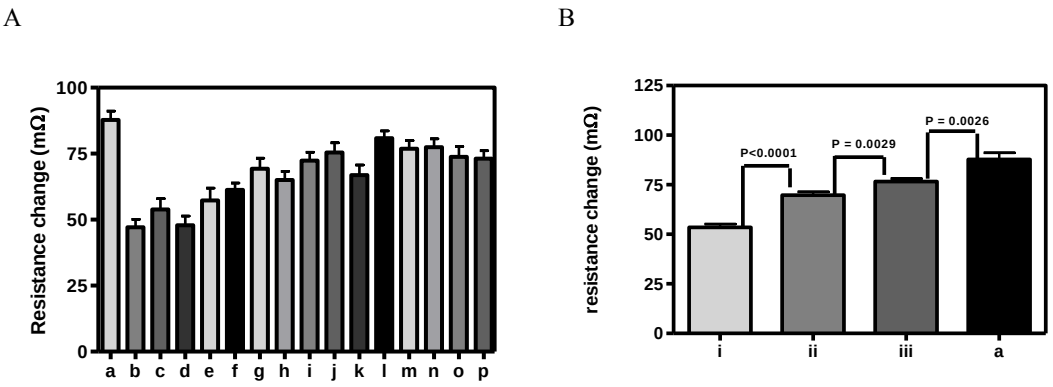

Figure 4.23 Resistance change due to competition of 20 μL urine samples and Average resistance change from different grades of prostate cancer urines
A: Resistance change due to competition of 20 μL urine samples (20 nL per sensor area) with endoglin-biotin$_{20}$ (0.83 pM, 1.66x10^{-20} mole per sensor area) followed by streptavidin-FeCo nanoparticle conjugate (41.5 pM, 1.66x10^{-19} mole streptavidin per sensor area, streptavidin/nanoparticle 1.3:1) binding
a) control, no competing urine; b) U1; c) U2; d) U3; e) U4; f) U5; g) U6; h) U7; i) U8; j) U9; k) U10; l) U11; m) U12; n) U13; o) U14; p) U15.
Columns, mean; bards, standard deviation; $6 \leq n \leq 8$.
B: Average resistance change caused by

i) five high grade prostate cancer urines (U1-U5); ii) five low grade prostate cancer urines (U6-U10); iii) five no prostate cancer urines (U10-U15); a) control.

Encouraged by the results, as a next step to determine endoglin levels in the tested urine samples, dose response curve was established for three-layer competition assay. To have real biological environment for the dose response curve experiment, equal amounts of all urine samples tested are mixed to give a urine cocktail; and endoglins in the cocktail were depleted on a capture antibody coated silica wafer surface. Briefly a spiked mixture of endoglin-biotin$_{20}$ (0.83 pM) and varied concentrations of pure unlabeled human recombinant endoglin in 20 µL endoglin depleted urine cocktail was applied on the sensor surface to compete for capture antibody on the sensor followed by streptavidin-FeCo nanoparticle conjugate (41.5 pM) binding. Figure 4.24 shows the dose-response curve of the three-layer competition assay which provides a wide detection range of endoglin from 27.6 fM to 83 pM with a statistically significant lower detection limit of 83fM. Results from each single competing dose were compared with that of their immediate higher and lower competing doses as well as with the sensor background to arrive statistical meaning. Our results show that the sensing signals obtained from buffer and endoglin depleted urine environment do not statistically differ from each other indicating that proteins other than endoglin in the urine do not non-specifically compete with endoglin-nanoparticles for capture antibody. This clearly reveals the detection specificity of our GMR device.

Urine test results from the three-layer competition assay were fitted into the dose-response curve to deduce endoglin levels in the urine samples (Figure 4.25 (A)). Results show that endoglin concentration levels are significantly different between high grade (208 ±123 fM), low grade prostate cancer (79.1 ±57.4 fM) patients and no prostate cancer (45.8 ±28.0 fM) patient's urine samples (Figure 4.25 (B)).

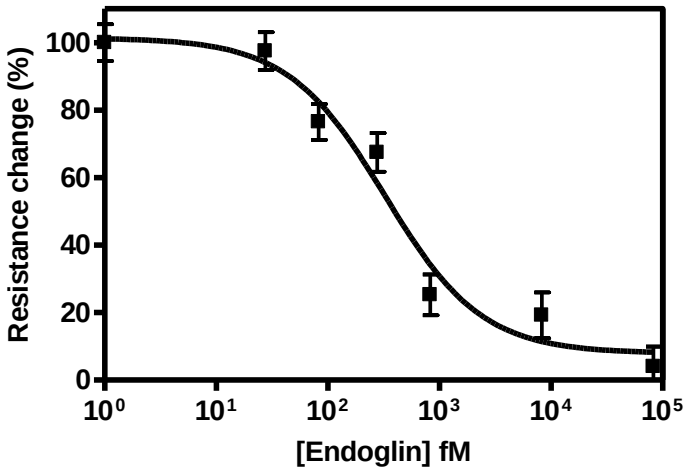

Figure 4.24 Three-layer competition dose response curve
Percentage resistance change due to competition of spiked mixture of endoglin-biotin$_{20}$ (1.66×10^{-20} mol per sensor area, 0.83 pM) and varied concentrations of unlabeled human recombinant endoglin in 20 µL endoglin depleted urine cocktail for capture antibody (1.66×10^{-20} mol per sensor area) on the sensor followed by streptavidin-FeCo nanoparticle conjugate (41.5 pM, 1.66×10^{-19} mole streptavidin per sensor area, streptavidin/nanoparticle 1.3:1) binding.

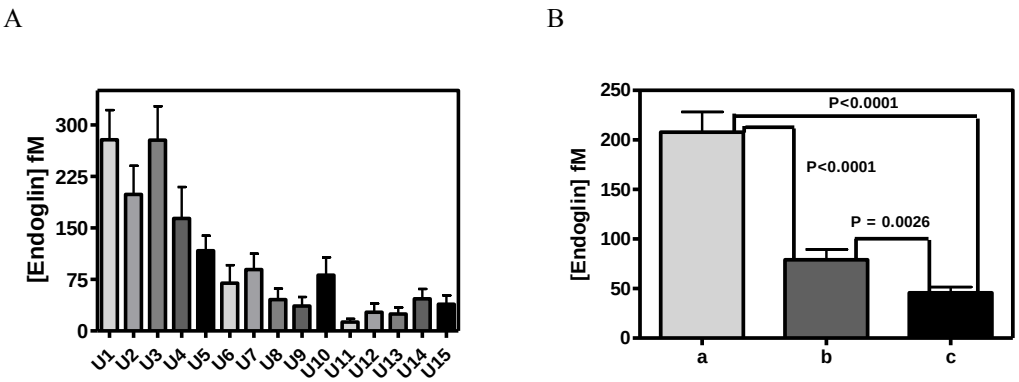

Figure 4.25 A: Endoglin levels in all the urine samples tested by three-layer competition assay; B: Average endoglin levels in the urine groups a) high grade prostate cancer (U1-U5); b) low grade prostate cancer (U6-U10); c) no prostate cancer (U11-U15).

Total urinary proteins in the urine samples were determined by micro pyrogallol red method using a total protein kit from Sigma Aldrich. One high and one low reading samples for total urinary protein from each high grade, low grade and no cancer group were desalted using Zeba^{TM} desalting column (7K molecular weight cut-off); and total urinary proteins were again quantified to determine influence of urinary salts on pyrogallol red assay for total urinary proteins (Table 4-4). The total urinary protein determinations of urines before and after desalting do not differ statistically indicating assay is not sensitive to urinary salt contents. Endoglin levels were normalized to total urinary protein (TP) and remained significantly elevated in the cancer cases (Figure 4.26). Quantitative determination of Creatinine in the urines samples were carried out

(Table 4-5) and endoglin levels were normalized to creatinine levels; and also remained significantly elevated in the cancer cases (Figure 4.26).

Urine samples	Total urinary proteins, μg/mL (before desalting) (mean ±SD; n=3)	Total urinary proteins, μg/mL (after desalting) (mean ±SD; n=3)
High grade prostate cancer		
U1	257.36 ±0.49	261.33 ±0.49
U2	498.87 ±0.74	
U3	35.42 ±0.74	35.14 ±0.85
U4	164.51 ±0.74	
U5	39.79 ±0.28	
Low grade prostate cancer		
U6	235.85 ±0.74	
U7	60.82 ±0.49	61.76 ±0.94
U8	71.34 ±0.28	
U9	325.62 ±1.01	
U10	417.50 ±2.12	423.94 ±2.15
No prostate cancer		
U11	378.36 ±0.28	384.20 ±0.29
U12	279.68 ±1.28	
U13	132.64 ±0.97	134.69 ±0.99
U14	310.9 ±1.22	
U15	140.41 ±0.49	

Table 4-4 Total urinary proteins before and after desalting human urine samples

A B

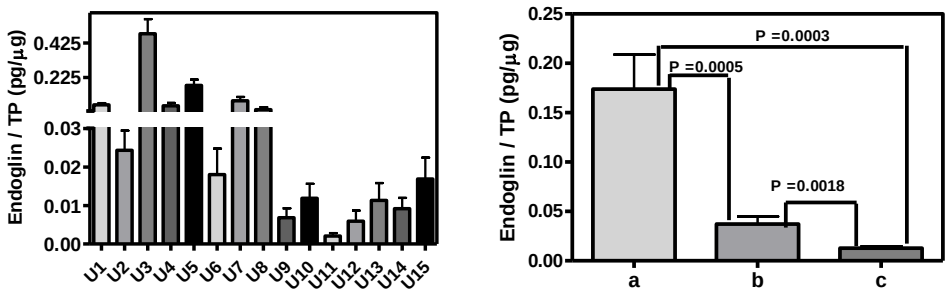

Figure 4.26 Endoglin to total urinary protein ratio and average endoglin to total urinary proteins (pg/µg) in tested urine samples
A: Endoglin to total urinary protein ratio (pg/µg) in tested urine samples;
B: Average endoglin to total urinary proteins (pg/µg) in the urine groups
a) high grade prostate cancer (U1-U5);
b) low grade prostate cancer (U6-U10);
c) no prostate cancer (U11-U15).

Urine samples	Creatinine levels, mg/mL (mean ±SD; n=2)
High grade prostate cancer	
U1	3.74 ±0.03
U2	13.00 ±0.03
U3	2.04 ±0.01
U4	9.15 ±0.02
U5	3.05 ±0.04
Low grade prostate cancer	
U6	6.40 ±0.09
U7	8.07 ±0.22
U8	2.31 ±0.01
U9	4.93 ±0.06

U10	1.78 ±0.01
No prostate cancer	
U11	2.39 ±0.01
U12	3.66 ±0.03
U13	4.21 ±0.09
U14	8.45 ±0.37
U15	3.66 ±0.02

Table 4-5 Creatinine levels in human urine samples

A B

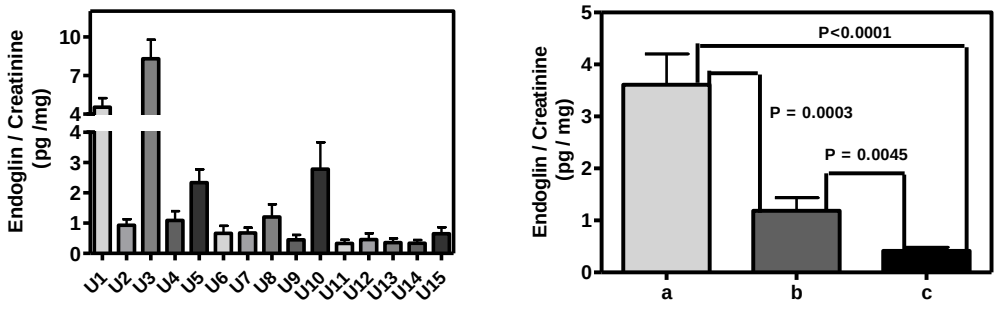

Figure 4.27 Endoglin to creatinine ratio and average endoglin to creatinine (pg/mg) in tested urine samples
A: Endoglin to creatinine ratio (pg/mg) in tested urine samples;
B: Average endoglin to creatinine (pg/mg) in the urine groups
a) high grade prostate cancer (U1-U5);
b) low grade prostate cancer (U6-U10);
c) no prostate cancer (U11-U15).

4.3.4 Conclusion

In conclusion, we have developed a novel three-layer competition-based assay on GMR biosensing system to detect urinary endoglin with high specificity and sensitivity using

unprocessed human urine samples. Our platform can detect as few as 1000 copies of the endoglin at concentrations as low as 83 fM. When functionalized to detect endoglin in the urine, our GMR biosensing system was able to successfully discriminate between patients with high grade cancer, and low grade cancer, and those with no cancer.

Chapter 5 External-field Free Magnetic Biosensing

5.1 Introduction

In this chapter, a new magnetic nanoparticle (MNP) detection scheme, without the presence of any external magnetic field, has been proposed, theoretically and experimentally studied. The goal is to reduce power consumption, which is critical for point-of-care applications. The proposed sensor structure uses a patterned groove structure in the biosensor so that the stray magnetic fields from the magnetic device will magnetize the MNPs. An example is given based on GMR sensing device with a spin valve structure. For this structure, the stray field from the free and pinned layer is used to magnetize the MNPs, located inside the groove and near to the free layer. Micromagnetic simulations are performed to calculate the signal level of this detection scheme. A maximum SNR of 40 dB from one iron oxide magnetic nanoparticle with 8 nm radius is obtained from the simulation. As proof of concept, GMR sensor with groove structure of 200 nm × 200 nm was fabricated using electron beam lithography. Using this sensor, the detection SNR of 30 μL 30 nm magnetic nanoparticles is around 9.3 dB. This sensor structure is not limited to GMR device and is applicable for other spintronic and magnetic sensing devices such as MTJ, Hall sensor with sandwiched structure and giant magneto impendence (GMI). These results have been published as “External-field-free magnetic

biosensor", Li, Y., Wang, Y., Klein, T. & Wang, J.-P. Appl. Phys. Lett. 104, 122401, (2014).

5.2 Background and Motivation

Bioassays that detect and quantify biomolecules at ultra-low quantity with point-of-care settings are of great need in many fields including basic medical science, disease control and diagnostics, drug discovery and environment monitoring, etc. Since the first proposal in 1998[63], magnetic biosensing scheme, which combines the magnetic biosensor and the magnetic nanoparticle (MNP), has been intensively studied[23,24,26-28,63,64,66-68,72,82,87-90,104,105]. These systems are based on the specific bond between the targeted biomolecule and the biologically-functionalized surface of an individual magnetic field sensor or a sensor-array. Functionalized MNPs are then specifically bound to these targeted biomolecules. Studied magnetic biosensors include GMR sensor[23,24,63,68,72,88,90,104,105], MTJ sensor[66], Hall biosensor[106,107] or GMI biosensor[108]. The dipole field from the specifically bond magnetized MNPs will change the average magnetic field on the sensing layer of the magnetic biosensor. This causes the change of the magnetization configuration and consequently the transfer curve of the magnetic biosensor. This change can then be quantitatively correlated with the number of the MNPs. Previous work has focused primarily on sensing modes that require a magnetic field generator, which is detrimental to the promised portability feature for magnetic

biosensors and also increases the power consumption of the whole system. Magnetic field from the bias current passed through the biosensor was proposed for magnetizing the MNPs[109]. This can eliminate the usage of the electromagnet. However, the issue for large power consumption still exists. A large current on sensing chip, such as tens of milliamperes, is required to produce a large enough magnetic field for magnetizing the MNPs. Such large current will not only cause Joule heating but also may result in a failure (electrical or mechanical) of the passivation layer between the sensor and the biological sample. To overcome these challenges, we propose the usage of stray field from the magnetic biosensor itself to magnetize the MNPs thus totally eliminate the usage of any external magnetic field generator (electromagnets or current lines). This scheme just requires a specific patterned structure, e.g. the groove, in the magnetic biosensor, which can be fabricated using a well-established ion milling or any other proper lithograph processes.

5.3 Analytical model

5.3.1 Conventional detection scheme

In a currently available (defined as conventional in this chapter) magnetic biosensing scheme using a spin valve structure as shown in Figure 5.1, the MNP is biologically bond to the surface of magnetic biosensor. In this configuration, an external magnetic field is

needed so that the superparamagnetic MNP is magnetized. The magnetized MNP generates a dipole magnetic field, which exerts on the free layer of the spin valve. Before the MNP is bond to the sensor surface, the effective field $\boldsymbol{H}_{eff}$ on the free layer is:

$$\boldsymbol{H}_{eff}=\boldsymbol{H}_{ext}+\boldsymbol{H}_{stray\text{-}pinned}$$

where $\boldsymbol{H}_{ext}$ is the external applied magnetic field and $\boldsymbol{H}_{stray\text{-}pinned}$ is the stray field from pinned layer. After bonding to the surface of the sensor, the MNP is magnetized by the external applied field, as well as the stray field from free and pinned layers. Both the stray fields from the free layer and pinned layer are very small and can be ignored for the conventional magnetic biosensing scheme. The magnetic charges from the free layer (two ends of the long axis of the sensor) are far from most of bond MNPs because of the large dimension of the sensor along the long axis. The magnetic charges from the fixed layer (two ends of the short axis of the sensor) are far from most of bond MNPs because of the distance from the pinned layer to sensor top surface. Due to the superparamagnetic property of the MNP, at external field $\boldsymbol{H}_{ext}$, its magnetization can be expressed as:

$$\boldsymbol{M} = \boldsymbol{M}_s \times L\left(\frac{\boldsymbol{m}_0\mu_0(\boldsymbol{H}_{ext} + \boldsymbol{H}_{stray\text{-}film})}{k_B T}\right)$$

where $\boldsymbol{M}_s$ is the saturation magnetization, $\boldsymbol{m}_0$ is the magnetic moment of a single particle, μ_0 is the magnetic permeability of vacuum, $\boldsymbol{H}_{ext}$ is the applied magnetic field, $\boldsymbol{H}_{stray\text{-}film}$ is the stray field from free and pinned layer, k_B is the Boltzmann constant, T is

the absolute temperature, and L is the Langevin function. Thus, the dipole field from the MNP on the free layer can be written as:

$$\boldsymbol{H}_{dipole}=\frac{3(\boldsymbol{m}\cdot\boldsymbol{r})\boldsymbol{r}}{r^5}-\frac{\boldsymbol{m}}{r^3}$$

where $\boldsymbol{m}$ is the magnetic moment of the MNP, $\boldsymbol{r}$ is space vector from the center of the MNP to the free layer. Therefore, the effective field on the free layer is then expressed as:

$$\boldsymbol{H}_{eff}=\boldsymbol{H}_{ext}+\boldsymbol{H}_{stray\text{-}pinned}+\boldsymbol{H}_{dipole}$$

The change of $\boldsymbol{H}_{eff}$ on the free layer before and after the MNP bonding will change the orientation of the free layer magnetization $\boldsymbol{M}_{free}$, which leads to an electrical signal change of the magnetic biosensor.

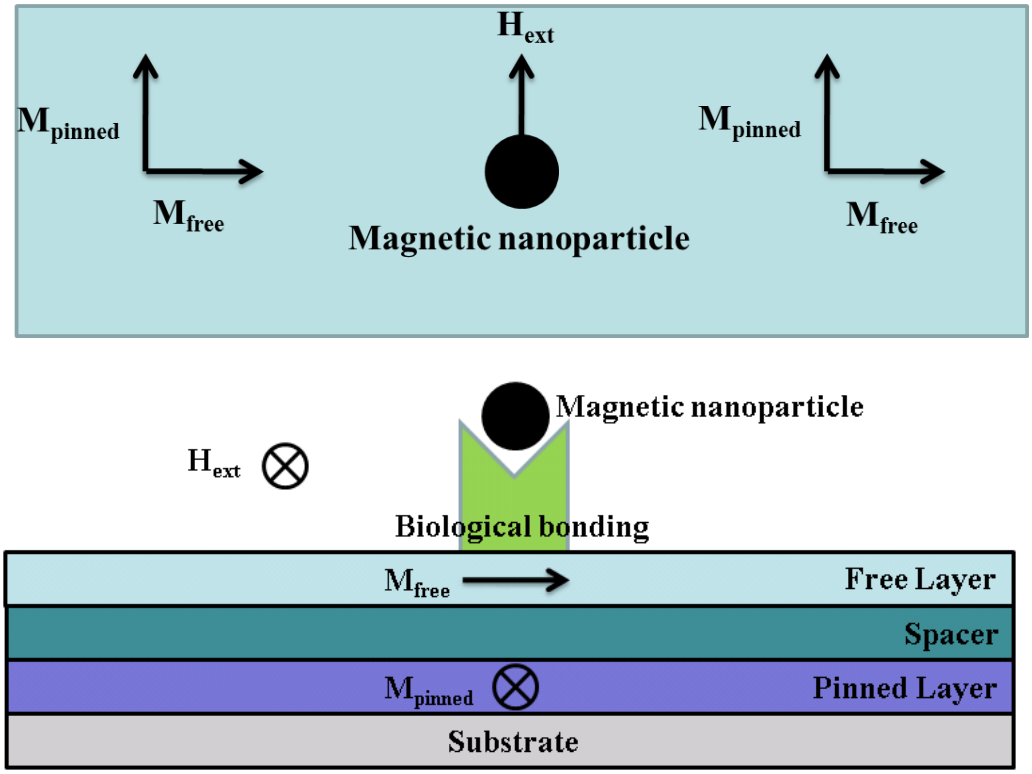

Figure 5.1 conventional magnetic biosensing scheme
a) Top view of a conventional magnetic biosensing scheme;
b) Cross-section view of a conventional magnetic biosensing scheme.
M_{free} and M_{pinned} are the magnetization of free and pinned layers of the spin valve structure, respectively. H_{ext} is the external applied magnetic field.

5.3.2 External-field-free detection scheme

Figure 5.2 describes our proposed external-field-free detection scheme. In this detection scheme, a groove structure is purposely created on the magnetic sensor, so that the MNPs can be bond into the groove where the magnetic charges from both free layer and pinned layer are close to the MNP thus the stray fields from the magnetic films (free and pinned layer) $\boldsymbol{H}_{stray\text{-}film}$ are strong. In this configuration, before the MNP bonding, the effective field on the free layer is only the stray field from the pinned layer, without the presence of the external applied field:

$$\boldsymbol{H}_{eff} = \boldsymbol{H}_{stray\text{-}pinned}$$

The MNP, after bonding into the groove, will be magnetized by the stray fields from both the free and pinned layers. Hence its magnetization can be expressed by:

$$\boldsymbol{M} = \boldsymbol{M}_s \times L\left(\frac{\boldsymbol{m}_0 \mu_0 \boldsymbol{H}_{stray\text{-}film}}{k_B T}\right)$$

where $\boldsymbol{H}_{stray\text{-}film}$ is the stray fields from the free and pinned layers of the magnetic biosensor. Combining the dipole field that generates by the MNP, the effective field on the free layer after the MNP bonding should be written as:

$$\boldsymbol{H}_{eff} = \boldsymbol{H}_{stray\text{-}pinned} + \boldsymbol{H}_{dipole}$$

Therefore, the difference of the effective field on the free layer changes the magnetization configuration of the free layer. By utilizing the strong stray fields from the free and pinned layers to magnetize the MNP, the external applied field is no longer needed in this novel detection scheme.

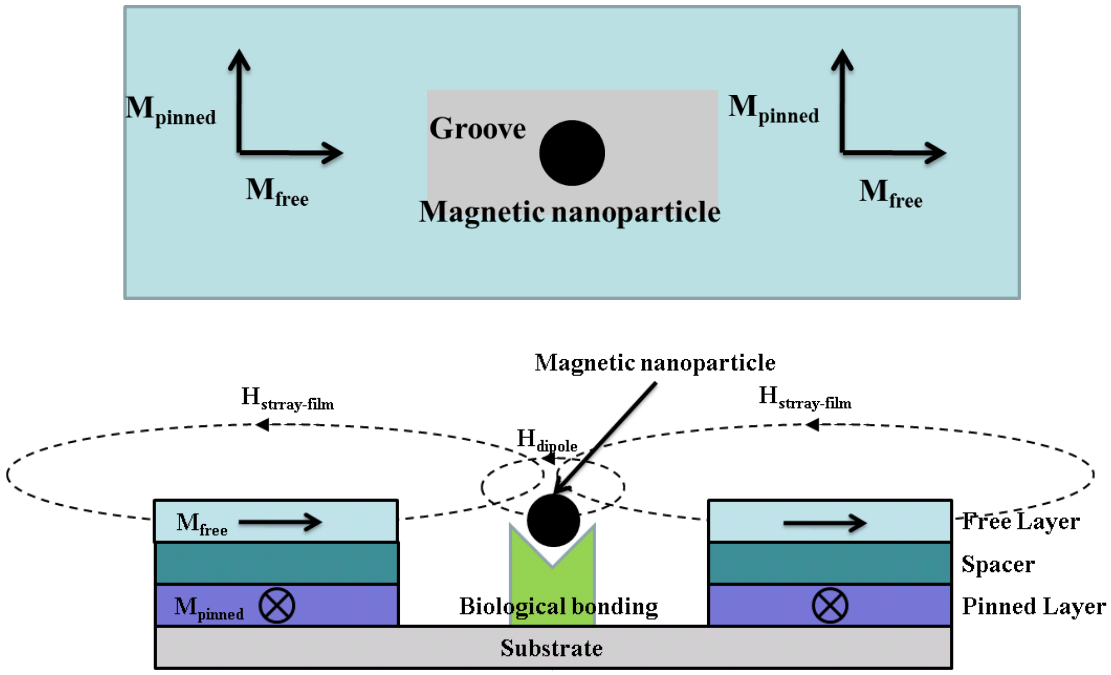

Figure 5.2 External-field-free magnetic biosensing scheme
a) Top view of an external-field-free magnetic biosensing scheme.
b) Cross section view of an external-field-free magnetic biosensing scheme
M_{free} and M_{pinned} are the magnetization of the free and pinned layers of the spin valve structure, respectively. $H_{stray\text{-}film}$ is the stray field from the free and pinned layers. H_{dipole} is the dipole field from the magnetic nanoparticle

5.4 Micromagnetic simulation

Micromagetics typically refer to the interaction of magnetic moments among materials with sub micrometer or nanometer scale. Compared with analytical or other simulation, micromagnetic simulation is often considered to be closer to the "accurate" situation. The basic idea of micromagnetic simulation is to divide the simulation object into many small

cells (typically nanometer size), then study the both individual and collective behavior/interaction of magnetic moment inside the small cells. The simulation is based on the calculation of several competing energies and their interaction, such as dipole energy, Zeeman energy, exchange energy and anisotropy energy. Therefore, the physical parameters which relate to these energy terms, such as magnetization, magnetic anisotropy, shape anisotropy exchange constant and damping coefficient, are critical to simulation results.

In this chapter, a well-established 2-D Micromagnetic simulation software, the object-oriented micromagnetic framework (OOMMF)[110], is employed to simulate the magnetization behavior of the free layer under the stray field from the pinned layer and the dipole field from the MNPs. OOMMF is a free micromagnetic simulation tool developed by Mike Donahue, and Don Porter in Applied and Computational Mathematics Division (ACMD) of National Institute of Standards and Technology (NIST), which is written in C++ with a Tcl/Tk interface.

Micromagnetic simulation in OOMMF employs Landau–Lifshitz–Gilbert equation for the divided small cell of a magnetic material[111]

$$\frac{\boldsymbol{dM}}{\boldsymbol{dt}} = -\gamma \boldsymbol{M} \times \boldsymbol{H}_{eff} - \frac{\gamma \alpha}{\boldsymbol{M}_s} \boldsymbol{M} \times (\boldsymbol{M} \times \boldsymbol{H}_{eff})$$

where $\boldsymbol{M}$ is the magnetization of the magnetic material, $\boldsymbol{H}_{eff}$ is the effective magnetic field, γ is the electron gyromagnetic ratio, α is the damping constant and $\boldsymbol{M}_s$ is the saturation magnetization. The effective field $\boldsymbol{H}_{eff}$ can be calculated as[111]

$$\boldsymbol{H}_{eff} = -\frac{1}{\mu_0 \boldsymbol{M}_s}\frac{\partial E}{\partial \boldsymbol{m}} = \frac{2A}{\mu_0 \boldsymbol{M}_s}\nabla^2 \boldsymbol{m} - \frac{1}{\mu_0 \boldsymbol{M}_s}\frac{\partial E_k}{\partial \boldsymbol{m}} + \boldsymbol{H}_{app} + \boldsymbol{H}_d$$

where μ_0 is the permeability of vacuum, $\boldsymbol{M}_s$ is the saturation magnetization, E is micromagnetic energy density, which usually includes anisotropy energy density E_k, exchange constant A, applied field $\boldsymbol{H}_{app}$, demagnetization $\boldsymbol{H}_d$ energy densities. In OOMMF simulation, all the constants and energy densities are considered to be the same inside the cell. The simulation of the entire object is then based on micromagnetic simulation of individual cells and the interaction of all the cells of the simulated object.

5.4.1 Micromagnetic simulation without magnetic particle

In OOMMF, Micromagnetic Input Format (MIF), which can be edited as a text file, is used as an input to the simulation. It contains all the physical parameters, such as saturation magnetization, exchange constant, uniaxial anisotropy, easy axis of anisotropy direction, demagnetization type, cell shape and size, initial magnetization direction, applied magnetic field, simulation converging criteria and etc.. These parameters are required by mmSolve2D, which is the main solver for the micromagnetic simulation.

Following is an example of MIF file as the input of pinned layer simulation.

MATERIAL PARAMETERS

All units are SI.

Saturation Magnetization of the pinned layer (A/m)

ms:1.5e+6

Exchange constant (J/m)

a:1e-11

Uniaxial anisotropy (J/m^3)

k1:10e3

Anisotropy type, One of <uniaxial|cubic>

anisotropy type:uniaxial

Initial anisotropy

anisotropy init: constant

Directional cosines wrt to coordinate axes.

anisotropy dir1:1 0 0

Demag coefficient, dimensionless

Damp Coef: 0.5

Demag type, One of <ConstMag|3dSlab|2dSlab|3dCharge|FastPipe|None>

demag type:3dslab

Part geometry (m)

part height:0.5e-6

part width:3e-6

part thickness:3e-9

Part shape; in this case, part shape is defined by an external figure file

part shape: Mask 3000_500_BG_100_100_notch.bmp

Cell size (m)

cell size:5e-9

Initial magnetization direction

init mag:uniform 90. 0.

External applied field type and range

Field range specifies how magnetic field is applied to the pinned layer

There are total seven parameters in the range. The first three numbers are the

starting x, y, z fields in Tesla. The next three numbers are the ending x, y, z

fields in Tesla. The last number specifies the steps between starting and ending

fields. If the step is 0, like in this case, the ending magnetic fields are

ignored, which means the only starting fields are applied through the whole

simulation. In this case, a constant 0.5 T magnetic field is applied on –y direction

of the pinned layer, to mimic pinned field.

field type: uniform

field range: 0 -0.5 0 0 -0.5 0 0

Simulation converging criteria

This is the control point of the minimum torque ($|\boldsymbol{m} \times \boldsymbol{h}|$) acting on local

magnetization. Once the minimum torque reaches this point, the simulation

of each field step will be stopped.

default control point spec: -torque 1e-6

This is where the base output filename/format are defined

base output filename: archive\indcfield_3000_500_BG_100_100_notch

magnetization output format: text %.10g

total field output format: text %.10g

Randomizer seed setting. If setting is 1, use seed randomize number generator

randomizer seed:1

In the simulation, both free and pinned layer with a groove structure are divided into small magnetic cells with the same size (5 nm). Each magnetic cell has its own magnetic moment and interacts with all other cells. For free layer, no external magnetic field is applied to it; while for pinned layer, a 0.5 T external magnetic field is set in MIF to mimic the pinning field from antiferromagnetic (AFM) layer.

Typically in MIFG file, the part shape defines the shape of the simulation object, and part geometry defines the dimensions. However, due to the irregular shape of groove structure sensor, the part shape and dimensions of this simulation are defined by external bmp files with different groove sizes. Figure 5.3 shows the definition of the dimensions for the sensor with a groove structure. In the OOMMF simulation, the size of the magnetic biosensor is fixed at 3 μm long (L_s) by 0.5 μm wide (W_s), while the groove dimension (length L_g and width W_g) varies for optimization. Both free and pinned layer share the same part geometry and dimensions.

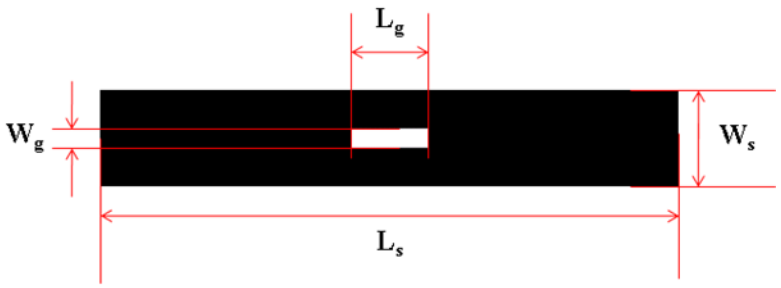

Figure 5.3 Top view of magnetic biosensor with groove structure.
L_s and L_g are the length of the magnetic biosensor and groove, respectively. W_s and W_g are the width of the magnetic biosensor and groove, respectively.

In this simulation, there are two types of simulation result outputs are being used/processed. One is .omf for magnetization vector file. OMF file is in vector field format (OVF), which contains local magnetization vector quantities of each cell. Figure 5.4 shows magnetization vector distribution of pinned layers with different size groove structures (a) 100 nm × 100 nm groove structure; b) 100 nm × 200 nm groove structure; c) 100 nm × 400 nm groove structure; d) 100 nm × 600 nm groove structure)). They are just four examples of various groove structures in this simulation. Around the edge of the groove structures, it looks like the magnetization vectors are aligned with other bulk magnetization vectors. However, if we look into the detail, which is shown in Figure 5.5, the magnetization vectors of individual cell around the groove edge have some deviations from magnetization vectors in bulk structure. This is due to the energy competition

between demagnetization field and the strong pinning field (0.5T) defined in the MIF input files. There is no external applied magnetic field in all the simulation here.

The other output file is .ohf file. OHF contains local magnetic field vectors in spiral positions. Figure 5.6 shows the magnetic field vector distribution on free layer position from pinned layer. Each magnetic field vector is the sum of magnetic stray fields originating from all the magnetizations on pinned layer, as shown in Figure 5.4. It can be noticed that magnetic fields also exist in the groove structure. Therefore, the stray fields from pinned layer need to be considered during the simulation of magnetic fields applied on the magnetic particle. Not only is ohf an output from OOMMF simulation, but also can it be treated as an input to OOMMF simulation. In OOMFF input definition file MIF, the external applied field can be defined from an ohf file, which defines a local magnetic field on each cell. Figure 5.7 demonstrates magnetization vector distribution of free layer with different groove structure sizes. There is no real external magnetic field applied, however, free layer is affected by the stray field from pinned layer. Therefore, magnetic field vectors of pinned layer, as shown in Figure 5.6, are used as the input to simulate the magnetization of free layer. As shown in Figure 5.7, the free layer magnetization vectors tend to align to the long axis of the sensor, which is defined by the competition of the shape anisotropy and the stray field from pinned layer.

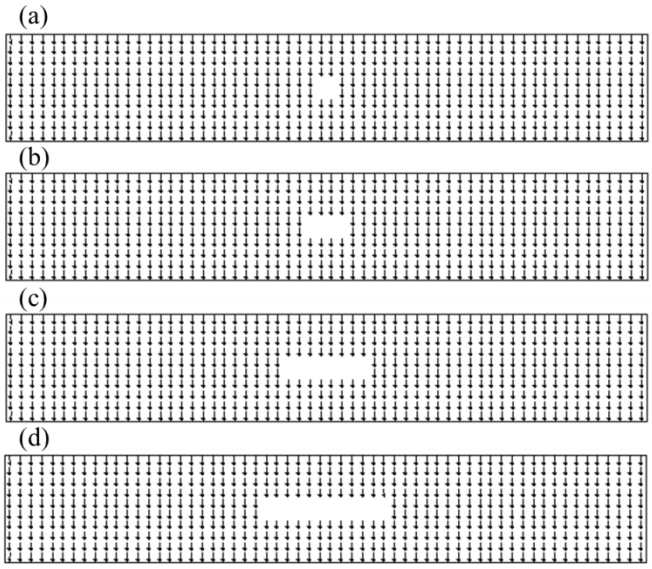

Figure 5.4 Pinned layer magnetization vector distribution with different groove structure sizes.
Arrow subsample: 10; view from +z direction
a) 100 nm × 100 nm groove structure; b) 100 nm × 200 nm groove structure; c) 100 nm × 400 nm groove structure; d) 100 nm × 600 nm groove structure

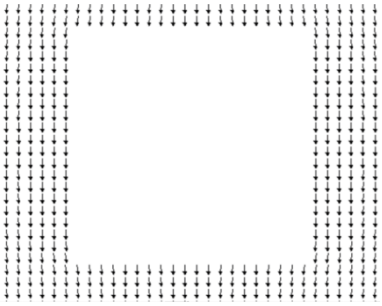

Figure 5.5 Zoom in view of 100 nm × 100 nm groove structure edge of pinned layer magnetization vector distribution
Arrow subsample: 1; view from +z direction

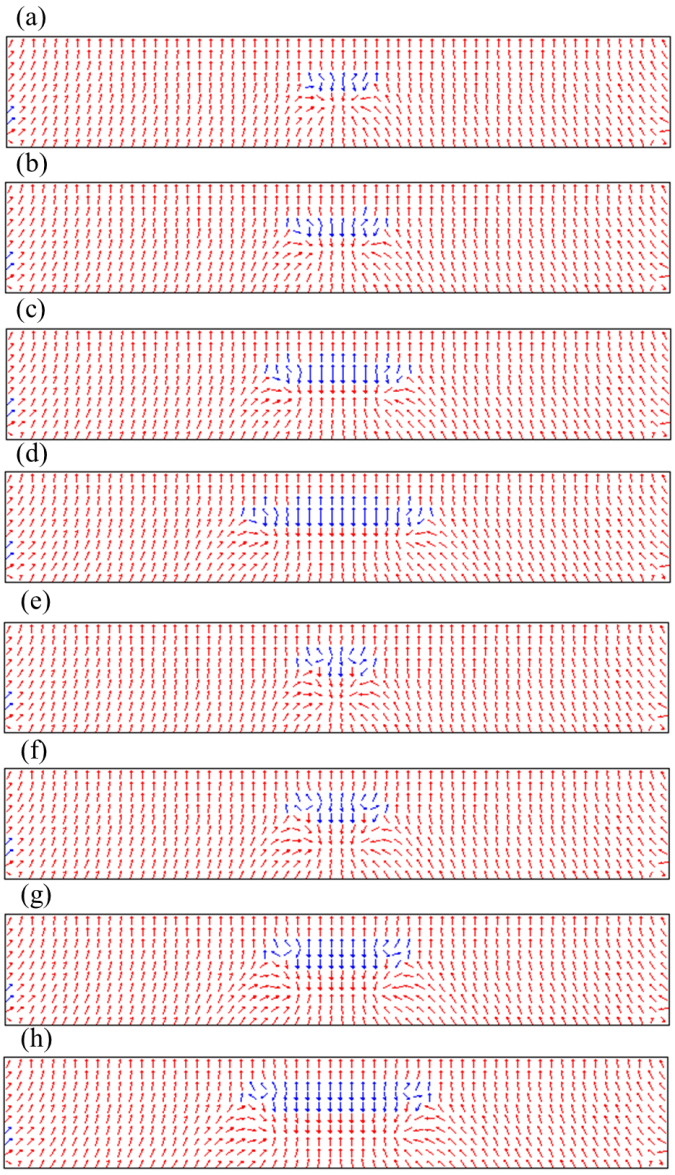

Figure 5.6 Magnetic field vector distribution on free layer from pinned layer with different groove structure sizes
Arrow subsample: 10; Data scale: 0.181 A/m
a) 100 nm × 100 nm groove structure; b) 100 nm × 200 nm groove structure; c) 100 nm × 400 nm groove structure; d) 100 nm × 600 nm groove structure

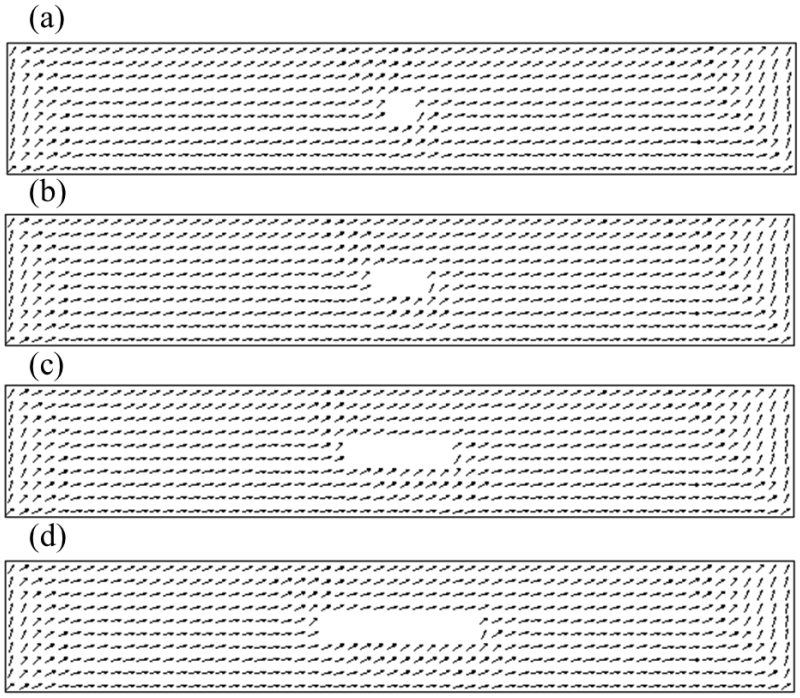

Figure 5.7 Free layer magnetization vector distribution with different groove structure sizes
Arrow subsample: 1; view from +z direction
a) 100 nm × 100 nm groove structure; b) 100 nm × 200 nm groove structure; c) 100 nm × 400 nm groove structure; d) 100 nm × 600 nm groove structure; e) 200 nm × 100 nm groove structure; f) 200 nm × 200 nm groove structure; g) 200 nm × 400 nm groove structure; h) 200 nm × 600 nm groove structure

5.4.2 Micromagnetic simulation with magnetic particle

In general, the detection signal of MNP using groove structure sensor, is computed from the averaged magnetization distribution of free layer with and without the existence of MNP. The detail micromagnetic process is listed in Figure 5.8. The pinned layer magnetization vectors and magnetic field vectors on the free layer are firstly calculated

by OOMMF. While for free layer, before the MNP bonding, the effective field is the sum of the stay fields from all the magnetic cells of the pinned layer. Therefore, the free layer magnetization without MNP can be calculated, using pinned layer magnetic stray field as the external field in OOMMF. With the MNP sitting in the groove, we assume the center of the MNP is the same level with the center of the free layer as shown in Figure 5.2 (b). The MNP is magnetized by the total field from all the magnetic cells of the free and pinned layers. The dipole field from the MNP is discretized and incorporated into the OOMMF input file as well as the stray field from the pinned layer on the free layer. So, with the existence of MNP, the averaged magnetization orientations of the free layer are computed from the magnetization distribution of the magnetic cells by OOMMF.

5.5 Micromagnetic Simulation Results

In this section, a single commercial available iron oxide MNP is simulated to explore the maximum sensitivity of this scheme while the MNP resides at the center of the groove structure. The iron oxide MNP has saturation magnetization value of 480 emu/cm^3 and radius of 8 nm. The signal from the MNP is represented by the change of the magnetoresistive ratio (MR) with and without the presence of the MNP. Figure 5.9 and Figure 5.10 show the MR change due to the MNP for different groove dimensions. In Figure 5.9 and Figure 5.10, the width of the groove is fixed at 100 nm and 200 nm, respectively, while the length of the groove varies from 100 nm to 700 nm. As shown in

Figure 5.9, the signal is at the maximum when the groove length is 100 nm in this simulation. It indicates stronger stray field from both the free and pinned layers acting on the MNP and stronger interaction between MNP dipole field the free layer. The signal then decreases rapidly to the minimum with 200 nm groove length and increases as the length increases, suggesting a complicated interaction among the free/pinned stray fields, MNP dipole field and free layer. Figure 5.10 shows a maximum signal (8.9×10^{-5}) with 100 nm groove length structure in this simulation. The signal then decreases dramatically with 200 nm groove length and increases slowly with a longer groove structure. In comparison, for a sensor with groove length longer than 200 nm, the sensor with 200 nm groove width shows a more stable signal change than 100 nm width case. This is possibly due to the reduced magnetic material left on the magnetic biosensor. Compared with experimental data[112], which shows a noise level around 10^{-5} MR change using a spin valve biosensor, a maximum sensitivity (around 40 dB) of ten nanoparticles detection can be achieved using our detection method.

5.6 Detection of magnetic nanoparticle using external-field free sensor

As proof of concept, a GMR sensor with groove structure of 200 nm × 200 nm was fabricated using electron beam lithography, and based on this sensor, real time detection of 30 μL magnetic nanoparticles (30 nm in diameter) was demonstrated.

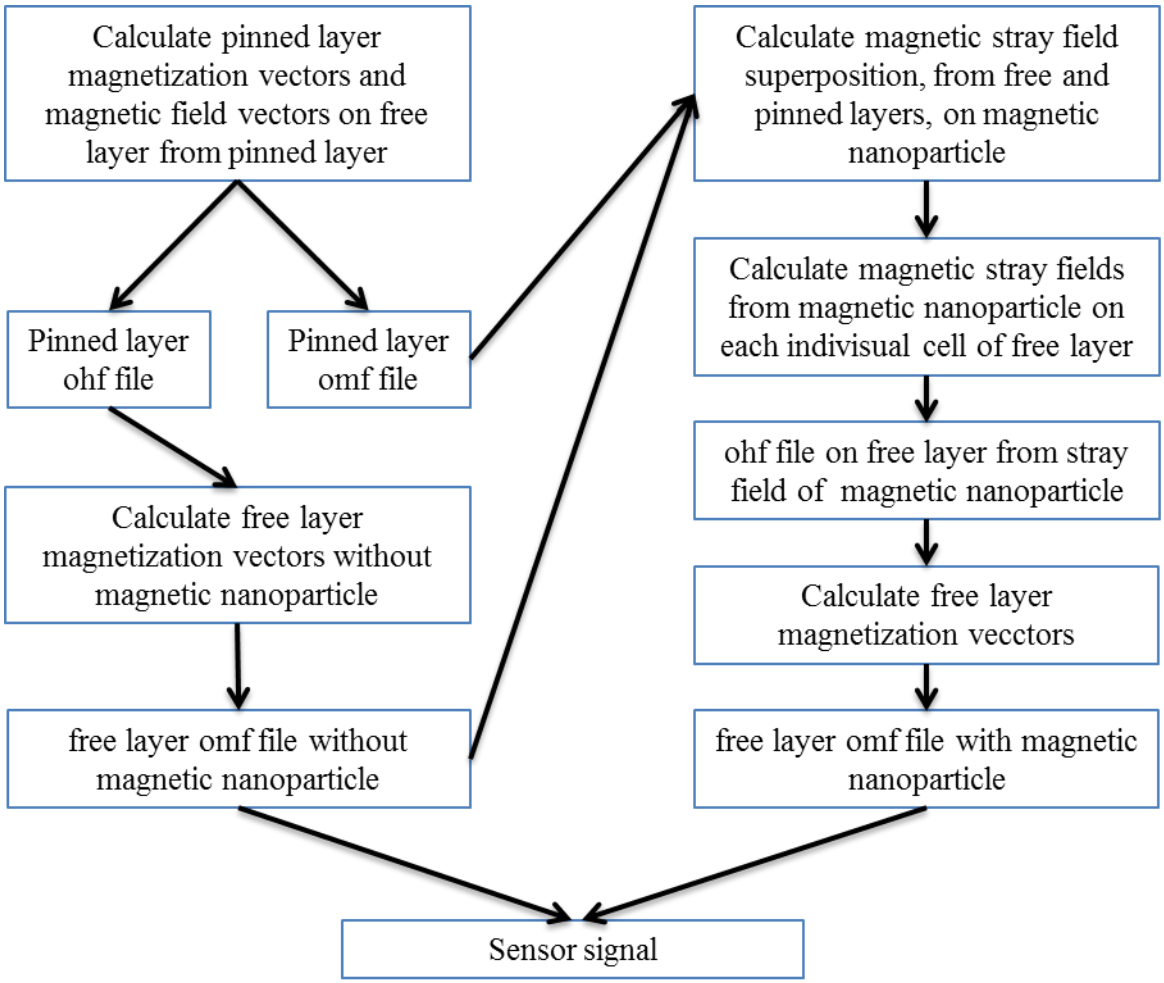

Figure 5.8 Micromagnetic simulation flow of detection signal of magnetic biosensor with groove structure

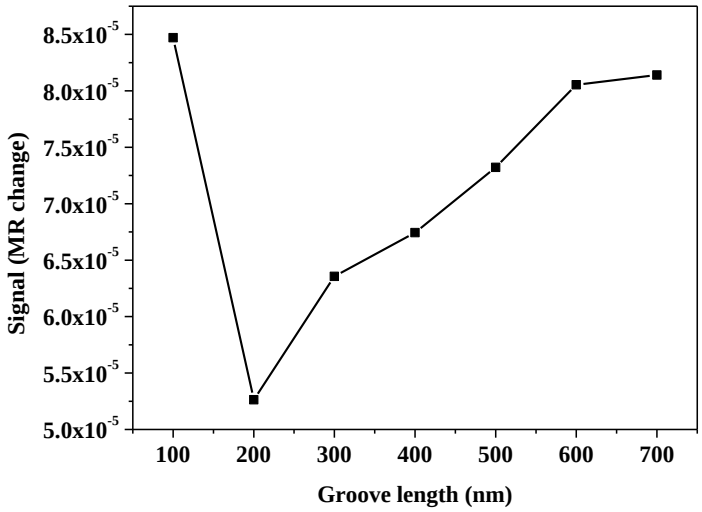

Figure 5.9 The signal from one 8 nm radius iron oxide magnetic nanoparticle, in terms of magnetoresistive ratio (MR) change, of biosensor with 100 nm groove width and different groove length

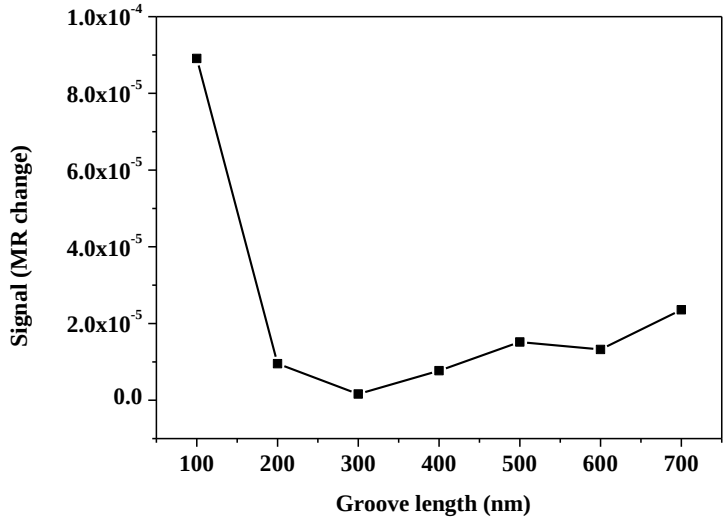

Figure 5.10 The signal from one 8 nm radius iron oxide magnetic nanoparticle, in terms of magnetoresistive ratio (MR) change, of biosensor with 200 nm groove width and different groove length

5.6.1 External-field free sensor fabrication

The fabrication of external-field free sensor is based on the fabrication of stripe sensor, which is described in chapter 4. The extra one step is to put groove structure on the stripe sensor before ion milling, using electron beam lithography due to the sub-micrometer size of groove structure and the width of stripe sensor. In electron beam lithography process, the key is the alignment between the groove structure and the stripe sensor. As proof of concept, a GMR sensor with groove structure of 200 nm × 200 nm was fabricated using electron beam lithography, and based on this sensor, real time detection of 30 μL magnetic nanoparticles (30 nm in diameter) was demonstrated. Figure 5.11 shows the schematic mask drawing of 200 nm × 200 nm groove pattern on top of 500 nm width GMR sensor strip, for electron beam lithography patterning. In order to improve the alignment between the groove structures and GMR stripes, one extra line of groove structures was patterned in the middle of two GMR sensor stripes.

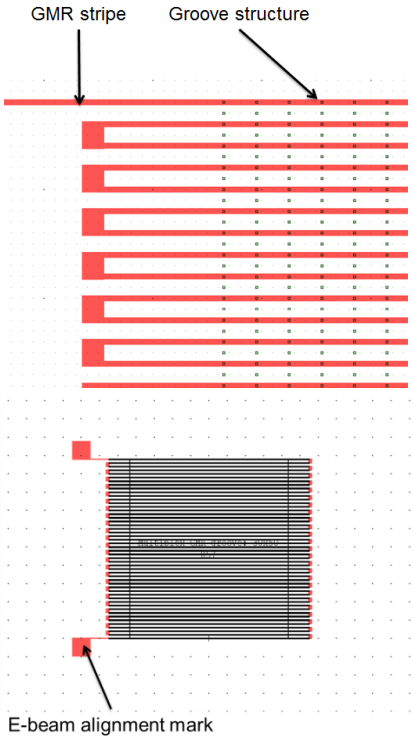

Figure 5.11 Schematic mask drawing of GMR sensor with groove structure for electron beam lithography

The electron beam patterning procedure is listed in the following steps:

1) Pre-bake 250C, 5min
2) Spin coating with PMMA-C9, 3500 rpm, 45sec
3) Softbake 180C, 2min
4) Pattern definition by electron beam lithography
5) Check on the microscope for nanoholes

6) Ionmill etch, etch for stack thickness (10 degree for 3x3mins, 60 degree for 1x3mins, beam current around 84mA)
7) Lift-off the PMMA: NMP 150C, 1hour + ultrasonic (10 mins).

Figure 5.12 is the optical image (100X) of GMR sensor with 200 nm × 200 nm groove structure after electron beam lithography.

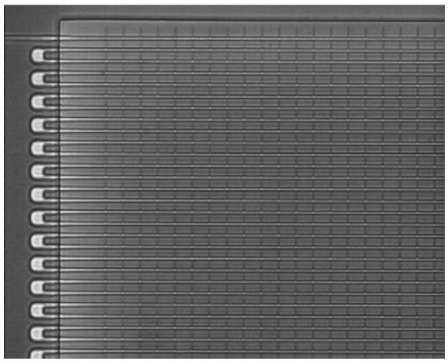

Figure 5.12 optical image (100X) of GMR sensor with 200 nm × 200 nm groove structure

5.6.2 Real time magnetic nanoparticle detection

Magnetic nanoparticles were detected using the GMR sensor with groove structures. Figure 5.13 shows real time detection of 30 μL 30 nm magnetic nanoparticle (1mg/mL), using GMR sensor with 200 nm × 200 nm groove structure. Before adding any DI water and magnetic nanoparticles, a baseline of detection was first established only by applying AC current through GMR sensor. Then 10 μL DI water was added on top of both active

and control sensors, where sensor signal stayed relatively unchanged as expected. The control sensor was covered by a two-component epoxy, to isolate sensor and particles. Finally, 30 μL solution of 30 nm magnetic nanoparticle (1mg/mL) was spotted onto the top of GMR sensor, which generated about 50 μV sensor signal. Since the noise level of the active sensor is around 17 μV, the SNR of the detection is around 9.3 dB.

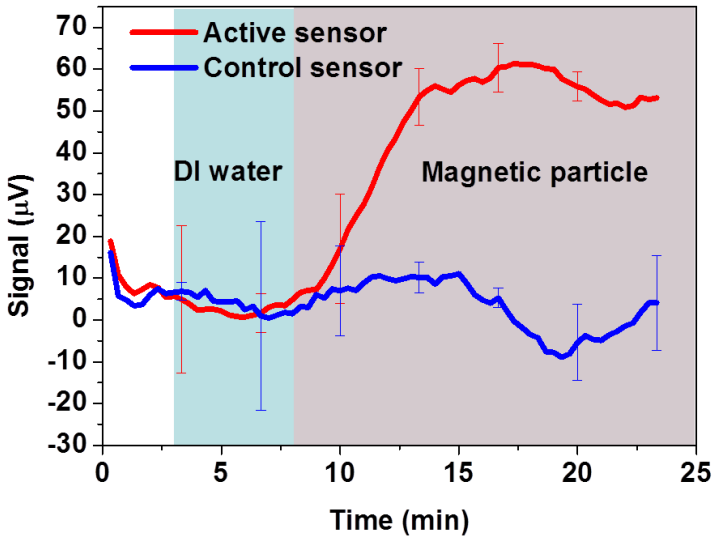

Figure 5.13 Real time detection of 30 μL 30 nm magnetic nanoparticle (1mg/mL), using GMR sensor with 200 nm × 200 nm groove structure

5.7 Conclusion

In summary, an external-field-free magnetic biosensing structure is demonstrated, which is useful for magnetic biosensing system miniaturization (e.g. handheld) and

power consumption control. The structure is based on a unique patterned grooves embedded in the magnetic biosensor and employs the stray fields from the free and pinned layers of the magnetic biosensor for MNP magnetization. Micromagnetic simulations were carried out for a theoretical study of this detection scheme. Signals from different groove structures were calculated. The results showed a maximum SNR of 18.6 dB from one 8 nm radius iron oxide magnetic nanoparticle locating in the center of the groove structure. The signal strength increased with the MNP position near the groove corner. In addition, the dynamic detection range of this detection scheme was explored by simulating the signal from multiple nanoparticles in the groove structure. The simulation showed that uniformly distributed 500 nanoparticles did not saturate the sensor signal and the maximum detection limit of this detection scheme was determined by the physical accommodation of nanoparticles in the groove structure. Finally, the real time detection of magnetic nanoparticles was demonstrated experimentally, by a GMR sensor with 200 nm × 200 nm groove structure. The sensor signal is around 50 μV within 10 minutes for the detection of 30 nm magnetic nanoparticles (1mg/mL), for which the estimated landing number of MNPs is 220/μm [26].

Chapter 6 Summary

In this dissertation, a magnetic biosensing system, based on the combination of GMR magnetic biosensor and high moment magnetic nanoparticle, is proposed, fabricated and demonstrated.

The prototype of GMR biosensing sensor has been designed and fabricated through photolithography technique. Comparing with conventional linear GMR sensor, a hysteresis GMR sensor with zero ground state of magnetization between free and fixed layer, is demonstrated. The new hysteresis GMR sensor shows higher sensitivity under a lower required magnetic applied field.

Together with the high moment FeCo magnetic nanoparticle, the magnetic biosensor has been applied to the detection of various biomolecules/biomarkers. We demonstrated the accurate quantification of human IL-6 by sandwich approach. This magnetic biosensing system is able to quantify as low as 200 molecules of human IL-6,. The low signal level of the control sensors suggests no significant non-specific binding using this sensing scheme. Moreover, a linear trend, between the sensing signal and the number of IL-6 molecules on the sensor surface, which suggests the application of GMR biosensing system for quantifying very small amount of the biomarker in the biological sample. In addition, the difference of IL-6 concentrations in human serum samples is nicely identified by the magnetic biosensing system. The accurate detection of various endoglin

concentrations in human urine samples, match with the grades of patent's prostate cancer, which suggests endoglin, is potentially a good biomarker candidate for prostate cancer.

In the last part of the thesis, an external-field free magnetic biosensing system is demonstrated. The external-field free magnetic biosensor utilizes the magnetic stray field from free and fixed layer of GMR sensor, to magnetize the magnetic labels. Micromagnetic simulation is performed to calculate different sensitivities for various dimensions of sensor design. At last, the real time detection of magnetic nanoparticle based on the external-field free sensor is demonstrated.

.

References

1 Gomez, M. & Silvestri, G. A. Lung Cancer Screening. *The American Journal of the Medical Sciences* **335**, 46-50 10.1097/MAJ.1090b1013e31815d32600, (2008).

2 Schena, M., Shalon, D., Davis, R. W. & Brown, P. O. Quantitative Monitoring of Gene Expression Patterns with a Complementary DNA Microarray. *Science* **270**, 467-470, (1995).

3 Lockhart, D. J. & Winzeler, E. A. Genomics, gene expression and DNA arrays. *Nature* **405**, 827-836, (2000).

4 Brazma, A. *et al.* Minimum information about a microarray experiment (MIAME)[mdash]toward standards for microarray data. *Nat Genet* **29**, 365-371, (2001).

5 Gresham, D., Dunham, M. J. & Botstein, D. Comparing whole genomes using DNA microarrays. *Nat Rev Genet* **9**, 291-302, (2008).

6 Hoheisel, J. D. Microarray technology: beyond transcript profiling and genotype analysis. *Nat Rev Genet* **7**, 200-210, (2006).

7 Sauer, S. *et al.* Miniaturization in functional genomics and proteomics. *Nat Rev Genet* **6**, 465-476, (2005).

8 Kulasingam, V., Pavlou, M. P. & Diamandis, E. P. Integrating high-throughput technologies in the quest for effective biomarkers for ovarian cancer. *Nat Rev Cancer* **10**, 371-378, (2010).

9 Wood, S. L., Knowles, M. A., Thompson, D., Selby, P. J. & Banks, R. E. Proteomic studies of urinary biomarkers for prostate, bladder and kidney cancers. *Nat Rev Urol* **10**, 206-218, (2013).

10 Altelaar, A. F. M., Munoz, J. & Heck, A. J. R. Next-generation proteomics: towards an integrative view of proteome dynamics. *Nat Rev Genet* **14**, 35-48, (2013).

11 Kulasingam, V. & Diamandis, E. P. Strategies for discovering novel cancer biomarkers through utilization of emerging technologies. *Nat Clin Prac Oncol* **5**, 588-599, (2008).

12 Kelloff, G. J. & Sigman, C. C. Cancer biomarkers: selecting the right drug for the right patient. *Nat Rev Drug Discov* **11**, 201-214, (2012).

13 Peták, I., Schwab, R., Őrfi, L., Kopper, L. & Kéri, G. Integrating molecular diagnostics into anticancer drug discovery. *Nat Rev Drug Discov* **9**, 523-535, (2010).

14 Wulfkuhle, J. D., Liotta, L. A. & Petricoin, E. F. Proteomic applications for the early detection of cancer. *Nat Rev Cancer* **3**, 267-275, (2003).

15 Macy, E. M., Hayes, T. E. & Tracy, R. P. Variability in the measurement of C-reactive protein in healthy subjects: implications for reference intervals and epidemiological applications. *Clinical Chemistry* **43**, 52-58, (1997).

16 Dianne, M. F. & Donna Pauler, A. in *Handbook of Statistics in Clinical Oncology, Second Edition* 383-394 (Chapman and Hall/CRC, 2005).

17 Watson, L. *et al.* Urine biomarkers for monitoring juvenile lupus nephritis: a prospective longitudinal study. *Pediatr Nephrol* **29**, 397-405, (2014).

18 Pottgiesser, T. & Schumacher, Y. O. Biomarker monitoring in sports doping control. *Bioanalysis* **4**, 1245-1253, (2012).

19 Ward, T. H. *et al.* Biomarkers of apoptosis. *Br J Cancer* **99**, 841-846, (2008).

20 Westman, K. W. A. *et al.* Clinical evaluation of a capture ELISA for detection of proteinase-3 antineutrophil cytoplasmic antibody. *Kidney Int* **53**, 1230-1236, (1998).

21 Chin, C. D. *et al.* Microfluidics-based diagnostics of infectious diseases in the developing world. *Nat Med* **17**, 1015-1019, (2011).

22 Engvall, E. & Perlmann, P. Enzyme-linked immunosorbent assay (ELISA) quantitative assay of immunoglobulin G. *Immunochemistry* **8**, 871-874, (1971).

23 Osterfeld, S. J. *et al.* Multiplex protein assays based on real-time magnetic nanotag sensing. *Proceedings of the National Academy of Sciences* **105**, 20637-20640, (2008).

24 Gaster, R. S. *et al.* Matrix-insensitive protein assays push the limits of biosensors in medicine. *Nature Medicine* **15**, 1327-1332, (2009).

25 Martins, V. C. *et al.* Challenges and trends in the development of a magnetoresistive biochip portable platform. *Journal of Magnetism and Magnetic Materials* **322**, 1655-1663, (2010).

26 de Boer, B. M., Kahlman, J. A. H. M., Jansen, T. P. G. H., Duric, H. & Veen, J. An integrated and sensitive detection platform for magneto-resistive biosensors. *Biosensors and Bioelectronics* **22**, 2366-2370, (2007).

27 Sandhu, A. Biosensing: New probes offer much faster results. *Nat Nano* **2**, 746-748, (2007).

28 Rife, J. C. *et al.* Design and performance of GMR sensors for the detection of magnetic microbeads in biosensors. *Sensors and Actuators A: Physical* **107**, 209-218, (2003).

29 Justino, C. I. L., Rocha-Santos, T. A. & Duarte, A. C. Review of analytical figures of merit of sensors and biosensors in clinical applications. *TrAC Trends in Analytical Chemistry* **29**, 1172-1183, (2010).

30 Silva, L. I. B., Rocha-Santos, T. A. P. & Duarte, A. C. Development of a fluorosiloxane polymer-coated optical fibre sensor for detection of organic volatile compounds. *Sensors and Actuators B: Chemical* **132**, 280-289, (2008).

31 Cooper, M. A. Optical biosensors in drug discovery. *Nat Rev Drug Discov* **1**, 515-528, (2002).

32 Simonian, A. L., Good, T. A., Wang, S. S. & Wild, J. R. Nanoparticle-based optical biosensors for the direct detection of organophosphate chemical warfare agents and pesticides. *Analytica Chimica Acta* **534**, 69-77, (2005).

33 Jabłoński, A. Efficiency of Anti-Stokes Fluorescence in Dyes. *Nature* **131**, 2, (1993).

34 Pease, A. C. *et al.* Light-generated oligonucleotide arrays for rapid DNA sequence analysis. *Proceedings of the National Academy of Sciences* **91**, 5022-5026, (1994).

35 Lockhart, D. J. *et al.* Expression monitoring by hybridization to high-density oligonucleotide arrays. *Nat Biotech* **14**, 1675-1680, (1996).

36 DeRisi, J. L., Iyer, V. R. & Brown, P. O. Exploring the Metabolic and Genetic Control of Gene Expression on a Genomic Scale. *Science* **278**, 680-686, (1997).

37 Wodicka, L., Dong, H., Mittmann, M., Ho, M.-H. & Lockhart, D. J. Genome-wide expression monitoring in Saccharomyces cerevisiae. *Nat Biotech* **15**, 1359-1367, (1997).

38 Brown, P. O. & Botstein, D. Exploring the new world of the genome with DNA microarrays. *Nat Genet*.

39 Duggan, D. J., Bittner, M., Chen, Y., Meltzer, P. & Trent, J. M. Expression profiling using cDNA microarrays. *Nat Genet*.

40 Lipshutz, R. J., Fodor, S. P. A., Gingeras, T. R. & Lockhart, D. J. High density synthetic oligonucleotide arrays. *Nat Genet*.

41 Talhavini, M. & Atvars, T. D. Z. Photostability of xanthene molecules trapped in poly(vinyl alcohol) (PVA) matrices. *Journal of Photochemistry and Photobiology A: Chemistry* **120**, 141-149, (1999).

42 Wood, R. W. XLII. On a remarkable case of uneven distribution of light in a diffraction grating spectrum. *Philosophical Magazine Series 6* **4**, 396-402, (1902).

43 Kneipp, K. *et al.* Single Molecule Detection Using Surface-Enhanced Raman Scattering (SERS). *Physical Review Letters* **78**, 1667-1670, (1997).

44 Rothenhausler, B. & Knoll, W. Surface–plasmon microscopy. *Nature* **332**, 615-617, (1988).

45 Ozbay, E. Plasmonics: Merging Photonics and Electronics at Nanoscale Dimensions. *Science* **311**, 189-193, (2006).

46 Maier, S. A. & Atwater, H. A. Plasmonics: Localization and guiding of electromagnetic energy in metal/dielectric structures. *Journal of Applied Physics* **98**, 011101, (2005).

47 Barnes, W. L., Dereux, A. & Ebbesen, T. W. Surface plasmon subwavelength optics. *Nature* **424**, 824-830, (2003).

48 Homola, J., Yee, S. S. & Gauglitz, G. Surface plasmon resonance sensors: review. *Sensors and Actuators B: Chemical* **54**, 3-15, (1999).

49 Hoa, X. D., Kirk, A. G. & Tabrizian, M. Towards integrated and sensitive surface plasmon resonance biosensors: A review of recent progress. *Biosensors and Bioelectronics* **23**, 151-160, (2007).

50 Shankaran, D. R., Gobi, K. V. & Miura, N. Recent advancements in surface plasmon resonance immunosensors for detection of small molecules of biomedical, food and environmental interest. *Sensors and Actuators B: Chemical* **121**, 158-177, (2007).

51 Otto, A. Excitation of nonradiative surface plasma waves in silver by the method of frustrated total reflection. *Z. Physik* **216**, 398-410, (1968).

52 Kretschmann, E. & Raether, H. Radiative decay of nonradiative surface plasmons excited by light. *Z. Naturforsch. A* **23**, 2135, (1968).

53 Jorgenson, R. C. & Yee, S. S. A fiber-optic chemical sensor based on surface plasmon resonance. *Sensors and Actuators B: Chemical* **12**, 213-220, (1993).

54 Slavík, R., Homola, J., Čtyroký, J. & Brynda, E. Novel spectral fiber optic sensor based on surface plasmon resonance. *Sensors and Actuators B: Chemical* **74**, 106-111, (2001).

55 Monzón-Hernández, D., Villatoro, J., Talavera, D. & Luna-Moreno, D. Optical-fiber surface-plasmon resonance sensor with multiple resonance peaks. *Appl. Opt.* **43**, 1216-1220, (2004).

56 Baibich, M. N. *et al.* Giant Magnetoresistance of (001)Fe/(001)Cr Magnetic Superlattices. *Physical Review Letters* **61**, 2472-2475, (1988).

57 Binasch, G., Grünberg, P., Saurenbach, F. & Zinn, W. Enhanced magnetoresistance in layered magnetic structures with antiferromagnetic interlayer exchange. *Physical Review B* **39**, 4828-4830, (1989).

58 Mott, N. F. The Electrical Conductivity of Transition Metals. *Proceedings of the Royal Society of London A: Mathematical, Physical and Engineering Sciences* **153**, 699-717, (1936).

59 Tsymbal, E. Y. & Pettifor, D. G. in *Solid State Physics* Vol. Volume 56 (eds Ehrenreich Henry & Spaepen Frans) 113-237 (Academic Press, 2001).

60 Dieny, B. *et al.* Magnetotransport properties of magnetically soft spin‐valve structures (invited). *Journal of Applied Physics* **69**, 4774-4779, (1991).

61 Ching, T. *et al.* Design, fabrication and testing of spin-valve read heads for high density recording. *Magnetics, IEEE Transactions on* **30**, 3801-3806, (1994).

62 Heim, D. E. *et al.* Design and operation of spin valve sensors. *Magnetics, IEEE Transactions on* **30**, 316-321, (1994).

63 Baselt, D. R. *et al.* A biosensor based on magnetoresistance technology. *Biosensors and Bioelectronics* **13**, 731-739, (1998).

64 Schotter, J. *et al.* Comparison of a prototype magnetoresistive biosensor to standard fluorescent DNA detection. *Biosensors and Bioelectronics* **19**, 1149-1156, (2004).

65 Tondra, M., Porter, M. & Lipert, R. J. Model for detection of immobilized superparamagnetic nanosphere assay labels using giant magnetoresistive sensors. *J. Vac. Sci. Technol. A-Vac. Surf. Films* **18**, 1125-1129, (2000).

66 Martins, V. C. *et al.* Challenges and trends in the development of a magnetoresistive biochip portable platform. *J Magn Magn Mater* **322**, 1655-1663, (2009).

67 Janssen, X. J. A., van Ijzendoorn, L. J. & Prins, M. W. J. On-chip manipulation and detection of magnetic particles for functional biosensors. *Biosensors and Bioelectronics* **23**, 833-838, (2008).

68 Wirix-Speetjens, R., Fyen, W., De Boeck, J. & Borghs, G. Single magnetic particle detection: Experimental verification of simulated behavior. *Journal of Applied Physics* **99**, 103903-103904, (2006).

69 Shen, W. *et al.* Detection of DNA labeled with magnetic nanoparticles using MgO-based magnetic tunnel junction sensors. *Journal of Applied Physics* **103**, -, (2008).

70 Li, Y. *et al.* in *Engineering in Medicine and Biology Society, 2009. EMBC 2009. Annual International Conference of the IEEE.* 5432-5435.

71 Bai, J. & Wang, J.-P. High-magnetic-moment core-shell-type FeCo–Au/Ag nanoparticles. *Appl. Phys. Lett.* **87**, 152502, (2005).

72 Srinivasan, B. *et al.* A Detection System Based on Giant Magnetoresistive Sensors and High-Moment Magnetic Nanoparticles Demonstrates Zeptomole Sensitivity: Potential for Personalized Medicine13. *Angewandte Chemie International Edition* **48**, 2764-2767, (2009).

73 Néel, L. Sur un probleme de magnetostatique relatif a des couches minces ferromagnetiques. *C. R. Hebd. Seances. Acad. Sci.* **A 255**, 1545, (1962).

74 Anderson, N. L. & Anderson, N. G. The human plasma proteome - History, character, and diagnostic prospects. *Mol. Cell. Proteomics* **1**, 845-867, (2002).

75 Prinz, G. A. Device physics - Magnetoelectronics. *Science* **282**, 1660-1663, (1998).

76 Fullerton, E. E. & Schuller, I. K. The 2007 Nobel Prize in Physics: Magnetism and transport at the nanoscale. *ACS Nano* **1**, 384-389, (2007).

77 Fert, A. Ursprung, Entwicklung und Zukunft der Spintronik (Nobel-Vortrag). *Angewandte Chemie* **120**, 6042-6054, (2008).

78 Graham, D. L., Ferreira, H. A. & Freitas, P. P. Magnetoresistive-based biosensors and biochips. *Trends Biotechnol.* **22**, 455-462, (2004).

79 Tamanaha, C. R., Mulvaney, S. P., Rife, J. C. & Whitman, L. J. Magnetic labeling, detection, and system integration. *Biosens. Bioelectron.* **24**, 1-13, (2008).

80 Lagae, L. *et al.* On-chip manipulation and magnetization assessment of magnetic bead ensembles by integrated spin-valve sensors. *Journal of Applied Physics* **91**, 7445-7447, (2002).

81 Miller, M. M. *et al.* A DNA array sensor utilizing magnetic microbeads and magnetoelectronic detection. *Journal of Magnetism and Magnetic Materials* **225**, 138-144, (2001).

82 De Palma, R. *et al.* Magnetic Bead Sensing Platform for the Detection of Proteins. *Analytical Chemistry* **79**, 8669-8677, (2007).

83 Li, G. X. *et al.* Spin valve sensors for ultrasensitive detection of superparamagnetic nanoparticles for biological applications. *Sens. Actuator A-Phys.* **126**, 98-106, (2006).

84 Mitchell, P. A perspective on protein microarrays. *Nat Biotech* **20**, 225-229, (2002).

85 Chan, S. M., Ermann, J., Su, L., Fathman, C. G. & Utz, P. J. Protein microarrays for multiplex analysis of signal transduction pathways. *Nat Med* **10**, 1390-1396, (2004).

86 Diamandis, E. P. Mass Spectrometry as a Diagnostic and a Cancer Biomarker Discovery Tool: Opportunities and Potential Limitations. *Mol. Cell. Proteomics* **3**, 367-378, (2004).

87 Tamanaha, C. R., Mulvaney, S. P., Rife, J. C. & Whitman, L. J. Magnetic labeling, detection, and system integration. *Biosensors and Bioelectronics* **24**, 1-13, (2008).

88 Graham, D. L., Ferreira, H., Bernardo, J., Freitas, P. P. & Cabral, J. M. S. Single magnetic microsphere placement and detection on-chip using current line designs with integrated spin valve sensors: Biotechnological applications. *Journal of Applied Physics* **91**, 7786-7788, (2002).

89 Li, G. & Wang, S. X. Analytical and micromagnetic modeling for detection of a single magnetic microbead or nanobead by spin valve sensors. *Magnetics, IEEE Transactions on* **39**, 3313-3315, (2003).

90 Nordling, J. *et al.* Giant Magnetoresistance Sensors. 1. Internally Calibrated Readout of Scanned Magnetic Arrays. *Analytical Chemistry* **80**, 7930-7939, (2008).

91 Mulvaney, S. P., Myers, K. M., Sheehan, P. E. & Whitman, L. J. Attomolar protein detection in complex sample matrices with semi-homogeneous fluidic force discrimination assays. *Biosensors and Bioelectronics* **24**, 1109-1115, (2009).

92 Anderson, N. L. & Anderson, N. G. The Human Plasma Proteome: History, Character, and Diagnostic Prospects. *Mol. Cell. Proteomics* **1**, 845-867, (2002).

93 Li, L., Chen, S., Oh, S. & Jiang, S. In Situ Single-Molecule Detection of Antibody−Antigen Binding by Tapping-Mode Atomic Force Microscopy. *Analytical Chemistry* **74**, 6017-6022, (2002).

94 Gonzalez, J., Laudano, M., McCann, T., McKiernan, J. & Benson, M. A review of high-risk prostate cancer and the role of neo-adjuvant and adjuvant therapies. *World Journal of Urology* **26**, 475-480, (2008).

95 Vickers, A. J. *et al.* Impact of recent screening on predicting the outcome of prostate cancer biopsy in men with elevated prostate-specific antigen. *Cancer* **116**, 2612-2620, (2010).

96 Fall, K. *et al.* Prostate-Specific Antigen Levels as a Predictor of Lethal Prostate Cancer. *Journal of the National Cancer Institute* **99**, 526-532, (2007).

97 Schmidt, C. Urine Biomarkers May Someday Detect Even Distant Tumors. *Journal of the National Cancer Institute* **101**, 8-10, (2009).

98 Konety, B. R. Panning for Prostate Gold: Urine Based Markers for Prostate Cancer. *The Journal of Urology* **181**, 9-10, (2009).

99 Downes, M. R. *et al.* Urinary markers for prostate cancer. *BJU International* **99**, 263-268, (2007).

100 Fujita, K. *et al.* Endoglin (CD105) as a urinary and serum marker of prostate cancer. *International Journal of Cancer* **124**, 664-669, (2009).

101 Baibich, M. N. *et al.* Giant Magnetoresistance of (001)Fe/(001)Cr Magnetic Superlattices. *Physical Review Letters* **61**, 2472, (1988).

102 Binasch, G., Grünberg, P., Saurenbach, F. & Zinn, W. Enhanced magnetoresistance in layered magnetic structures with antiferromagnetic interlayer exchange. *Physical Review B* **39**, 4828, (1989).

103 Millen, R. L. *et al.* Giant Magenetoresistive Sensors. 2. Detection of Biorecognition Events at Self-Referencing and Magnetically Tagged Arrays. *Analytical Chemistry* **80**, 7940-7946, (2008).

104 Li, Y. *et al.* Nanomagnetic Competition Assay for Low-Abundance Protein Biomarker Quantification in Unprocessed Human Sera. *Journal of the American Chemical Society* **132**, 4388-4392, (2010).

105 Li, Y. *et al.* in *Engineering in Medicine and Biology Society, 2009. Annual International Conference of the IEEE.* 5432-5435.

106 Sandhu, A. *et al.* High efficiency Hall effect micro-biosensor platform for detection of magnetically labeled biomolecules. *Biosensors and Bioelectronics* **22**, 2115-2120, (2007).

107 Thanh, N. T., Kim, K. W., Kim, C. O., Shin, K. H. & Kim, C. G. Microbeads detection using Planar Hall effect in spin-valve structure. *Journal of Magnetism and Magnetic Materials* **316**, e238-e241, (2007).

108 Kurlyandskaya, G. V. *et al.* Giant-magnetoimpedance-based sensitive element as a model for biosensors. *Appl. Phys. Lett.* **82**, 3053-3055, (2003).

109 Troels Borum Grave, H., Christian Danvad, D., Bjarke Thomas, D. & Mikkel Fougt, H. Theoretical study of in-plane response of magnetic field sensor to magnetic beads magnetized by the sensor self-field. *Journal of Applied Physics* **107**, 124511, (2010).

110 Donahue, M. J. & Porter, D. G. OOMMF User's Guide, Version 1.0. *OOMMF User's Guide, Version 1.0, Interagency Report NISTIR 6376*, (1999).

111 Miltat, J. E. & Donahue, M. J. in *Handbook of Magnetism and Advanced Magnetic Materials* (John Wiley & Sons, Ltd, 2007).

112 Gaster, R. S., Hall, D. A. & Wang, S. X. Autoassembly Protein Arrays for Analyzing Antibody Cross-Reactivity. *Nano Letters*, (2010).